2D Phase Formation and Transitions at Electrified Liquid/Solid Interfaces: in-situ STM and Monte Carlo Investigations

Zur Erlangung des akademischen Grades eines

DOKTORS DER NATURWISSENSCHAFTEN

(Dr. rer. nat)

der Fakultät für Chemie und Biowissenschaften der
Universität Karlsruhe (TH)
angenommene

DISSERTATION
von

M. Sc. Dimitar Iliev Borissov

aus Sofia, Bulgarien

Dekan: Prof. Dr. H. Puchta
Referent: Prof. Dr. W. Freyland
Korreferent: Prof. Dr. M. Olzmann
Tag der mündlichen Prufüng: 14.12.2005

to my family and Anna

Contents

Zusammenfassung

Der Schwerpunkt dieser Arbeit richtet sich auf Untersuchungen der zwei dimensionalen(2D) Phasenbildung und Phasenübergänge an unterschiedlichen Grenzflächen, insbesondere den elektrochemischen fest-flüssig Grenzflächen. Die Selbstorganisation unterschiedlicher makrozyklischer Moleküle wurde auf verschiedenen Substrate wie Graphit und Au(111) mittels in-situ Rastertunnelmikroskopie(STM) und Photoelektronenspektroskopie(XPS) unter Ultra-Hoch-Vakuum(UHV) Bedingungen untersucht. STM und konventionelle elektrochemische Methoden wurden eingesetzt, um die Abscheidung von Ag auf Au(111) im Unterpotentialbereich(UPD) aufzuklären. Von besonderem Interesse ist der Vergleich des Elektrokristallizationsmechanismus in unterschiedlichen Elektrolyten, wässrige Elektrolyte im Vergleich zur Ionen Flüssigkeit(IL). Die Gleichgewichts Monte Carlo(MC) Methode wurde verwendet, um die UPD Prozesse zu simulieren und die zugehörigen Adsorptionsisothermen zu bestimmen. Schliesslich wurden Versuche der 2D-Abscheidung von Ag auf Au(111) mittels Potential gepulsten Messungen im UPD Bereich durchgeführt. Diese Experimente ermöglichen einen neuen Einblick in die Abscheidungskinetik und Stabilität von 2D-Clusters. Die wichtigsten Ergebnisse dieser Arbeit können wie folgt zusammengefaßt werden:

Auf Graphite wurden wohlgeordnete 2D Strukturen(SAMs) einer makrozyklischen Verbindung mit Hilfe von STM Messungen gefunden. Die zugehörige Elementarzelle wird bestimmt zu A = 3.8 ± 0.32 nm, B = 6.1 ± 0.45 nm.

Im UPD Bereich von Ag auf Au(111) im wässrigen Elektrolyt findet bei der Reduzierung des angelegten Potentials auf 20 mV ein Phasenübergang von der offenen (3 x 3)-Struktur zur dicht gepackten (1 x 1) Monolage(ML) von Ag auf Au(111) statt. Im Gegensatz zu der UPD-Abscheidung im wässrigen Eletrolyt zeigt der erste Prozess in der Ionen-Flüsigkeit zwei Zyklovoltammogram(CV) Peaks bei 410 mV und 230 mV. Atomar aufgelöste STM-Bilder bei 300 mV zeigen zum ersten Mal einen Phasenübergang (ungeordnet/geordnet, $\sqrt{3}$ x $\sqrt{3}$)R30° Struktur). Es wurden adsorbierte $AlCl_4^-$ Anionen beobachtet, die mit dem ersten UPD Prozess überlappen. Bei beiden Elektrolyten wurde die Bildung einer Ag-Monolage im UPD-Bereich fest-

gestellt. Die elektrochemische Auflösung der Ag-ML führt zu monoatomar tiefen Löchern auf dem Au-Substrat, was auf Oberflächenlegierung hinweist. Die Gleichgewichts MC Simulation von Ag auf Au(111)in wässrigen Lösungen zeigt, dass die effektive Wechselwirkungsenergie zwischen den nächsten Ag-Nachbarn, J1, nach Anpassung der experimentellen Daten für den ersten und den zweiten UPD-Prozess bei T=293°C gleich J1=24 ± 1 meV bzw. J1=40 ± 2 meV ist. Die so bestimmten J1 weisen auf eine effektive Anziehung hin. In der Ionen-Flüsigkeit wurden J1-Werte für den ersten UPD Prozess (bei 410 mV) als leicht abstossend (J1= -10 ± 2 meV) bestimmt. Die Schnappschüsse der MC - Simulationen zeigen, dass die geordnete Ag-Phase bei 200 mV überwiegt, während die ungeordente Phase verschwindet. Dieser Übergang stimmt mit den in-situ STM Ergebnissen überein.

Einstufige gepulste Elektrodeposition von Ag auf Au(111) im UPD - Bereich wurde mittles in-situ STM untersucht. Der Effekt der Pulsdauer (0.2 ms bis 500 ms) auf die Stabilität der 2D-Nanocluster wurde zum ersten Mal erforscht. Für die Interpretation der Kinetik wurde ein gekoppeltes Diffusions-Adsorptions Modell entwickelt.

Abstract

Investigations of this thesis focus on two-dimensional(2D) phase formation and phase transitions at various interfaces, in particular, electrified liquid-solid interfaces. Self-assembly of different macrocyclic molecules has been studied on different substrates such as graphite and Au(111) by in-situ scanning tunneling microscopy(STM) and X-ray photoelectron spectroscopy(XPS) methods under ultra-high vacuum(UHV) conditions. Electrochemical STM and conventional electrochemical methods have been employed to elucidate the underpotential deposition(UPD) of 2D phase formation of Ag on Au(111). Of particular interest is the comparison of the electrocrystallization mechanism in different electrolytes, aqueous vs. ionic liquid(IL). Equilibrium Monte Carlo(MC) method was employed to simulate the UPD of this particular system and to obtain the respective adsorption isotherms. Finally, the experiments on 2D deposition of Ag on Au(111) were completed by pulse potential measurements in the UPD range which give a new insight into the deposition kinetics and stability of 2D clusters. Some of the main results of this thesis are summarized as follows:

Ordered 2D arrays of macrocyclic compounds were characterized by STM on graphite with a unit cell of A = 3.8 $\pm$ 0.32 nm, B = 6.1 $\pm$ 0.45 nm and Γ= 75 $\pm$ 2°. In the UPD of Ag on Au(111) in the aqueous electrolyte, atomically resolved in-situ STM images at 500 mV show a (3 x 3) adlayer of Ag, whereas sweeping the potential to 20 mV, a phase transition from the more open (3 x 3) structure to a dense packed (1 x 1) monolayer(ML) of Ag on Au(111) occurs. In contrast, in the IL, the first UPD process of Ag exhibits two CV peaks at 410 mV and 230 mV. High resolution STM images at 300 mV show for the first time a phase transition (disorder/order) from an inhomogeneous to an ordered phase with a ($\sqrt{3}$ x $\sqrt{3}$)R30° structure. Also, for the first time adsorbed $AlCl_4{}^-$ anions with a superlattice of (1.63 x $\sqrt{3}$)R30° overlapping with the first UPD of Ag were observed. In both electrolytes, formation of one ML of Ag was found in the UPD range. The dissolution of the ML leads to monoatomically deep characteristic pits in the gold substrate which is a signature of surface alloying.

Equilibrium MC simulations of UPD of Ag on Au(111) show that in aqueous solutions, the effective energy of interaction between the 1st nearest neighbor(NN) Ag adatoms, J1, obtained from fits of the experimental data for the first (at 520 mV) and the second (at 25 mV) UPD processes at T=293°C is J1=24 $\pm$ 1 meV and J1=40 $\pm$ 2 meV, respectively. This indicates an effective attraction. In the IL, J1, for the first UPD (at 410 mV) was found to be moderately repulsive, J1= -10 meV. Snapshots of MC simulations for different electrode potentials show that the ordered phase of Ag becomes predominant at 200 mV and the disordered phase disappears, in good agreement with the in-situ STM results.

One step pulsed potential electrodeposition in the UPD region of Ag on Au(111) was studied by in-situ STM. The effect of pulse duration (0.2 ms to 500 ms) on the stability of 2D nanocluster was investigated for the first time. In order to get insight into the kinetics of this process, a coupled diffusion-adsorption model was developed.

Chapter 1

Introduction

Interfaces play an important role in various areas of physics and chemistry, both in fundamental research and technology. A few prominent examples may illustrate this: metal-semicoductor or Schottky contacts which are the basis of semiconductor devices and circuits, interfacial phase transitions or more generally, interfacial thermodynamics and electrochemistry including fundamental problems in phase formation and growth, but also different phenomena in catalysis, colloid chemistry and tribology [1, 2, 3]. Since the invention of Scanning Tunneling Microscope(STM), new insight into interfacial phenomena became possible and novel topics came into focus [4]. Among them is nanoscience and nanothechnology. Phenomena on the nano-meter scale of matter have attracted interest in different disciplines in physics, chemistry and biosciences [5].

Atomistic aspects of phase transitions in two dimentional(2D) adsorbed layers on surfaces studied by STM have attracted a lot of attention as a powerful tool for nano structuring. For instance, spontanious formation of ordered self-assembled monolayers(SAMs) of molecules on surfaces can be considered as a phase transition at the interface. In interfacial electrochemistry with development of the in-situ electrochemical STM technique one can perform structural analysis of ordered(disrodered) adsorbed metal phases and study their properties as a function of time as well as of the applied electrode potential. Also, sudden deposition of monolayers on electrode surfaces at potential

positive with respect to the Nernst potential can be considered as a phase transition on the electrode surface.

The present work deals with the investigation of 2D surface structures and phase transitions at the nano-meter scale. It is divided into three main topics. The first, includes an investigation of SAMs of macrocycles adsorbed on graphite and Au(111) surfaces. The second, 2D phase formation of silver on Au(111) in aqueous and in ionic electrolytes is studied by in situ STM and electrochemical methods as well as by Monte Carlo simulations. The third topic deals with an investigation of 2D silver nano islands formation by applying a fast electrochemical potential pulse in the underpotential deposition region on Au(111).

The outline of the thesis is as follows: After the introduction, in Chapter 2 the basic aspects of the methods used in this study are given. Chapter 3 focuses on the experimental setup, sample preparation and etc. In Chapter 4 are discussed the experimental results concerning 2D self-assembly of macromolecules on graphite and Au(111). Chapter 5 presents 2D phase transitions of under potentially deposited Ag on Au(111) in aqueous and ionic electrolytes. Emphasis is given to similarities and distinction of both electrolytes on the 2D electrocrystallization. The last Chapter 6 includes a study of potential pulsed nanostructuring of Ag on Au(111) in the UPD region.

Chapter 2

Theoretical background

This chapter introduces the methods and required theoretical background which will be useful to know about while reading this thesis.

2.1 Scanning tunneling microscopy (STM)

Scanning tunneling microscopy (STM) is a powerful tool which can be used to directly image electron density of surfaces of conducting samples with atomic resolution and to follow the dynamics of surface processes in real time (*in-situ* STM). The method has revolutionized the advances in surface science over the last 20 years. STM was invented by Binning and Rohrer in 1982 [4, 6, 7] for which they got Nobel Prize in 1986.
The next section deals with the general physics involved in STM which is needed to understand the phenomenon of tunneling process. A more detailed treatment of that topic can be found in the literature [8].

2.1.1 The tunnel effect

To understand how STM works and what principles it is based on, first we develop the concept of the tunnel effect. The tunnel effect originates from the wavelike properties of particles and it is often said to be as old as quantum mechanics. Let us consider a case of an electron which is an incident upon a barrier with a potential energy larger than its kinetic energy,

for example, between two,parallel, plane, metal electrodes of large crossection in comparison to their separation. According to classical mechanics a particle with an energy, E, can overcome a potential barrier of V_0 only if $E > V_0$, otherwise it is reflected as illustrated in Figure 2.1A. STM is a real example which shows that classical physics fails on the atomic level. In quantum mechanical approach, all properties of a system are expressed in terms of a wave function which is obtained by solving the Schrödinger equation. In quantum mechanics the probability of the electron to traverse through the barrier is non-zero even if $E < V_0$. This is sketched in Figure 2.1B for an electron of energy, E, and mass m, and a potential barrier of height V_0 and width d. The axis perpendicular to the plane parallel electrodes is the z-axis, with its zero on the left side of the tunnel gap.
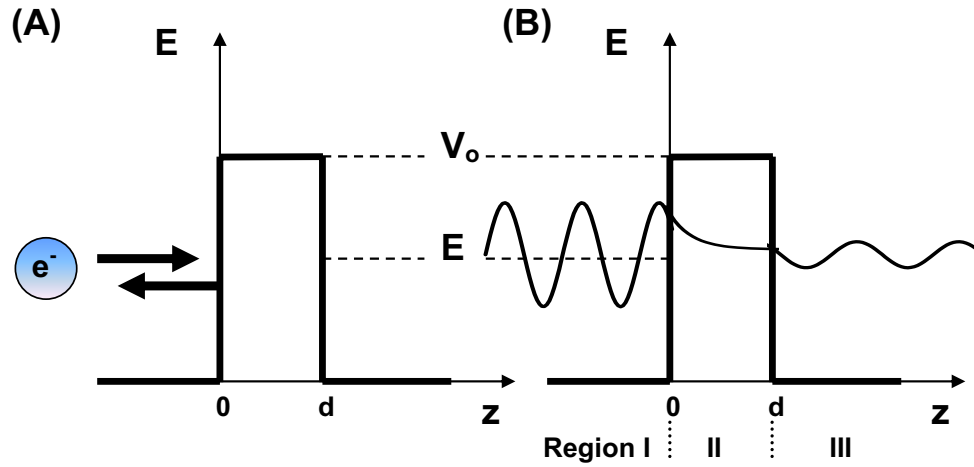
Figure 2.1: Tunnel effect in one dimension. (A) In classical mechanics an electron (e$^-$) of energy E is reflected by a potential barrier V_0 if $E < V_0$; (B) in quantum physics the probability of the electron wave to traverse the potential barrier is non-zero.

The electron motion is govern by the Schrödinger equation,

$$i\frac{\partial}{\partial t}\Psi\left(\vec{z},t\right) = H\Psi\left(\vec{z},t\right), \tag{2.1}$$

where H is the Hamiltonian of the system. The Hamiltonian for a simple tunnel junction consists of a kinetic energy part $-\frac{\hbar^2}{2m}\frac{\partial^2}{\partial z^2}$ and a potential

energy part $V\left(\vec{z}\right)$ The potential energy V is

V=0 in Region I,   z <0

V=V$_0$ in Region II, $0 < z < $ d

V=0 in Region III,   z $> $ d.

The wave function $\Psi\left(\vec{z},t\right)$ of the electron is a solution of the equation

$$i\frac{\partial}{\partial t}\Psi\left(\vec{z},t\right) = -\frac{\hbar^2}{2m}\frac{\partial^2}{\partial z^2}\Psi\left(\vec{z},t\right) + V\left(\vec{z}\right)\Psi\left(\vec{z},t\right) = \left(-\frac{\hbar^2}{2m}\frac{\partial^2}{\partial z^2} + V\left(\vec{z}\right)\right)\Psi\left(\vec{z},t\right).$$
(2.2)

The probability to find a particle described by the wave function $\Psi\left(\vec{z},t\right)$ at the position $\vec{z}$ at the time t is

$$P\left(\vec{z},t\right) = \Psi\left(\vec{z},t\right)\Psi^*\left(\vec{z},t\right) = \left|\Psi\left(\vec{z},t\right)\right|^2.$$
(2.3)

To simplify the calculation we consider the one dimensional case of a tunneling barrier with a potential independent of time. The wave function $\Psi\left(\vec{z},t\right)$ is written as the product of $\Psi_z\left(z\right)\Psi_t\left(t\right)$. Eq. 2.2 then can be separated as

$$\frac{\hbar^2}{2m}\frac{\partial^2\Psi_z\left(z\right)}{\partial z^2} + \left(E - V\left(z\right)\right)\Psi_z\left(z\right) = 0.$$
(2.4)

There are three solutions to this Schrödinger equation:

Region I

$$\Psi_z\left(z\right) = A\exp\left(\frac{ipz}{\hbar}\right) + B\exp\left(-\frac{ipz}{\hbar}\right), \quad z < 0$$
(2.5)

Region II

$$\Psi_z\left(z\right) = C\exp\left(kz\right) + D\exp\left(-kz\right), \quad 0 \le z \le d$$
(2.6)

Region III

$$\Psi_z\left(z\right) = AS\left(E\right)\exp\left(\frac{ip(z-d)}{\hbar}\right), \quad z > d$$
(2.7)

where $p = \sqrt{2mE}$, $\hbar k = \sqrt{2m\left(V - E\right)}$. For a detailed treatment of the

problem see Baym [9]. At the boundaries of the three regions, these functions and their first derivatives must be continuous. The function $S(E)$ is called the tunneling matrix element. It is a measure for the probability to tunnel from left to right for a particle being present at the left side of the junction. Satisfying the boundary conditions in Eq. 2.5-2.7 leads to four simultaneous equations for the five parameters A, B, C, D, S(E). We can chose an arbitrary value for the amplitude of the incoming electron wave, hence we set A = 1. The tunneling matrix element is for $E < V$:

$$S\left(E\right) = \frac{2i\hbar kp}{2i\hbar kp \cosh(kd) + (p^2 - \hbar^2 k^2)\sinh(kd)}.\qquad(2.8)$$

The tunneling barrier has both a transmissivity and a reflectivity. In a measurement of the tunneling current, we can only detect the transmissivity, which is given by

$$T\left(E\right) = |S\left(E\right)|^2 = \left[1 + \frac{\sinh^2(kd)}{4(E/V)(1 - E/V)}\right]^{-1}.\qquad(2.9)$$

This equation can be simplified for electrons with a de Broglie-wave length much smaller than the barrier, width d, or kd≫1. Eq. 2.9 becomes

$$T\left(E\right) \approx 16\frac{E}{V}\left(1 - \frac{E}{V}\right)\exp\left(-2kd\right) = 16\frac{E}{V}\left(1 - \frac{E}{V}\right)\exp\left(-\frac{2d}{\hbar}\sqrt{2m(V - E)}\right).$$
$$(2.10)$$

To get a feeling for the magnitude of the transmission coefficient T(E) we use values for V and E typical for a metal. The zero point of the energy scale is at the bottom of the valence band for a metal, which is typically 8 eV below the Fermi energy. All electron states between the bottom of the valence band and the Fermi energy are filled, at zero temperature. The barrier height is, for a clean metal surface, about 4 eV above the Fermi energy, hence $V = 12$ eV. We further assume that the tunneling barrier width is d = 1 nm. Using these values we get T(E)=10^{-9} for electrons at the Fermi energy. Figure 2.2 shows the transmission of the tunnel barrier as a function of the electron energy E for the above values of V and d.
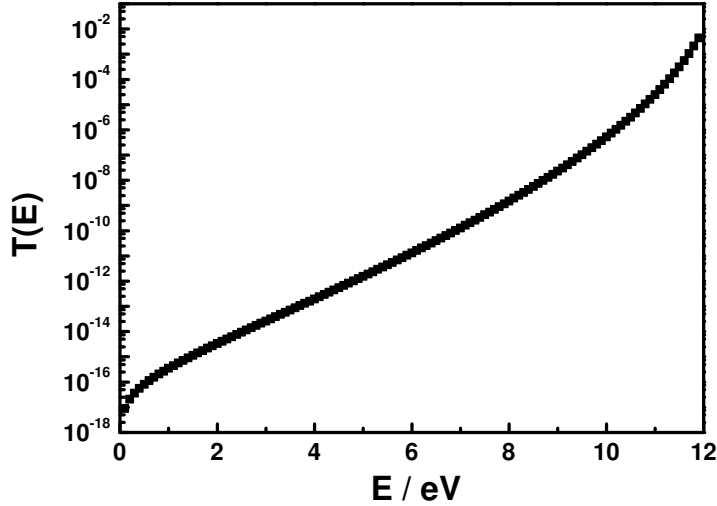
Figure 2.2: The transmission coefficient as a function of the electron energy. The zero energy corresponds to an electron at the bottom of the valence band. The Fermi energy for this calculation is set to 8 eV and the work function is 4 eV.

2.1.2   Tip-surface interaction model

In the previous section we have seen that there is some probability T(E) that the electron can penetrate the barrier, in spite of the fact that according to the classical approach it is not possible. STM is fully benefited by this fact. A small metal tip, which is simply a sharpened metallic wire, is brought near enough to the conducting surface of a sample. The lateral tip position (x, y axis) and the tip-sample distance d are controlled with picometer precision by means of voltage signals applied to piezo-electric material. If the tip is brought close enough to the sample that the wave functions of the conduction electrons of tip and sample begin to overlap substantially, a measurable tunneling current, I, flows between the biased sample[1] and the tip. The tip-sample distance in typical tunneling experiments is about 5-10 Å . Since the tunneling current depends exponentially on the tip-sample distance, it mainly flows through the few atoms at the very apex of the tip.

---

[1]potential, U_{bias}, with respect to the ground

Thus the tunneling current is highly localized, leading to the atomic-scale resolution of STM. The tip scans the surface in two dimensions, while its height is adjusted to maintain a constant tunneling current. The result is essentially a contour map of the surface.

However, the interpretation of STM measurements is based on an approach different from the wave matching method, see Sec. 2.1.1 . To describe a tunnel current Bardeen used first-order time-dependent perturbation theory [10]. Instead of calculating the Schrödinger equation of the coupled system Bardeen's approach derives the tunnel current from the overlap of the wave functions of the two electrodes. Tersoff and Hamann were the first to apply Bardeen's transfer Hamiltonian to tunnel experiments with STM [11]. They approximated a locally spherical symmetry for the tip and allowed only s-type wave functions to contribute to the tunnel matrix element. In the limit of low temperature T and small applied bias voltage U_{bias} between tip and sample, the tunnel current, I, is described by

$$I = 32\pi^3 \hbar^{-1} e^2 U_{bias} \phi^2 \rho_t \left(E_F\right) R^2 k^{-4} e^{2kR} \sum_s |\psi_s \left(\vec{r}_0\right)|^2 \delta \left(E_s - E_F\right), \quad (2.11)$$

where $k = \hbar^{-1}\sqrt{2m\phi}$, ρ_t is the density of states per unit volume of the probe tip, ϕ is the work function (for simplicity we assume that the work function of the tip is equal to that of the sample), E_F is the Fermi energy, r_0 and R are related to the geometry of the tip as drawn in Figure 2.3.

The last term of Eq. 2.11 sums the sample wave functions of discrete electronic states E_s. The expression can be described as the surface density of states ρ_s at the Fermi energy. Since the wave functions decay exponentially into the vacuum one can derive that the tunnel current depends exponentially on the distance, d, between the tip and the sample [11]:

$$I \propto \exp^{-2kd}. \qquad (2.12)$$

Within the limit of small bias voltages the tunneling current may be interpreted as proportional to the sample density of states. At larger bias voltages
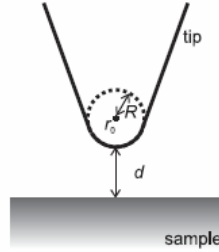
Figure 2.3: Geometry of the tunneling tip in the Tersoff-Hamann model. Probe tip has arbitrary shape but is assumed locally spherical with radius of curvature R. Distance of the nearest approach is d. Center of curvature of tip is labeled r_0.

the tunnel current is represented by a weighted integral over a range of energies,

$$I \propto \int_0^{eU} \rho_s(E)\rho_t(E, eV)T(E, eU)dE, \tag{2.13}$$

where

$$T(E, eU) = \exp\left[-\frac{2d}{\hbar}\sqrt{m(\phi_s + \phi_t + eU - 2E)}\right]. \tag{2.14}$$

Figure 2.4 illustrates the tunneling junction between tip and sample in equilibrium and with applied sample bias voltage $(eU)^2$. The occupied states bellow the Fermi energy are indicated in gray color and the sample density of states is shown by the black curve. In equilibrium, the net tunnel current is zero, see Figure 2.4A. At negative sample bias voltage, U, electrons from the sample in the range from $E_F - eU$ to E_F can tunnel into unoccupied states of the tip, Figure 2.4B, and vice versa for $U > 0$, Figure 2.4C.

STM allows us to experimentally investigate the surface structure or topography of a sample by taking the advantage of the exponential dependence of the tunneling current I on d. A difference in tip height of 1 Å leads to a variation in the tunnel current, I, of about one order of magnitude. This is the reason for the high vertical resolution of the STM. One can get atomic resolution even with a not well shaped tip.

There are two commonly used operating modes: the constant-height and

---

[2]sometimes bias voltage, U, is denoted as U_{bias}
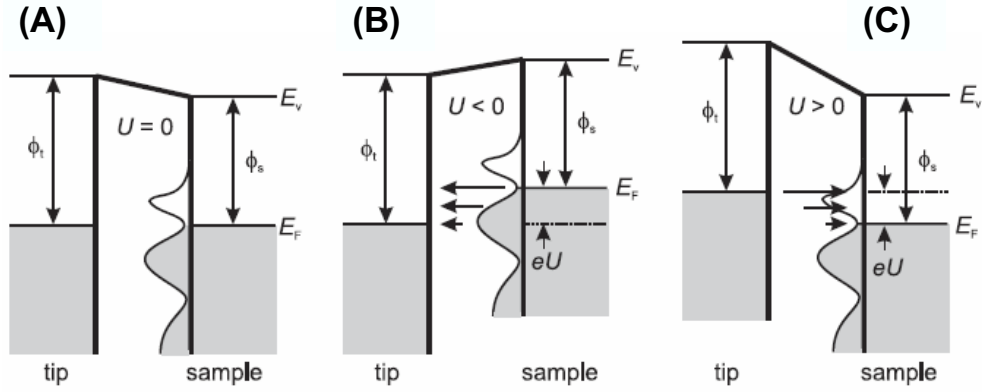
Figure 2.4: Tunneling junction. (A) in equilibrium, no net current; (B) For negative bias voltages, net current flows from sample to the tip (arrows show the direction of the net current); (C) for positive bias, net current flows from tip to sample [12].
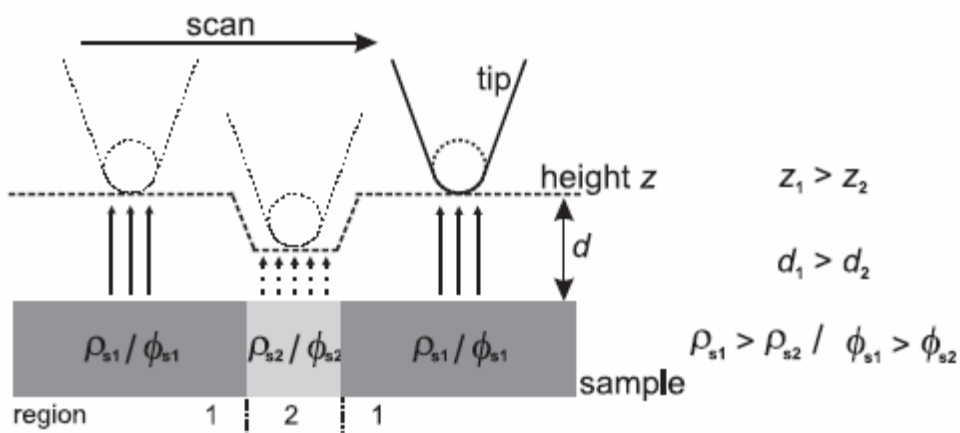
the constant-current mode, see Figure 2.5. In the constant-height mode, see Figure 2.5A, the the tip can be rapidly scanned across the sample surface at constant height while a feedback loop, see Sec. 2.1.3 is slowed or turned off completely. As a result, the variation of tunnel current between tip and sample is recorded as a function of position x, y. Since d_1 is larger than d_2 in this example the tunnel current I_1 is smaller than I_2 at a given bias voltage U. In the constant-current mode, Figure 2.5B, the feedback loop forces the tip to change the height z to keep the current constant. This means that the z-position of the tip has to be adjusted during scanning which is done by applying an appropriate voltage U_z to the z-piezo of the tube scanner. By recording the height of the tip z as a function of lateral position, a topographical images can be obtained.

Interpreting STM image data is not as straightforward as it looks at first glance. For instance let us take a sample with a plane surface having two regions with different local density of states ρ_s or work function ϕ_s. In region 1 with a density of states ρ_{s1} or the a work function ϕ_{s1} the tunneling current is I_1 at a tip sample distance d_1, Figure 2.6. During scanning feedback tries to keep the tunnel current constant ($I_1=I_2$), therefore the tip has to be moved closer to the sample surface in region 2 due to the reduced density of states ρ_{s2}
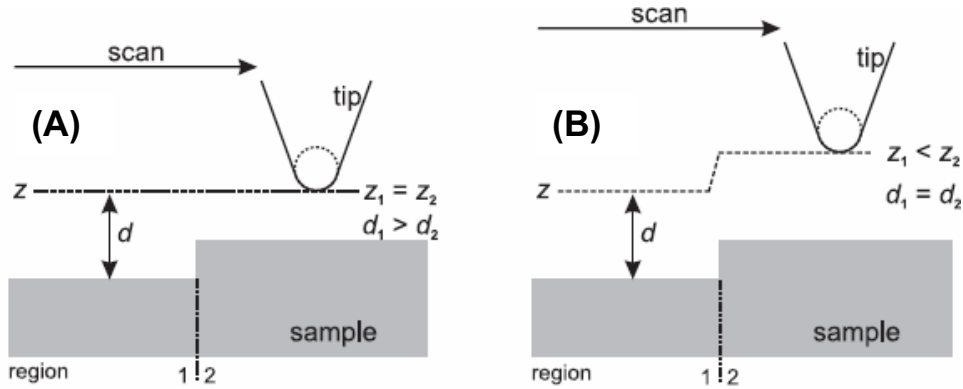
Figure 2.5: Operating modes of STM. (A) the constant-height mode ($z_1=z_2=$const), measurement of the variation of tunnel current as a function of position x, y. in the scan direction; (B) the constant-current mode ($I_1=I_2=$const), measurement of the height z of the tip [12].

or work function ϕ_{s2} in that surface area. As a result one finds a depression in the topography image z(x,y) in the region 2 in comparison with region 1, although the surface is completely flat. This phenomenon is referred to as the "topographic effect".

Figure 2.6: The "Topographic effect": sample areas with different local density of states ρ_{s2} or work function ϕ_{s2} can lead in a variation in tip height z when operating in the constant-current mode even though surface is flat (the number and strength of the arrows illustrate the tunnel current density) [12].

2.1.3   Experimental realization of STM

The schematic experimental realization of STM is shown in Figure 2.7. In order to investigate sample properties by measuring tunnel currents several requirements have to be met. First of all, sample must be conductive as well as a sharp probe tip which scans the surface. The width of the insulating tunnel barrier has to be of the order of a few Angstroms (Å) to obtain measurable tunnel current (typically in the range of 0.1-10 nA). The tunnel current is established and sensed by a special preamplifier (IVC) which converts current into voltage, see Figure 2.7. Since the tunneling current is exponentially dependent on distance between the tip and the sample, a logarithmic amplifier is used to linearize the signal. This logarithmic amplifier is followed by an comparator for the setpoint current. Scan of tip over the surface has to be controlled very well in order to avoid crash and mechanical contact. Piezoelectric tube scanners are used to control the tip position and movement with the precision needed at atomic scale. The piezoelectric tube scanners have four separate electrodes which are connected to a X/Y scan generator. By applying a voltage via a high voltage amplifier to two opposite sector electrodes, the piezo tube elongates in x,y-directions. The elongation is proportional to applied voltage. The X/Y scan generator serves as a source for the x and y raster voltages. The vertical motion of the tube is controlled by the inner electrode, z, which is driven by the feedback system. In this way, fine adjustments of the distance between sample and tip is achieved. Experimental set-up has to be very rigid and a lot of care has to be taken to reduce mechanical instabilities and vibrations including vibration isolation system. The STM control, data acquisition and real-time display is controlled by a personal computer via the analog/digital interface 16-bit converter.

2.2   Photoelectron Spectroscopy

Photoelectron spectroscopy(PES) is based on the phenomenon of photoemission which was detected by Hertz in 1887. In 1905 Einstein proposed the concept of "photon" and explained the photoelectric effect using the following
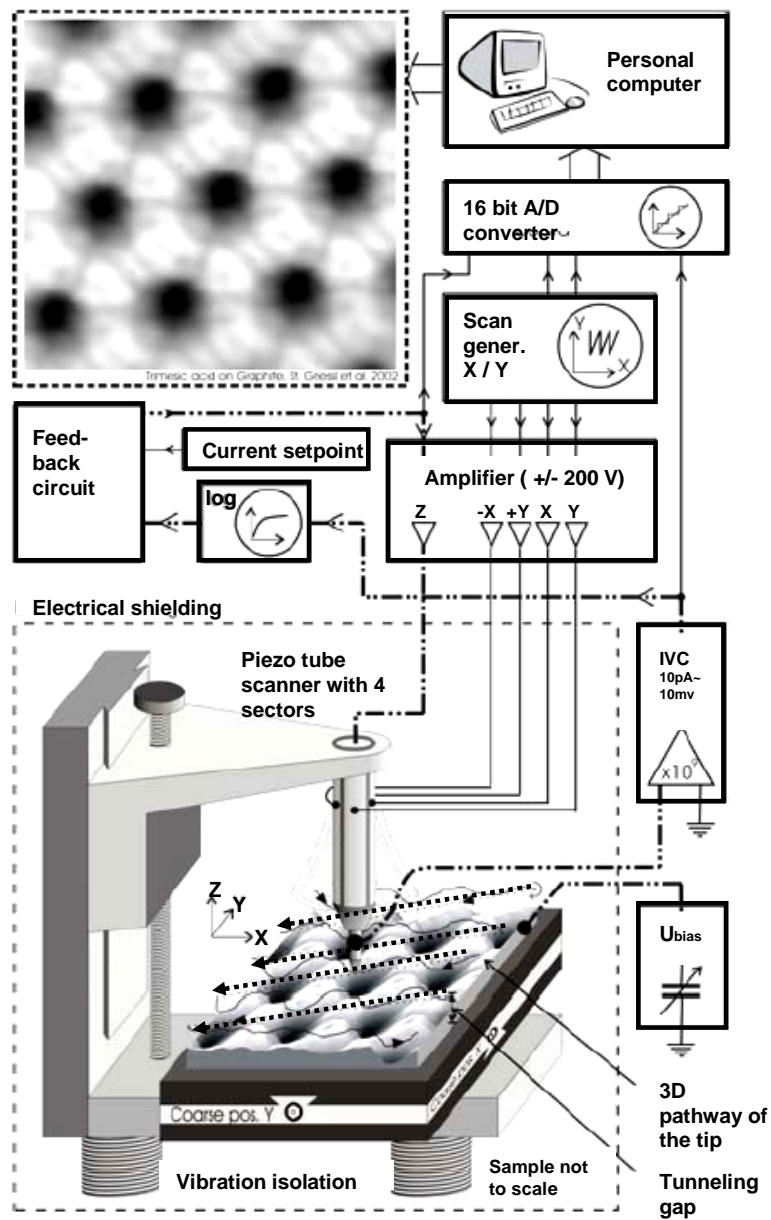
Figure 2.7: STM system block diagram [13].

simple formula:

$$E_k = hv - E_B - \Phi,$$

where E_k is kinetic energy of photoelectron, hv is the photon energy, E_B is binding energy of the electron, and Φ is work function of the material. Though the main point of this formula is that the energy of light is quantized, in view of experiment, this also says that if we use this "photoelectron effect" we can know the electron energy state inside the material. That is, we can know the electronic structure of the matter.

2.2.1   X-ray Photoelectron Spectroscopy (XPS)

XPS is Photoelectron spectroscopy using X-ray as a photon source. The energy range of X-ray in XPS is usually more than 1000 eV. X-ray of this energy range can be obtained by using a characteristic X-ray line spectrum, which is due to transitions of electrons from high energy states to lower ones. When an atom is bombarded by high energy electrons, some inner atomic electrons are sometimes knocked out, leaving vacancies in the inner shell. These vacancies are filled by electrons with other high energy states, in which process the X-ray emits the corresponding energy difference between these two states. Most widely used targets to obtain X-ray in XPS are Al and Mg.

### 2.2.2   Ultraviolet Photoelectron Spectroscopy (UPS)

UPS is one of the most useful tools to study the valence band structure of condensed matter. It usually uses the He I line ($hv = 21.22$ eV) or He II line ($hv = 40.8$ eV) as a photon source. Comparing with XPS, the resolution of the UPS is rather high (~meV), so this is adequate for studying band structures though it is more surface sensitive than XPS.

2.3 Electrochemical Methods

2.3.1 Potential Controlled Methods

Since this work deals with electrified solid/liquid interfaces, elucidating the electrochemical behavior of a system is of a major importance. For this aim, a current response as a function of time is recorded through a series of steps to different electrode potentials (E_i). The electrode potential is swept in a linear manner with time by a potentiostat which has the control of the voltage across the working electrode-counter electrode and it adjusts this voltage to maintain the potential difference between the working and the reference electrodes. One can view the potentiostat alternatively as an active element whose task is to force through the working electrode whatever current is required to achieve the desire potential at any time. Chemically, it is the flow of electrons needed to support the active electrochemical process at rates consistent with the potential. Usually the potential is swept at a constant sweep (scan) rate, v, between two limiting potentials E_1 and E_2, Figure 2.8. Thus, at any time the potential is:

$$
\begin{aligned}
0 < t < \tau, \quad & E(t) = E_i - vt, \\
t > \tau, \quad & E(t) = E_i - 2v\tau + vt.
\end{aligned}
\tag{2.15}
$$
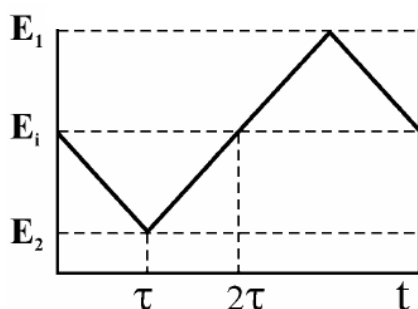
Figure 2.8: Cyclic voltammetry. The electrode potential is ramped between E_1 and E_2.

As a result one measures a current-voltage, $(i - E)$, response. The technique is known as cyclic voltammetry. Sometimes it is more informative to mea-

sure current-time, $(i - t)$, response known as chronoamperometry. However, understanding more quantitatively the size and shape of $i - E$ or $i - t$ response curves might not be a straightforward task. If we consider a simple one electron electrode reaction taking place on an interface solid/liquid,

$$O + ne^- \leftrightarrows R,$$
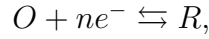
the electrochemical response can be affected quite significantly by different processes such as mass transfer, adsorption and charge transfer of the species O or R.

2.3.2   Electrode reactions driven by mass-transfer

This is the simplest case in which all other processes are very rapid compared to the mass-transfer processes. The net rate of the electrode reaction, v_{nr}, is then governed totally by the rate at which the electroactive species is brought to the surface by mass transfer, v_{mt}

$$v_{nr} = v_{mt} = \frac{i}{nFA}, \tag{2.16}$$

where F is the Faraday constant, A is area of electrode. The modes of mass transfer are: *migration* - movement of a charged species under a gradient of electrical potential; *diffusion* - movement of a species under the influence of chemical potential (concentration gradient); and *convection* - stirring and hydrodynamic transport.
Mass transfer to an electrode is governed by

$$J_j = - \left(\frac{C_j D_j}{RT} \right) grad\overline{\mu}_j, \tag{2.17}$$

written for one-dimensional linear mass transfer along the x-axis, including convection [2]

$$J_j(x) = -D_j \frac{\partial C_j(x)}{\partial x} - \frac{z_j F}{RT} C_j D_j \frac{\partial \phi(x)}{\partial x} + C_j v(x), \tag{2.18}$$

is known as the *Nernst-Planck* equation, where $J_j(x)$ is the flux of species j (mol s^{-1}cm^{-2}) at distance x from the surface, D_j is the diffusion coefficient (cm^2/s), $\frac{\partial C_j(x)}{\partial x}$ is the concentration gradient at distance x, $\frac{\partial \phi(x)}{\partial x}$ is the potential gradient, z_j and C_j is the charge and concentration of species j, and $v(x)$ is the velocity with which a volume element in solution moves along the axis.

If species j is charged, then the flux, J_j, is equivalent to a current density. Let us consider a linear system with a cross sectional area, A, normal to the axis of mass flow. Then,

$$- J_j = \frac{i_j}{z_j FA} = \frac{i_{d,j}}{z_j FA} + \frac{i_{m,j}}{z_j FA}, \tag{2.19}$$

with

$$\begin{aligned} \frac{i_{d,j}}{z_j FA} &= D_j \frac{\partial C_j}{\partial x} \\ \frac{i_{m,j}}{z_j FA} &= \frac{z_j F D_j}{RT} C_j \frac{\partial \phi}{\partial x}, \end{aligned} \tag{2.20}$$

where $i_{d,j}$ and $i_{m,j}$ are diffusion and migration currents of species j, respectively. At any location in solution, the total current, i is made up of contributions of all species, $i = \sum_j i_j$ and

$$i = \frac{F^2 A}{RT} \frac{\partial \phi}{\partial x} \sum_j z_j^2 D_j C_j + FA \sum_j z_j D_j \frac{\partial C_j}{\partial x}. \tag{2.21}$$

The relative contribution of migration (first term) to the total current can be neglected if the concentration of the counter ions is high enough. In this case we can consider the situation where the electroactive species are transported purely by diffusion at the electrode surface and in which the process controls the faradaic current flowing in the external circuit. The pure diffusion problem is well described by the Flick's first law which states that the flux is proportional to the concentration gradient $\frac{\partial C_j(x)}{\partial x}$. For example the flux of a substance O at a given location x and time t written as $Jo(x,t)$ according to the Flick's first law is

$$- J_O(x,t) = D_O \frac{\partial C_O(x,t)}{\partial x}. \tag{2.22}$$

The Flick's second law pertains to the change in concentration of O with time

$$\frac{\partial C_O(x,t)}{\partial t} = D_O \left(\frac{\partial^2 C_O(x,t)}{\partial x^2} \right).$$ (2.23)

To get an expression which gives the general current-potential characteristics one has to solve Eq. (2.23) under the following conditions:

(a) Initial conditions

If O is uniformly distributed throughout the solution at a bulk concentration C_O^* at the start of the experiment, the initial condition (for all x) is

$$C_O(x,0) = C_O^*,$$ (2.24)

and If R is initially absent from the solution, then

$$C_R(x,0) = 0.$$ (2.25)

(b) Semi-infinite boundary conditions

The electrochemical cell is usually large compared to the length of diffusion; hence one can assume that at large distances from the electrode $(x \to \infty)$ the concentration reaches a constant value, typically the initial concentration, so that

$$\lim_{x \to \infty} C_O(x, t \geq 0) = C_O^*,$$
$$\lim_{x \to \infty} C_R(x, t \geq 0) = 0.$$ (2.26)

Additional boundary conditions usually relate to concentrations or concentration gradient at the electrode surface as a function of the applied potential:

$$C_O(0, t > 0) = f(E_i - vt),$$
$$\frac{C_O(0,t>0)}{C_R(0,t>0)} = f(E_i - vt).$$ (2.27)

The concentrations of O and R at the electrode surface can be assumed to be at equilibrium with the electrode potential, as governed by the Nernst equation for the half-reaction

$$\theta(t) = \frac{C_O(x = 0, t > 0)}{C_R(x = 0, t > 0)} = \exp\left[\frac{nF}{RT} \left(E_i - vt - E^0 \right) \right],$$ (2.28)

Such a process which follows Eq. 2.28 or an equation derived from it is called a nernstian. This is often said to be thermodynamically or electrochemically reversible.

Also, the mass conservation requires that the flux of species R is equal to the flux of O at the electrode. So,

$$D_O \left[\frac{\partial C_O(x,t)}{\partial x} \right]_{x=0} = -D_R \left[\frac{\partial C_R(x,t)}{\partial x} \right]_{x=0}. \tag{2.29}$$

The calculation of $i - t$ and $i - E$ characteristics involves the solution of Eq. 2.23 and the determination of the concentration profile. It can be shown that after Laplace transformation[3] Eq. 2.23 under the (a) and (b) conditions one yields the following solution [2]:

$$\overline{C}_O(x,s) = \frac{C_O^*}{s} - \frac{C_O^*}{s} e^{-\sqrt{\frac{s}{D_O}}x}, \tag{2.30}$$

Inverse Laplace transformation of 2.30 gives

$$C_O(x,t) = C_O^* \left\{ 1 - erfc \left[\frac{x}{2(D_O t)^{1/2}} \right] \right\}. \tag{2.31}$$
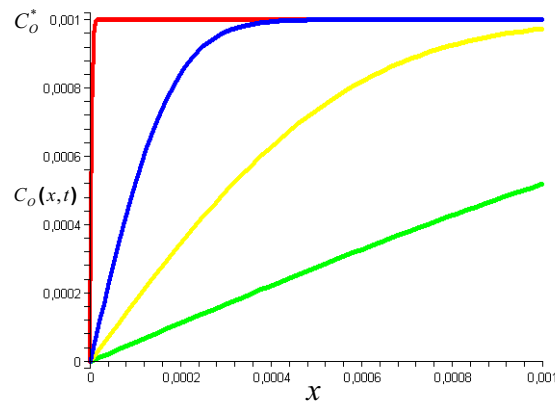
Figure 2.9: Concentration profiles for D_O=1x10^{-5} cm^2/s, C_O^*=1 mM for several times (1x10^{-6} s red; 1x10^{-3} s blue; 1x10^{-2} s yellow; 1x10^{-1} s green).

---

[3] By definition Laplace transformation of a function, $F(t)$, is $L\{F(t)\} \equiv \int_0^\infty e^{-st} F(t) dt$

The flux at the electrode surface is proportional to the current

$$- J_O(0, t) = \frac{i(t)}{nFA} = D_O \left[\frac{\partial C_O(x, t)}{\partial x} \right]_{x=0}.$$ (2.32)

The derivative in Eq. 2.32 can be evaluated from Eq. 2.30. Substitution and inversion produces the current-time response, $i - t$

$$i_d(t) = \frac{nFAD_O^{1/2}C_O^*}{\pi^{1/2}t^{1/2}}.$$ (2.33)

which is known as a Cottrell equation, see Figure 2.10. The Eq. 2.33 is a special case for the diffusion-limited region which requires a very negative $E - E^0$, so that $\theta \to 0$. The general response function for a potential step experiment in a reversible system is [2]

$$i(t) = \frac{nFAD_O^{1/2}C_O^*}{\pi^{1/2}t^{1/2} \left[1 + \left(\frac{D_O}{D_R} \right)^{1/2} \theta \right]} = \frac{i_d(t)}{1 + \left(\frac{D_O}{D_R} \right)^{1/2} \theta}.$$ (2.34)

Now we see that for a reversible couple, every $i - t$ curve has the same shape but its magnitude is scaled by $1 / \left[1 + \left(\frac{D_O}{D_R} \right)^{1/2} \theta \right]$ according to the potential to which the step is made. For very positive potentials (relative to $E^0 v$), this scale factor is zero; thus $i(t)$ has a value between zero and $i_d(t)$, depending on E.
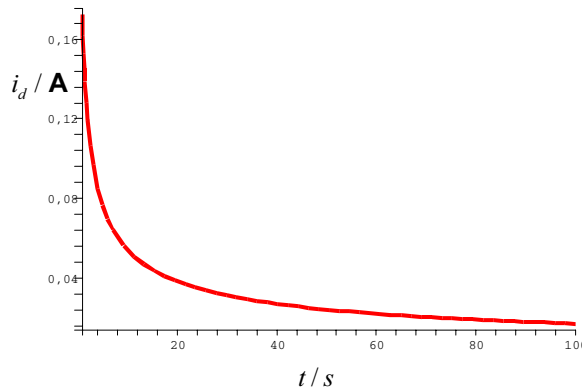
Figure 2.10: Cottrell behavior of the diffusion current with time.

Solution of Eq. 2.23 for the time dependent boundary conditions imposed by the rapid potential scan, v, requires numerical integration. Nevertheless, it can be shown [2] that the $i - E$ characteristic for a reversible process at a planar electrode initially in absence of R obeys the relation for the peak current, i_p

$$i_p = 0.446 n^{3/2} \left(\frac{F^3}{RT} \right)^{1/2} A C_O^* D_O^{1/2} v^{1/2}. \tag{2.35}$$

The general dependence of $i - E$ is shown schematically in Figure 2.11 with cyclic voltammogram computed using the numerical methods of Nicholson and Shain [14].
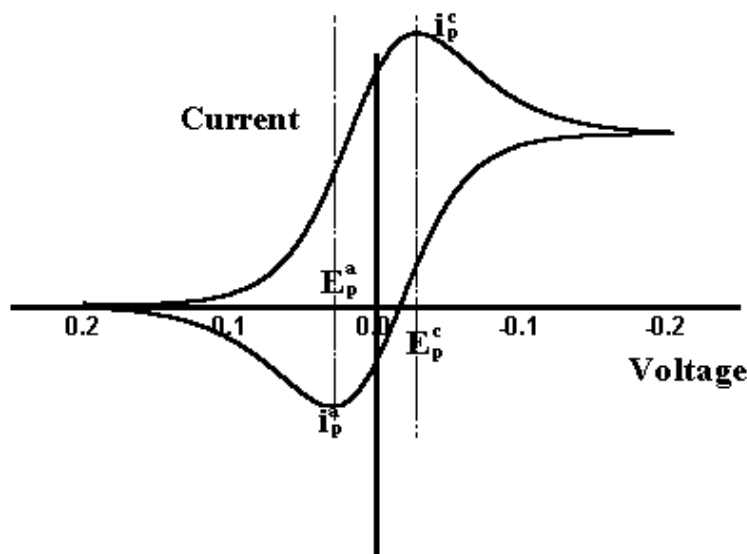
Figure 2.11: Typical cyclic voltammogram of a nernstean reversible reaction controlled by semi-infinite linear diffusion to a planar electrode; i_p^c and E_p^c are peak current and peak potential for the cathodic process (the letters "c" and "a" stand for cathodic and anodic processes).

It should be noted that i_p is proportional to C_O^* and the sweep rate $v^{1/2}$. Also, from the slope of i_p vs. $v^{1/2}$ one can estimate the diffusion coefficient D_O.

2.3.3   Electrode reactions driven by adsorption

The electrochemical response ($i - E$ curve) for the electrode reaction $O + ne^- \leftrightarrows R$ can be affected quite significantly by the adsorption of R or O. The treatment of such problems is more complicated because one must choose an adsorption isotherm which involves the introduction of additional parameters and, in general, nonlinear equations. Suppose that O and R are adsorbed on the electrode surface with surface concentrations $\Gamma_O(t)$ and $\Gamma_R(t)$ and that electrode process consists of the complete reduction/oxidation of O and R on the forward/reverse sweep. The current is not diffusion-controlled but is limited by the amount of the adsorbed material.

The equations describing the process include the same ones as used previously, namely the mass-transfer Eq. 2.23 and the initial and semi-infinite conditions [(a) and (b)]. However, the flux conditions at the electrode are different. The general flux equation is then

$$- J_O(0,t) - \frac{\partial \Gamma_O(t)}{\partial t} = - \left[-J_R(0,t) - \frac{\partial \Gamma_R(t)}{\partial t} \right] = \frac{i(t)}{nFA}. \qquad (2.36)$$

Initial conditions at t=0 must also be supplied

$$\begin{aligned} \Gamma_O &= \Gamma_O^* \\ \Gamma_R &= 0. \end{aligned} \qquad (2.37)$$

The relationship between the amount of substance j adsorbed on the electrode surface, Γ_j, the activity in the bulk solution, a_j^b, and the electrical state of the system, E, at a given temperature, is given by the adsorption isotherm. This is obtained from the condition of equality of electrochemical potential for the bulk and adsorbed species j at equilibrium,

$$\bar{\mu}_j^A = \bar{\mu}_j^b, \qquad (2.38)$$

where the superscripts A and b refer to adsorbed j and bulk j, respectively. Thus

$$\bar{\mu}_j^{0,A} + RT \ln a_j^A = \bar{\mu}_j^{0,b} + RT \ln a_j^b, \qquad (2.39)$$

where the $\bar{\mu}_j^0$ terms are the standard electrochemical potentials. The standard free energy of adsorption, $\Delta \bar{G}_j^0$, which is a function of the electrode potential, is defined by

$$\Delta \bar{G}_j^0 = \Delta \bar{\mu}_j^{0,A} - \Delta \bar{\mu}_j^{0,b}. \tag{2.40}$$

Thus

$$a_j^A = a_j^b \exp^{\frac{-\Delta \bar{G}_j^0}{RT}} = k_j a_j^b \tag{2.41}$$

Eq. 2.41 is the general form of an adsorption isotherm, with a_j^A being a function of a_j^b and k_j. Different specific isotherm result from different assumptions or models for the relationship between a_j^A and Γ_j. Most frequently, one assumes the Langmuir isotherm.

The Langmuir isotherm involves assumption of (a) no interactions between the absorbed species on the electrode surface, (b) no heterogeneity of the surface, and (c) at high bulk activities, saturation coverage of the electrode by adsorbate (e.g., to form a monolayer) of amount $\Gamma_{j,S}$. Thus

$$\frac{\Gamma_j}{\Gamma_{j,S} - \Gamma_j} = k_j a_j^b. \tag{2.42}$$

Isotherms can be written in terms of the fractional coverage of the surface, $\theta = \frac{\Gamma_j}{\Gamma_{j,S}}$. The Langmuir isotherm in this form is :

$$\frac{\theta}{1 - \theta} = k_j a_j^b. \tag{2.43}$$

The Langmuir isotherm also can be written in terms of the concentration of species j in solution by including activity coefficients in the k_j term. This yields

$$\Gamma_j = \frac{\Gamma_{j,S} k_j C_j}{1 + k_j C_j}. \tag{2.44}$$

For the reaction $O + ne^- \leftrightarrows R$ we assume that the electroactive species R and O obey Langmuir isotherms, so that

$$\Gamma_O(t) = \frac{k_O \Gamma_{O,S} C_O(0,t)}{1 + k_O C_O(0,t) + k_R C_R(0,t)}, \tag{2.45}$$

and we also assume that within the range of potentials of the wave, the Γ's are independent of E. Eq. 2.36 becomes

$$-\frac{\partial \Gamma_O(t)}{\partial t} = \frac{\partial \Gamma_R(t)}{\partial t} = \frac{i(t)}{nFA}. \qquad (2.46)$$

Eq. 2.46 implies that reduction of adsorbed O produces adsorbed R with no adsorption or desorption occurring during the scan. In order to include Langmuir type of adsorption we have to include Eq. 2.45 written for O and R

$$\frac{\Gamma_O(t)}{\Gamma_R(t)} = \frac{k_O \Gamma_{O,S} C_O(0,t)}{k_R \Gamma_{R,S} C_R(0,t)} = \frac{k_{O,S} C_O(0,t)}{k_{R,S} C_R(0,t)}, \qquad (2.47)$$

with $k_{O,S} = k_O \Gamma_{O,S}$, $k_{R,S} = k_R \Gamma_{R,S}$. If the reaction is nernstian, the surface concentrations are related as:

$$\frac{C_O(0,t)}{C_R(0,t)} = \exp\left[\frac{nF}{RT}\left(E - E^0\right)\right]. \qquad (2.48)$$

Then Eq. 2.47 yields

$$\frac{\Gamma_O(0,t)}{\Gamma_R(0,t)} = \frac{k_{O,S}}{k_{R,S}} \exp\left[\frac{nF}{RT}\left(E - E^0\right)\right]. \qquad (2.49)$$

From Eq. 2.46, Eq. 2.49 and the fact that $\Gamma_O + \Gamma_R = \Gamma_O^*$ one yields:

$$\frac{i(t)}{nFA} = -\frac{\partial \Gamma_O(t)}{\partial t} = \left[\frac{\partial \Gamma_O(t)}{\partial E}\right] v, \qquad (2.50)$$

and with $E = E_i - vt$ the equation for the $i - E$ curve is obtained:

$$i = \frac{n^2 F^2}{RT} \frac{vA\Gamma_O^*(k_{O,S}/k_{B,S})\exp\left[(nF/RT)\left(E - E^0\right)\right]}{\left\{1 + (k_{O,S}/k_{B,S})\exp\left[(nF/RT)\left(E - E^0\right)\right]\right\}^2} \qquad (2.51)$$

A typical $i - E$ curve is presented in Figure 2.12.
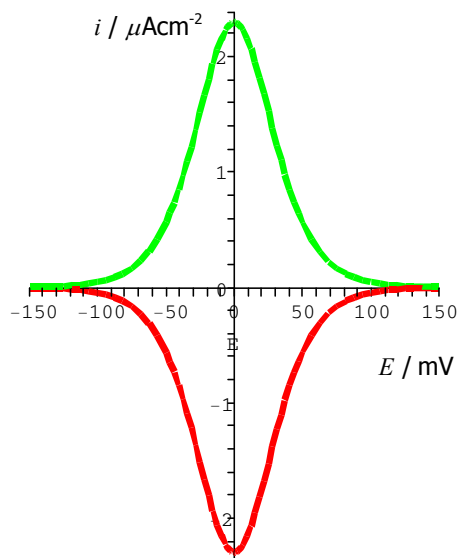
Figure 2.12: Cyclic voltammogram for adsorption process. Current is given in normalized form.

The peak current is given by

$$i_p = \frac{n^2 F^2}{4RT} v A \Gamma_O^*. \tag{2.52}$$

The peak current, and indeed the current at each point on the wave is proportional to v, in contrast to the $v^{1/2}$ observed for the nernstian waves of diffusing species.

2.4 Monte Carlo (MC) simulations of lattice-gas models in interfacial electrochemistry

The Monte Carlo(MC) method is particularly well suited to the study of fluctuations and phase transitions in two dimensional (2D) systems of ions, atoms or molecules at or near a solid/liquid interface characterized by specific chemisorption at well-defined sites on it. Monte Carlo simulation of lattice-gas models as a tool for understanding interfacial electrochemistry is a main topic of this chapter and it is described briefly. Detailed aspects of this

approach can be found in the literature [15, 16, 17, 18].

2.4.1   Lettice-gas models of chemisorption

MC simulations of lattice-gas models of chemisorption have many advantages in comparison with many mean-field techniques ranging from the simple Langmuir isotherm (see, Sec. 2.3.3) to more complex ones such as Frumkin and Temkin isotherms. First of all, mean-field methods are really not very accurate for most 2D systems, because they ignore the special structure of the system. Therefore, a lot of nontrivial amount of work and attention goes into implementing enough of this structure to give accurate results. In contrast, MC codes take special structure into account. In addition, MC simulations are not only limited to the study of equilibrium properties but also they provide a tool to study time dependent phenomena and dynamic properties of the system. These simulations can be used to obtain numerical results for such experimentally measurable quantities as adsorption isotherms, voltammetric currents and charge densities and images obtained by high resolution STM.

Implementation of structure of the lattice-gas models assumes that adsorption is only allowed on a discrete lattice of adsorption sites. The concentration of adsorbate at site i, c_i is 1 if the site is occupied by the adsorbate and 0 otherwise. The energy of a particular configuration of occupied sites, **c**, is is given by the grand-canonical lattice-gas Hamiltonian

$$H(c) = -\bar{\mu} \sum_i c_i - \sum_n \left(J^{(n)} \sum_{<ij>}^{(n)} c_i c_j \right) - H_{trios+}(c). \qquad (2.53)$$

The electrochemical potential of the adsorbate in solution is $\bar{\mu}$ and the first term of on the right-hand side is the free energy of adsorption when adsorbate-adsorbate interactions are ignored. The next term represents all paired adsorbate-adsorbate interactions. The index n indicates the separation between sites, e.g., $n = 1$ indicates nearest neighbors, whereas $\sum_{<ij>}^{(n)}$ indicates the sum over all pairs of neighbors of rank n. The pair interaction

energy between adsorbate particles which occupy nth nearest neighbor sites is $J^{(n)}$. Trios and higher order interactions are including in H_{trios+} therm. By definition $\bar{\mu} > 0$ denotes a tendency for adsorption in the absence of lateral interactions, and $J^{(n)} > 0$ represents effective attraction.

The connection of the theoretical lattice-gas to the applied electrode potential, E, that characterizes the experimental system, is made through the electrochemical potential

$$\bar{\mu} = \mu^0 + RT \ln \frac{a_A^b}{a_A^0} - zFE. \tag{2.54}$$

The binding energy of the absorbate, A, with the substrate is taken into account in the standard chemical potential, μ^0, which in this work is treated as adjustable model parameter.

The interesting thermodynamic property, which is a function of the electrochemical potential, is the surface coverage per adsorption site, defined as

$$\theta = N^{-1} \sum_i c_i, \tag{2.55}$$

where N is the total number of adsorption sites. Thus, one can find out how much charge, q, is adsorbed per adsorption site

$$q = -ez\theta. \tag{2.56}$$

A sign convention is used that reduction currents are negative.

Lattice-gas model approach allows us to describe systems which involve co-operative chemisorption of two different species, for instance A and B on the surface. The concentration of each component at site i is c_i^A and c_i^B with simultaneous adsorption of both species at one site forbidden. The lattice-gas

Hamiltonian for such a two-component system can be written as

$$H(c) = -\bar{\mu}_A \sum_i c_i^A - \bar{\mu}_B \sum_i c_i^A$$

$$-\sum_n \left[J_{AA}^{(n)} \sum_{<ij>}^{(n)} c_i^A c_j^A + J_{BB}^{(n)} \sum_{<ij>}^{(n)} c_i^B c_j^B + J_{AB}^{(n)} \sum_{<ij>}^{(n)} \left(c_i^A c_j^B + c_i^B c_j^A \right) \right] - H_{trios+}(c).$$

$$(2.57)$$

In this case the adsorbed charge density is

$$q = -e(z_A \Theta_A + z_B \Theta_B). \tag{2.58}$$

In the absence of diffusion and in the limit of vanishing potential scan rate, $i - t$ characteristic can be estimated in terms of the equilibrium lattice-gas response functions, $\frac{\partial \Theta_X}{\partial \bar{\mu}_X}$. The quasi-equilibrium current is obtained as

$$i = \frac{dq}{dt} = \frac{dq}{dE}\frac{dE}{dt}. \tag{2.59}$$

The total differential of the charge density is

$$dq = -e\left[\left(z_A \frac{\partial \Theta_A}{\partial \bar{\mu}_A} + z_B \frac{\partial \Theta_B}{\partial \bar{\mu}_A} \right) d\bar{\mu}_A + \left(z_A \frac{\partial \Theta_A}{\partial \bar{\mu}_B} + z_B \frac{\partial \Theta_B}{\partial \bar{\mu}_B} \right) d\bar{\mu}_B \right], \quad (2.60)$$

which can be simplified with the Maxell relation, $\frac{\partial \Theta_A}{\partial \bar{\mu}_B} = \frac{\partial \Theta_B}{\partial \bar{\mu}_A}$. For any particular electrochemical experiment, $d\bar{\mu}_X = -z_X F dE$. Substituting this into Eq. 2.60 and that result into Eq. 2.59, the quasi-equilibrium current becomes

$$i = -eF\left[z_A^2 \frac{\partial \Theta_A}{\partial \bar{\mu}_A} + 2z_A z_B \frac{\partial \Theta_B}{\partial \bar{\mu}_A} + z_B^2 \frac{\partial \Theta_B}{\partial \bar{\mu}_B} \right] \frac{dE}{dt}. \tag{2.61}$$

Therefore $i-E$ function can be estimated from the equilibrium partition using standard statistical-mechanics arguments, as described in the next section. All quantities which are given here such as coverages, charges, and currents are per adsorption site. They can be converted to experimentally measured units of inverse surface area through division by the area per adsorption site.

2.4.2 Monte Carlo simulation of equilibrium configurations

The properties of a system such as density coverages and response functions which we discussed in the previous section are approximated by a summation using only characteristic subset of phase space points $\{c_1, c_2, ..., c_M\}$ which are used as a statistical sample. In the statistical mechanics in the limit of $M \to \infty$ the Sum 2.62 tends to the partition function, Z

$$Z = \sum_{\{c\}} \exp \left[-\frac{H(c)}{k_B T} \right] \qquad (2.62)$$

One task of statistical mechanics is to compute from the model Hamiltonian, H, the expectation value of an observable, Y. At equilibrium this is the weighted by Boltzmann factor sum:

$$\langle Y \rangle = \frac{1}{Z} \sum_{\{c\}} Y(c) \exp \left[-\frac{H(c)}{k_B T} \right]. \qquad (2.63)$$

Analytically, for a real system, Eq. 2.62 or 2.63 is hard to calculate, or even to estimate. In contrast, MC simulation methods can be employed to estimate the properties of even quite complicated models numerically [19].

One possible route toward estimating Eq. 2.63 is to evaluate the sum directly from randomly generated configurations. This technique is known as *sample sampling*. It is found to be inefficient for most problems where the temperature is important, because only the most energetically favorable configurations make significant contribution to the sum. A homogeneous sampling of the phase space would require a tremendous effort.

A much more efficient method, called *importance sampling*, samples more frequently the phase space from certain regions from where the contributions to the observable come entirely. A priori we do not know where these regions are. Metropolis et al. [20, 21] advanced this idea not to choose the states, independently of each other, but to construct a Markov process by which states are generated where important contribution to the observable

is made. Markov chain is constructed of different configurations $c_1, c_2, ..., c_M$ in such a way that the configuration c_{i+1} depend only on the preceding one c_i. The probability of getting to c_{i+1} from c_i during a certain period of time is given by a suitable transition probability $W(c_i \rightarrow c_{i+1})$. They pointed out that it is possible to choose the transition probability $W(c_i \rightarrow c_{i+1})$ in such a way that in the limit $M \rightarrow \infty$ the distribution function $P(c)$ of the states generated by this Markov process tends towards the equilibrium distribution function

$$P_{eq}(c) = \frac{1}{Z} \exp\left[-\frac{H(c)}{k_B T}\right]. \tag{2.64}$$

In addition, the principle of detailed balance is imposed which states that the rate of going from configuration c_i to configuration c_{i+1} in equilibrium is the same as the rate of going in the opposite direction

$$P_{eq}(c_i)W(c_i \rightarrow c_{i+1}) = P_{eq}(c_{i+1})W(c_{i+1} \rightarrow c_i). \tag{2.65}$$

Eq. 2.65 implies that the ratio of transition probabilities for a move $c_i \rightarrow c_{i+1}$ and the inverse move $c_{i+1} \rightarrow c_i$ depend only on the energy change $H(c_{i+1}) - H(c_i)$

$$\frac{W(c_i \rightarrow c_{i+1})}{W(c_{i+1} \rightarrow c_i)} = \exp\left[-\frac{H(c_{i+1}) - H(c_i)}{k_B T}\right]. \tag{2.66}$$

The algorithm developed by Metropolis specifies the transition probability as

$$\begin{aligned} W(c_i \rightarrow c_{i+1}) &= \exp\left(-\frac{H(c_{i+1}) - H(c_i)}{k_B T}\right) \quad if \quad (H(c_{i+1}) - H(c_i)) > 0 \\ W(c_i \rightarrow c_{i+1}) &= 1 \qquad\qquad\qquad\qquad\quad if \quad otherwise \end{aligned} \tag{2.67}$$

In this way we select more frequently only those configurations which lead towards lowering the energy of the system. The MC sampling of the lattice-gas model includes first specification of the type and size of the lattice and the boundary conditions which have to be used. Second, we have to specify the initial configuration, e.g., all sites are no occupied. Then one repeats again and again the following steps:

1. Select one lattice site i which is considered for occupying

2. Compute the energy change associated with that move $(H(c_{i+1}) - H(c_i))$

3. Calculate the transition probability for that move $W(c_i \rightarrow c_{i+1})$ with Eq. 2.67

4. Draw a random number R uniformly distributed between 0 and 1

5. If R$<W(c_i \rightarrow c_{i+1})$ change the occupation status of that site. In any case the configuration obtained at the end of this step is considered as a "new one"

6. Analyze the resulting configuration as desired, store its properties to calculate necessary averages.

When importance sampling is used to incorporate the weighting, many thermodynamic averages can be estimated from the moments of the sample quantities. For instance, the qth moment of the number of adsorbed particles of species X is

$$M_q^X = s^{-1} \sum_{k=1}^{S} \left(\sum_{l=1}^{N} c_i^X \right)_l^q, \qquad (2.68)$$

where, s, is the number of samples taken during the simualation. The coverage is then just

$$\Theta_X = \frac{1}{N} \frac{\partial \ln Z}{\partial(\bar{\mu}_X/k_B T)} = \frac{M_1^X}{N}, \qquad (2.69)$$

with N the number of adsorption sites. The response functions, $\partial \Theta_X / \partial \bar{\mu}_X$, which are related to the quasi-equilibrium $i - E$ (CV current) are

$$\frac{\partial \Theta_X}{\partial \bar{\mu}_X} = \frac{1}{k_B T} \frac{\partial^2 \ln Z}{\partial(\bar{\mu}_X/k_B T)^2} = \frac{s}{s-1} \frac{M_2^X - (M_1^X)^2}{N k_B T}. \qquad (2.70)$$

The response function is proportional to the variance of the number of adsorbed X particles which corresponds to the fluctuations in the coverage. Eq. 2.70 is an example of class of important results in statistical mechanics, called fluctuation dissipation theorems. In our practical context it provides a convenient way to calculate the CV characteristics without numerical differentiation [22].

Chapter 3

Experimental setup

3.1   Sample preparation

Investigating two-dimensional(2D) phase transitions at electrified liquid/solid
interfaces on the nanometer scale as described in this work requires a utiliza-
tion of very clean surfaces of samples with well defined crystal orientations.
For this reason, the sample preparation and the surface cleaning procedures
were important prerequisites for successful experiments.

In this work, three kinds of substrates were used: highly oriented pyrolitic
graphite (HOPG) of rectangular shape (12 mm x 12 mm, ZYH grade from
Advance Ceramics Corporation, USA), epitaxially grown gold in (111) ori-
entation (200 - 300 nm thickness) on quartz substrates (Berliner glass KG,
Germany) and a mechanically polished single-crystal Au(111), with a size of
10 x 10 mm and a thickness of 2 mm, with an orientation misfit of better
than 0.1° and grain size less than 30 nm (MaTeck, Germany).

HOPG substrates consist of many monoatomic layers of hexagonal oriented
carbon network, which are bound by weak van der Waals interactions. This
allows us to obtain a clean and freshly prepared surface by cleaving the sub-
strate layer by layer each time prior to STM experiment.

The epitaxially grown Au(111) on quartz plates were thoroughly rinsed with
a spectroscopy grade Ethanol (Fluka) and then flame annealed on a clean
Ceran plate in a hydrogen burner at 600 - 650 °C to a reddish color for 2

min. During annealing special care was taken to distribute the heat homogeneously all over the gold surface and not to overheat the sample which results in large number of small monoatomic terraces. After this, the substrate was quenched in Milli-Q water. To prevent unwanted contamination from the surroundings on the surface of the substrate a droplet of Milli-Q water was kept on before the assembly of the electrochemical STM cell.

The experiments, in which a single crystal Au(111) was used, we employed the following cleaning procedure: first, the crystal was electropolished in 0.1 M H_2SO_4 electrolyte in a conventional electrochemical cell with platinum as a reference and a counter electrode at a constant applied voltage of $+4$ V for 1 min. As a result, the oxide layer was dissolved in 1M HCl. Then the crystal was thoroughly rinsed with Milli-Q water. In order to get large monoatomic flat terraces the single crystal Au(111) was flame annealed in the hydrogen burner to a reddish color for 10 min. Afterwards it was quenched in Milli-Q water and as described before a droplet of Milli-Q water was left on the gold surface to prevent adsorption of impurities.

These procedures resulted in large atomically flat and clean terraces.

3.2   STM measurements

In this section the experimental details related to STM experiments are described. STM measurements were performed under different conditions: in ultra high vacuum(UHV) conditions with an Omicron Multiprobe P surface science system, at the liquid/solid, and at the electrified electrolyte/solid interfaces.
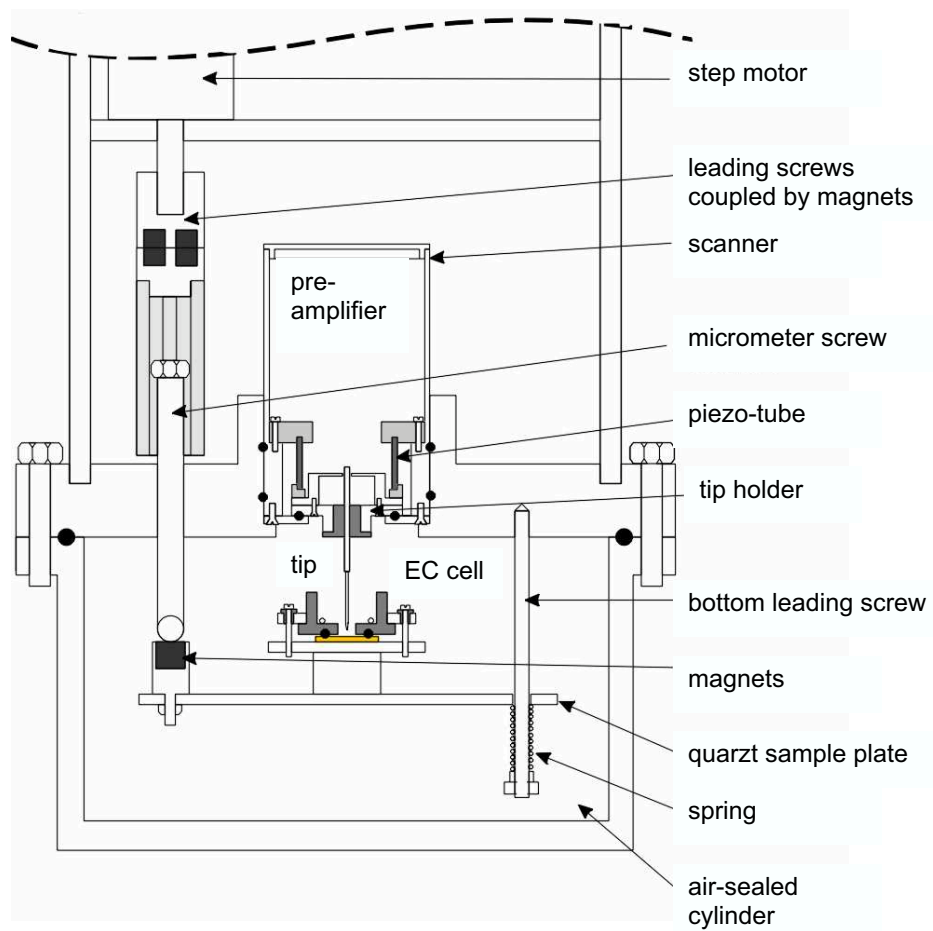
3.2.1   The STM microscope

In-situ STM investigations at liquid/solid interface were carried out with a home-built STM head employed with a 2μ scanner. The STM head was driven either by a Molecular Imaging(MI) Pico SPM controller or by a Park(Park) Scientific Instruments controller. The electrochemical in-situ STM experiments described in Chapter 5 and Chapter 6 were conducted at
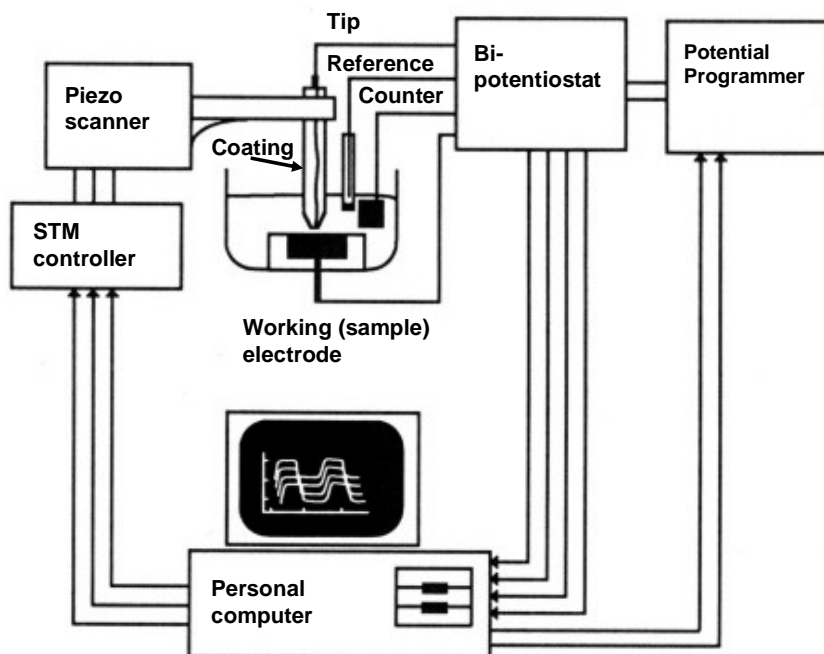
Figure 3.1: Principle of operation of electrochemical STM (EC-STM) [2].

electrified electrolyte/solid interface where the applied voltage to the sample had to be controlled independently from the bias voltage required for tunneling [23, 24]. Therefore, the STM microscope was combined with a bipotentiostat as shown schematically in Figure 3.1.

 This experimental setup is known as in-situ electrochemical STM(EC-STM) which allows us to follow changes of the structure at the electrolyte/sample interface as a function of the applied by the bipotentiostat working(sample) potential and make the electrochemical measurements as well as the imaging process possible at the same time in real time and real space. Of course, to measure tunneling currents of the order of nA one has to reduce the faradaic offset current as much as possible which is proportional to the surface area of the tip exposed in the electrolyte and the applied tip voltage. For this reason the tip must be well insulated. These details are given in Sec. 3.2.2. The home-built STM microscope is made of three parts: **(1) microscope head**, **(2) scanner** and **(3) electrochemical cell (EC-cell)**. The whole set-up is shown in Figure 3.2. The microscope head contains three stepping

Figure 3.2: Construction of the home-built EC-STM microscope [25].

motors (Vexta PK243M - 03A, Oriental Motors). The turning moment of the stepping motor is transferred through a leading screw which has a hollow inside coupled by eight magnets to a micrometer screw (New Focus Inc, 300 μm/per full rotation, USA). A sample plate made of quartz is attached by magnets to the micrometer screws. So, the turning motion results in lifting and approaching the sample towards the tip of the scanner, see Figure 3.2. Quartz is used since it has a low thermal expansion coefficient and thus reduces the thermal drift during STM imaging.

STM scanner is the "heart" of every STM microscope. It is used to control the tip position and movement with the precision needed at atomic scale. A lead titanate-lead zirconate ceramic is found to be the best piezo-electric material for scanners because of its small hysteresis and proportional displacement with the applied voltage [26]. In this study, a home-built scanner with a single piezo-tube is used having dimensions of 19 mm outside diameter and 8 mm height (PI Ceramic, Germany). The piezo tube is covered outside and inside with a thin metal layer, which acts as electrode. The outer electrode is divided into four equal sectors isolated from each other. An elongation in x,y direction is generated by applying an appropriate voltage to two opposite sectors. A motion in z-direction (along the longitudinal axis) can be achieved with the inner electrode which is driven by the feedback system. The scanner is also equipped with a current preamplifier which converts tunneling current into voltage. An important point is the calibration of piezo scanners. To do this for the x,y-in-plane directions, we have chosen the simplest method by measuring a well known spacing of a substrate such as HOPG. For the z-direction a monoatomic gold step was used. The method is describe in detail in ref. [27].

The schematic construction of the electrochemical(EC) cell used for in-situ EC-STM experiments is shown in Figure 3.3. The EC cell is made of Teflon, which is sealed through a Teflon-coated silicon O-ring.
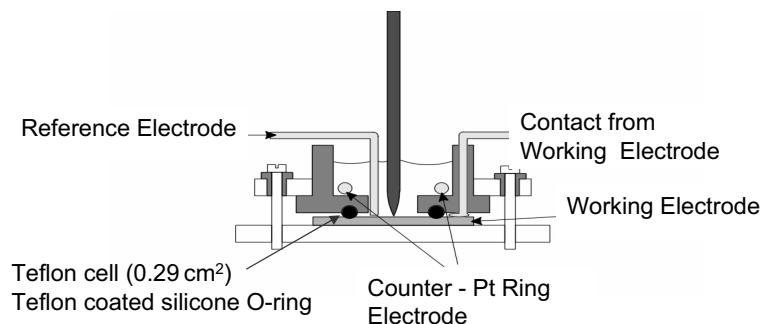
Figure 3.3: Schematic diagram of the electrochemical cell (EC-cell).

3.2.2   Tip preparation

The quality of STM images depends strongly on the quality of tunneling tips. Therefore, the reproducible preparation of well shaped and stable tips is crucial. Two kinds of STM tips were used in this work, made of PtIr wire (90%-10% respectively, 0.25 mm in diameter, Advent, England) and from W wire (>99.98, 0.25 mm diameter, Alfa). The tips were produced from the coresponding wires by cutting or by electrochemical etching. Some of the STM experiments done in non-conducting media were carried out with PtIr tips which simply had been cut at 45° with clean scissors. Incidentally, this procedure gave very sharp tips, good enough for atomic resolution, but in most of the cases this yielded multiple tunneling from multiple nano tips resulting in so called double tip effects or ghost images. A typical exapmle of double tip effect caused by a cut tip is given in Figure 3.4.

PtIr tips were also produced by electrochemical etching in 4 M NaCN using the "drop-off" method [28,29]. A PtIr wire, after being washed with ethanol, was vertically anchored to a manipulator and fixed in the center of a ring wire of Pt acting as a counter electrode. A thin lamella of NaCN solution was formed on the ring electrode crossing the PtIr wire. Then an AC voltage of 4 V was applied between the Pt ring electrode and PtIr wire. Due to the "necking-in" effect, the down part of the wire drops off when its weight exceeds the tensile strength of the necking-in region. Just before droping the voltage was reduced to 2 V. The down part was caught in a small plastic tip holder so that the apex of the tip was not damaged. For a better control
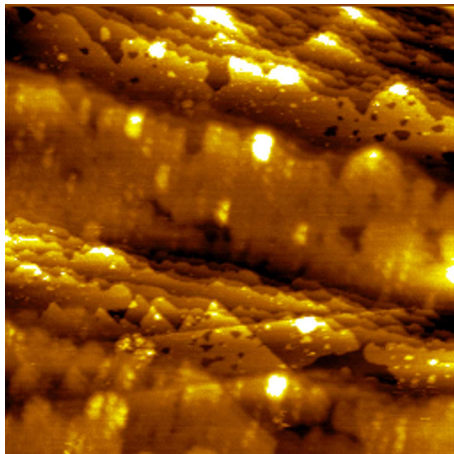
Figure 3.4: 350 nm x 350 nm STM image on Au(111) showing a ghost step edge artifact caused by a double tip.

all tips were checked by an optical microscope with 40x magnification before use. Similar procedure was employed for the preparation of W tips but in 2 M NaOH applying a DC voltage of 4 V in which the W wire was the anode and the Pr ring electrode cathode.

In order to minimize Faradaic currents in those STM measurements carried out in an electrolyte the freshly prepared tips were insulated with an anodic epoxy-paint (BASF, ZQ 84-3225 0201,Germany). For this purpose 0.8 cm of PtIr tips were immersed into the epoxy-paint and a DC voltage of 25 V was applied for 5 minutes between the tip(anode) and a counter Pt plate electrode(cathode). For W tips a different DC voltage of 80 V was used for 5 minutes. To harden the coating, the tips were immediately put into an oven for 2h at 150 °C and then 10 min. at 250 °C with the tip apex pointing up.

3.3 Electrochemical measurements

All electrochemical measurements were conducted in the conventional three-electrode electrochemical cell, see Figure 3.3 and the electrochemical response of the studied systems was recorded with the help of an AutoLab potentiostat (PGSTAT 30, Eco Chemie). For in-situ EC-STM experiments the required potential was applied by a Molecular Imaging PicoStat potentiostat.

3.3.1   Electrolytes

In the framework of this work two kinds of electrolytes were used: silver
plating solutions contained 1mM Ag_2SO_4 (p.a., Merck, Germany) with a sup-
porting electrolyte of 0.1M H_2SO_4 (Suprapur, Merck, Germany) prepared in
Milli-Q water (18.2 MΩ, Millipore) and 2 mM AgCl (p.a., Fluka) in 58:42
mole ratio $AlCl_3$:1-butyl-3-methyl-imidazolim chloride (BMICl). The aque-
ous electrolyte was purged with nitrogen (5N, Griesheim, Germany) before
each experiment.

The synthesis of 1-bythyl-3-methyl-imidazolium chloride was performed in
a closed glass container inside a simple glove box, without circulation and
filter systems, filled with argon. Initial products for the synthesis of BMICl
were 1-methylimidazole (99 %, Merck, Germany) and 1-chlorobutane (95 %,
Merck, Germany). For cleaning proposes 1-chlorobutane was boiled first for
several hours over P_2O_5, distilled at 78 °C, then placed in a tightly sealed
flask and transported into the glove box. 1-methylimidazole was distilled
under vacuum at 198 °C and after that left under the atmosphere of Ar in a
protective glass container.

To synthesize BMICl, 1-methylimidazole was slowly added to 1-chlorobutane
under argon. This mixture was stirred at 50 °C under the same atmosphere
for two weeks. During that time the mixture formed an oily product, whose
subsequent recrystallization was initiated by addition of several small pieces
of BMICl. The whole crystallization of BMICl took approximately one hour
and transparent crystals were the final product. These crystals were filtered
out and recrystalized two times from acetonitrile (99.8 %, Merck, Germany).
The resulting white crystals of BMICl were dried under vacuum for 14 days
and only after that used for the further preparation of the room tempera-
ture molten salt. Aluminium cholide (p.a., Fluka, Germany) was cleaned by
recrystalization and sublimation at 200 °C three times under vacuum in a
quartz ampoule.

The ionic electrolyte was produced by slowly mixing $AlCl_3$ and BMICl in pro-
portional composition of 58:42. Immediately after the addition of the first
several crystals of the aluminum chloride to the BMICl the mixture began

to melt. This melting was a result of a spontaneous exothermal reaction. Therefore mixing had to be done slowly to avoid local overheating, which could lead to a decomposition of the whole melt in general and the organic component in particular. During 2-3 hours $AlCl_3$ and BMICl were mixed up and then left under stirring over 14 - 16 hours. Then aluminum chloride was completely dissolved and the ionic liquid was ready for the dissolution of AgCl.
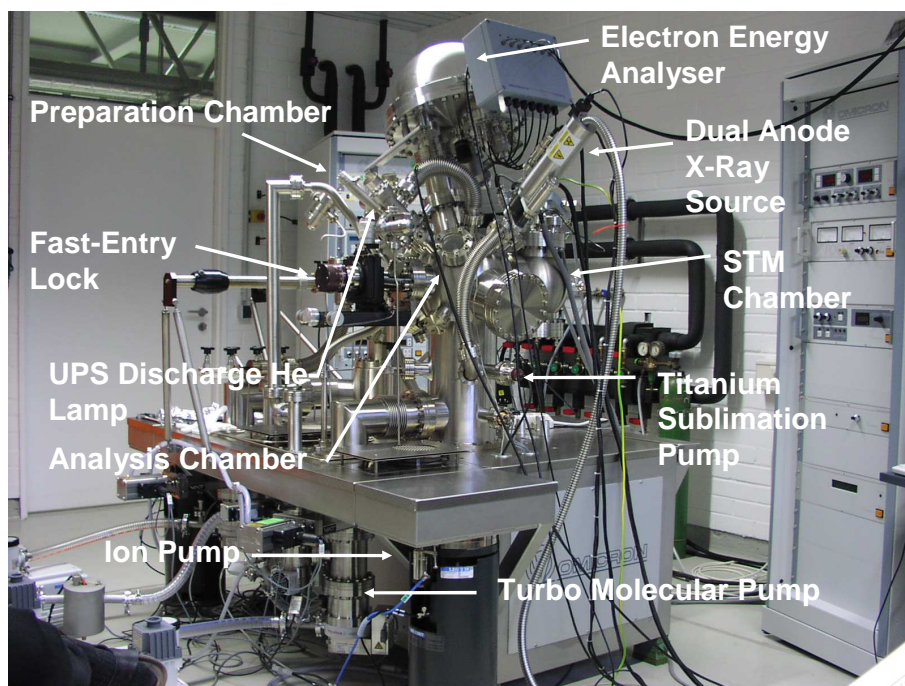
Figure 3.5: The Omicron multi-technique surface science UHV system.

3.4 XPS and UPS measurements

XPS and UPS measurements were carried out in an Omicron (NanoTechnology) Multiprobe P surface science ultra high vacuum (UHV) system which is shown in Figure 3.5. The UHV system contains three satellite chambers: preparation, analysis and SPM chamber. The base pressure in the analysis

chamber was lower than 10^{-9} Pa. Two turbo-molecular pumps, one ion-pump(IP), and a titanium sublimation pump(TSP) were used to maintain the the vacuum in that regime. For XPS measurements the analysis chamber is equipped with a multi-channel energy analyzer, EA 125 U7, and a twin anode (Mg Kα-hv = 1253.6 eV; Al Kα-hv = 1486.6 eV) DAR 400 X-ray source. XPS spectra were taken with the Mg Kα anode operated at 255 W at constant pass-energy of the analyzer of 50 eV in steps of 0.2 eV. Ultra violet photoelectron spectroscopic (UPS) studies of self-assembled monolayers on Au(111) were measured by a cold cathode UV source - HIS 13 supplied form the Omicron system using He(I) light (21.22 eV). Typical values for the pass energy and the entrance slits were chosen as 3.0 eV and 0.5 mm, respectively. The photoelectron spectra were recorded under a total resolution of 0.05 eV as determined from Fermi edge measurements of bare gold samples.

Chapter 4

2D Self-assembly of macrocycles

4.1 Introduction

The realization of nanoscale molecular assembling requires the development of new and efficient approaches for combining molecular building blocks into desired functional structures. Self-assembly [30, 31] of individual molecules on surfaces provides an attractive route to pattern nanostructures by bottom-up approach and will likely supersede lithographic techniques in manufacturing miniature devices in electronics and optics. Self-assembly, in general, is defined as the spontaneous organization of pre-design building blocks(molecules) to matter with geometric translational symmetry, typically involving multiple energy scales and multiple degrees of freedom. Self-assembly is also abundant in nature, as seen in the formation of, e.g., membranes from lipid molecules, or the living cell as probably the most important paradigm. Before these assembles of pre-design building blocks, atoms or molecules can be engineered into practical devices with advanced functionality, a number of fundamental questions must be addressed, such as: What is the nature and driving force of self-assembly? Which type of interactions (adsorbate-adsorbate or adsorbate-substrate) are crucial for the order? In which way do the different constituents of the molecular building blocks have an impact on the structure? How should individual atoms and molecular building blocks be manipulated and positioned at specific sites on

a surface?

The invention of Scanning Tunneling Microscopy(STM) has enabled researchers to shed some light on these questions. In particular, STM and atomic force microscopy(AFM), with their molecular and even atomic resolution are becoming important and well suited tools for elucidation of self-assembled structures. Therefore, the discovery of self-assembled monolayers(SAMs) was made possible by the invention of STM.

Some of the earliest STM studies of self-assembly at the liquid/solid interface were done with substituted long-chain alkane and alcohol monolayers physisorbed on graphite [32,33,34,35,36,37,38,39,40,41,42]. High-resolution STM images of well-ordered monolayers of these systems were easily obtained. Differences in packing of molecules were found which led to an interesting discussion about the impact of adsorbate-adsorbate or adsorbate-substrate interactions on monolayer ordering.

Another class of compounds which are very good candidates for SAMs formation are sulphur-containing alkanes [43]. In fact, one of the first studies reveling the phenomenon of self-assembly was based on disulfides on gold surfaces [44]. Investigations of thiols assembled from pheniloctane solutions on graphite have shown that the molecules lie flat on the substrate and are weakly physisorbed. Contrary to all expectations, thiols with similar length chemisorbed on metal surfaces, such as Au, Ag stick out almost perpendicular to the substrate surface [45, 46, 47]. Interestingly, a brighter contrast for functional groups of different thiols, sulfides and disulfides adsorbed on graphite in the STM images led to the idea that tunneling probability in the area of S-H or S-S is greatly enhanced [32, 48, 49, 50, 51, 52, 53]. Several STM studies have manifested that the bright spots in the high-resolution images are related to the position of the S atom along the hydrocarbon chain. Furthermore, two types of molecular arrangements are found: head-to-head and head-to-tail. In the first configuration, the SH group of one molecule is adjacent to the SH group of the neighboring molecule. In the second one, the SH group lies next to the neighboring methyl group. SAMs of 1-docosanethiol [32,49,50] have been observed in both configurations randomly distributed in the monolayer, whereas more ordered lamellae have been re-

ported for 1-dodecanethiol.

Similar to the thiols, the position of the sulphur atom is clearly visible in SAMs of sulfides such as docosane disulfide, hexadecyl disulfide, tetradecyl sulfide and octadecyl sulfide physisorbed on graphite and on MoS_2 [32, 48, 49, 50, 51, 54]. However, differences have been found between the assemblies of sulfides and disulfides on the MoS_2 and graphite substrates. The contrast of sulphur atoms with respect to the hydrocarbon chain appears to diminish suggesting changes in electronic coupling between the adsorbate and substrate. In case of docosane disulfide, a different 2D geometry has been observed compared with than one on graphite. Moreover, a drastic change is manifested in STM images of hexadecyl ether in which the sulphur atom is substituted by an oxygen atom [48]. In sharp contrast to the bright spots seen at the locations of sulphur atoms, the positions of oxygen atoms are very dark relative to the carbon backbone. It is thought that the unusual intensity of the sulphur group is observed due to an enhanced tunneling which is caused by the overlapping of an electronic state of the adsorbate in the conduction band with the substrate Fermi level.

A promising class of compounds to form macromolecular assembles are ring systems. Porphyrins such as iron and zinc protoporphyrin(IX) chlorides [55, 56] deposited on graphite from aqueous solutions and copper tetra[3,5 di-t-butylphenyl]porphyrin (Cu-TBPP) adsorbed on Cu(100), Au(110), and Ag(110) surfaces [57, 58] have been investigated by STM. Cyanophenyl substituted porphyrins have been studied by STM at the vacuum-solid interface concerning the characteristic intermolecular interactions of the specific side groups [59]. Self-assembly of other ring compounds such as pyrroles [60], thiophenes [61] and triphenylenes [62] as well as copper and cobalt [63, 64] phthalocyanines [65] on Au(111) has been investigated by STM.

In the light of this short overview, studies of self-assembly of macrocyclic compounds are rare. However, their aggregation and self-organisation phenomena have received a lot of attention recently, see reviews [66, 67, 68]. Starting with the pioneering work of Chandrasekhar et al. [69, 70], disklike ring molecules with a rigid internal void known as shape-persistent macromolecules were investigated as building blocks in supramolecular chemistry. Therefore,

one anticipates that rigid disk-like columnar phases should produce materials with well-defined and non-collapsible internal channels. Furthermore, functionalizing these hollow structures appropriately could potentially result in applications such as ion channels, micro reaction chambers or functinalized rodlike micellar aggregates.

Macrocycles based on phenyl-ethynyl or phenyl-butadienyl units have been shown to form assembled structures due to weaker $\Pi - \Pi$ interactions [71, 72, 73, 74]. Also, it has been concluded that self-assembly is possible only if macrocycles have electron-deficient cores [75]. Thus, a primary motivation of this work is to investigate by STM the formation of ordered structures of these molecules.

4.2   Results

In this chapter, the STM experimental results related to self-assembly of shape-persistent macrocycles are described.

4.2.1   SAMs of shape-persistent macrocycles on HOPG

Shape-persistent macrocycles such as **1**, see Figure 4.1, are a promising class of candidates to form supramolecular assemblies on surfaces. They have relatively large, ring-shaped cores with flexible side alkyl chains. The triple bond inside the ring is quite inflexible and tends to keep the molecule planar. Hence, they are known as shape-persistent macrocycles. In addition to most other molecules able to form SAMs, macrocycles like **1** offer the possibility to incorporate functional groups in their interior while keeping the molecular dimensions and thus the pattern periodicity unaffected [76, 77, 78, 79]. Functionalized shape-persistent macrocycles allow therefore not only the creation of nano-patterned surfaces but the formation of functionalized nanopatterned surfaces.

1
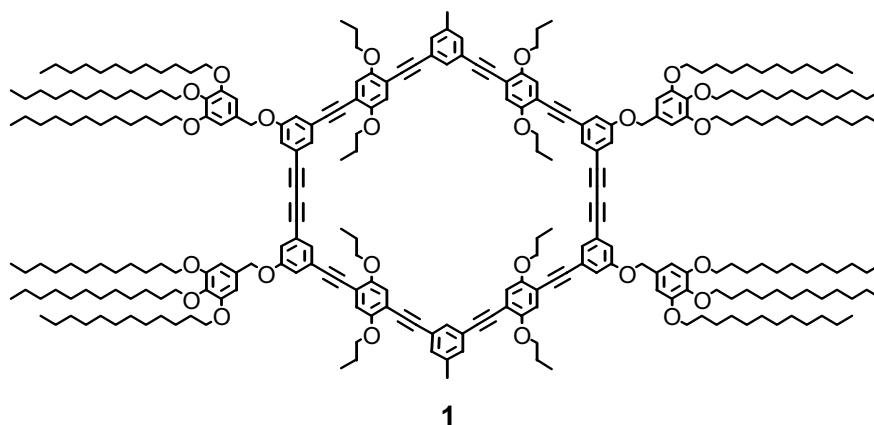
Figure 4.1: The molecular structure of shape persistent macrocycles [76].

First, the physisorption abilities of **1** were probed by STM at the liquid/solid interface. As a substrate highly oriented pyrolytic graphite(HOPG) was chosen because of its large monoatomically flat terraces, see Figure 4.2A and well known hexagonal closed packing (hcp) structure (Figure 4.2B).
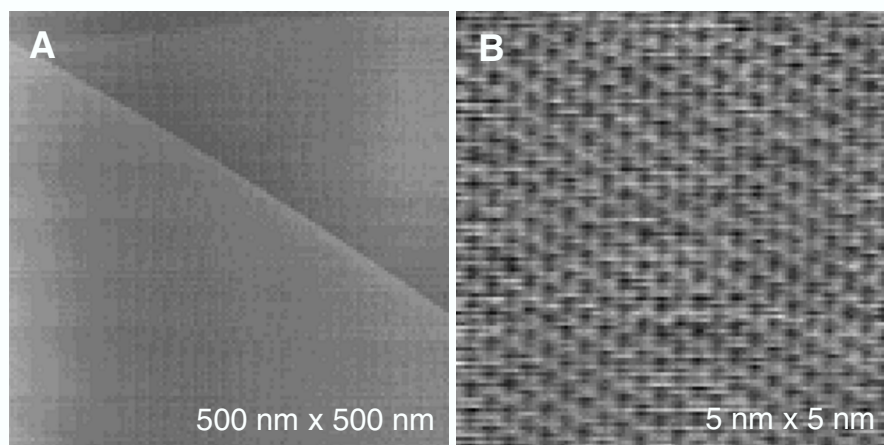
Figure 4.2: STM of HOPG showing: (A) large monoatomic flat terraces, I_t=0.5 nA, Ubias=0.5 V; (B) atomic resolution of the hexagonal graphite structure, I_t=2 nA, Ubias=0.5 V.

The first aim was to check what kind of structure macrocycle **1** can form and if it would be self-ordered on the flat large HOPG terraces. In addition it is of interest whether the macrocycles are physisorbed and lie flat on the
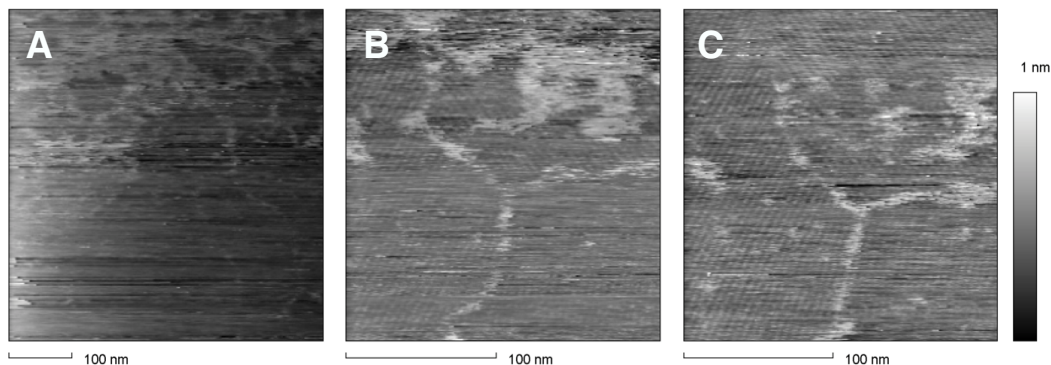
Figure 4.3: STM images of **1** on HOPG taken at different bias voltages and constant tunneling current of 1 nA. (A) V_{bias}=1 V; (B) V_{bias}=1.2 V ;(C) V_{bias}=1.4 V.

substrate. For that purpose, a freshly cleaved HOPG surface was exposed to 0.5 mM solution of **1** in 1,2,4-trichlorobenzene (99+%, Aldrich, Germany). STM images with different bias voltages (V_{bias}) were aquired at the solution-HOPG interface. Figure 4.3A shows an STM image of basal plane of the substrate at V_{bias}=1V. Some brighter areas in the upper left part of the image indicate that the tunneling probability in these zones is enchanced due to the interaction with the monolayer. The next sequential STM images, Figure 4.3B and C, reveal spontaneous physisorption of **1** as an ordered monolayer on HOPG. The self-assembly of **1** seems to be lacking of long range ordering. Domains with different orientation of **1** are clearly seen. With increasing V_{bias}, the contrast of monolayer strongly increases. As long as the applied bias voltage is kept larger than 1.4 V, the monolayer appears in the STM image. This issue will be clarified in Sec. 4.3.

Another interesting issue concerns the self-assembly of **1** on HOPG influenced by imperfections and defects in the substrate. As displayed from Figure 4.4, defects of the substrate result in reorientation of the molecular rows.

Figure 4.5 shows STM images of **1** spontaneously physisorbed as a monolayer on HOPG acquired with a tunneling current I_t=1 nA and a bias voltage V_{bias} =1.7 V. The image was taken during scanning at the solution-HOPG interface. A well ordered array of the macrocycles can be clearly seen. The
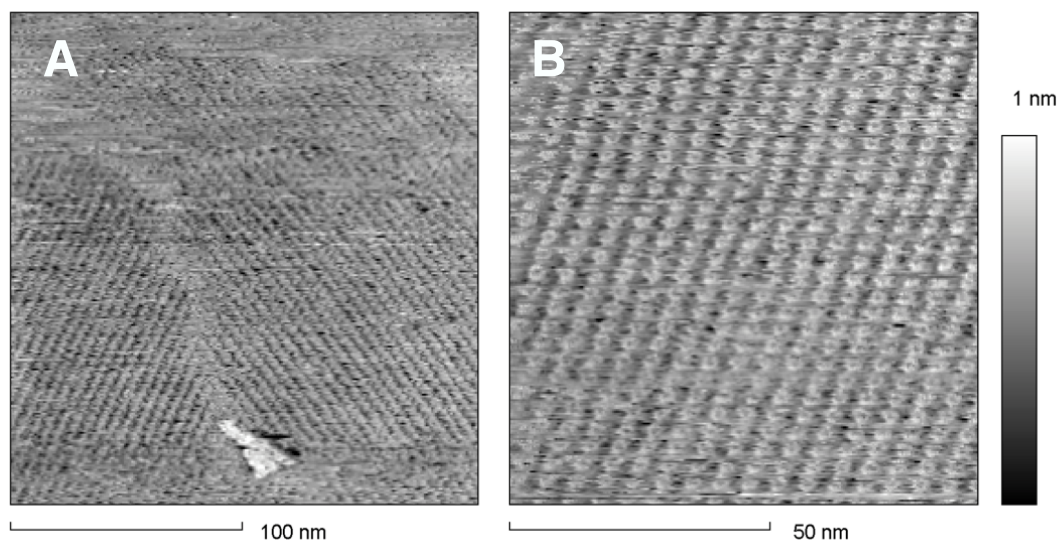
Figure 4.4: The effect of defects on the self-assembly of **1** on HOPG. (A) the orientation of molecular rows depends on defects of substrate ;(B) self-assembly is perfect; V_{bias}=1.7 V, I_t=1 nA.

two-dimensional unit cell contains one macrocycle (Z = 1) and has lattice constants of A = 3.8 $\pm$ 0.32 nm, B = 6.1 $\pm$ 0.45 nm and Γ= 75 $\pm$ 2°.
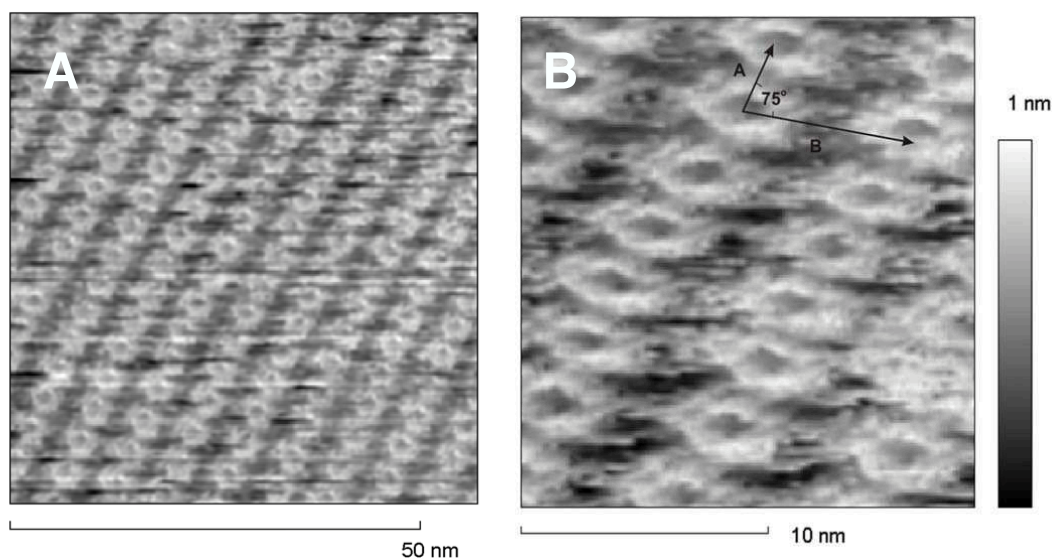
Figure 4.5: STM images of self-assembly of the shape-persistent macrocycle **1** taken at the solution - HOPG interface with lattice constants of A = 3.8 $\pm$ 0.32 nm, B = 6.1 $\pm$ 0.45 nm and Γ= 75 $\pm$ 2°; V_{bias}=1.7 V, I_t=1 nA; (A) 50 nm x 50 nm (B) 15 nm x 15 nm.

400 nm x 400 nm
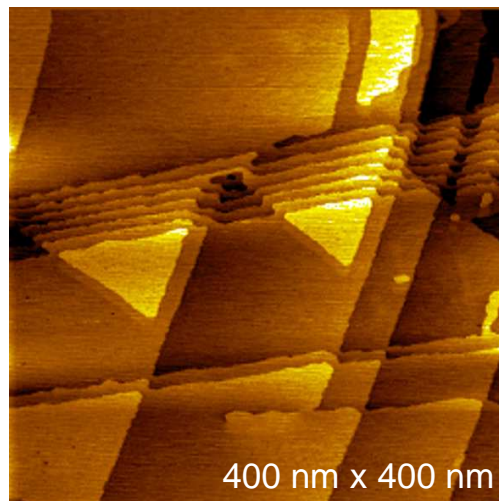
Figure 4.6: A typical single crystal bare Au(111) surface imaged by STM at V_{bias}=0.5 V, I_t=0.3 nA.

4.2.2   SAMs of shape-persistent macrocycles on Au(111)

From a technological point of view, functionalized SAMs of **1** on metal substrates have a potential for various supramolecular aspects and applications including organization into and transport through porous molecular crystals [80, 81, 82, 83, 84] and nanostructured patterning [79, 85, 86]. Therefore, we tried to form SAMs of **1** on gold substrates. Unfortunately, the attempts were not successful. This may have several reasons: for instance, the balance between the lateral intermolecular and the adsorbate-Au(111) interactions might not be optimal; lack of necessary functionalization which could bind **1** to Au(111); the roughness of the Au(111) surface. In comparison with the large flat HOPG surface, a typical Au(111) surface exhibits a number of monoatomic deep gold triangular islands which are very characteristic for the (111) plane, see Figure 4.6.

 In order to improve the binding characteristics of **1** on Au(111), the macrocycles were functionlized by adding thiolether groups to the interior of the macrocycles. It is well established that alkanethiols easily form a stable adlayer on Au(111) yielding $(\sqrt{3} \times \sqrt{3})R°30$ superstructures [87,88,89,90]. Even alkyl sulphides have been shown to produce steady self-assembled monolay-

ers on Au(111) [91]. Therefore macrocycles of **2b** were prepared by carbodi-imide coupling of **2a** and 2-(ethylmercapto)-ethylamine hydrochloride yielding the ethylmercapto-ethylamide containing compounds **2b**. These structures now contain intraannular functional groups (amides) and additional thioether groups for improved binding on the Au substrate.

2a: R = OH
2b: R = NH(CH$_2$)$_2$SEt
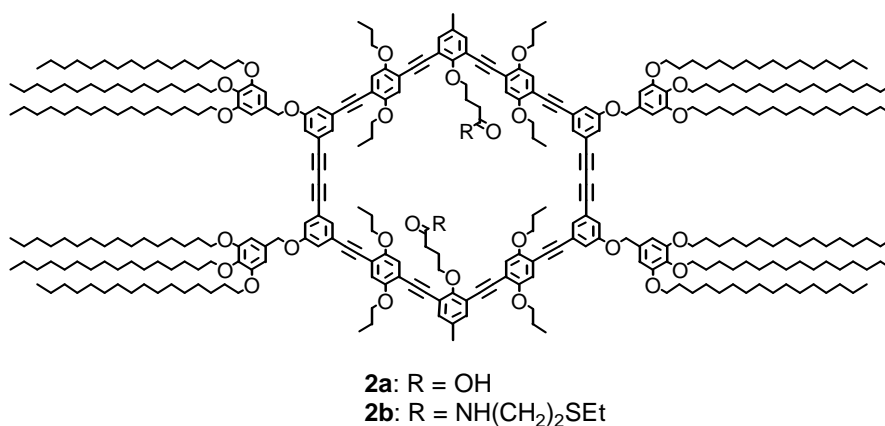
Figure 4.7: The molecular structure of sulfur functionalized macrocycle **1** [92].

A single crystal Au(111) surface was brought in contact with 0.1 mM solution of **2b** in octhylbenzene and was examined by STM. The effect of sulfur functionalization of **2b** on its adsorption properties is clearly seen. Individual macrocycles of **2b** are randomly chemisorbed all over the surface, see Figure 4.8A. The macromolecules appear as round bright spots in the STM image. A cross section analysis among them shows a size of 6.5 nm, see Figure 4.8B. The alkyl side chains are not visible.
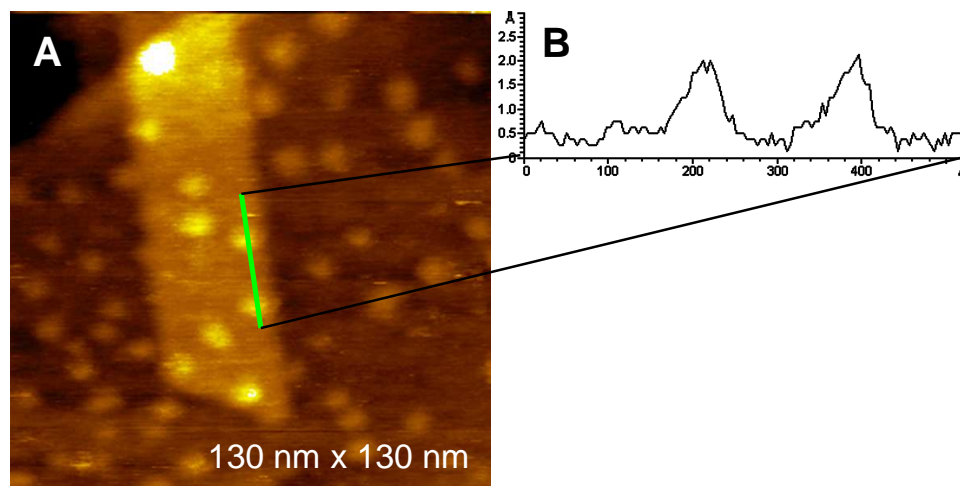
Figure 4.8: STM image of **2b** adsorbed from solution on single crystal Au(111). (A) molecules are randomly distributed all over the Au(111) surface ;(B) a cross section height profile of two macromolecules.

In order to improve the order of **2b** assemblies on Au(111), the following preparation procedure was employed. Self-assembly of **2b** was carried out on a single crystal Au(111) from a solution containing **2b** at 70 °C for 15h. Then the substrate was rinsed several times with a large amount of fresh octylbenzene to remove weakly adsorbed species and dried in a stream of nitrogen. Then the surface was examined by STM at the air/Au(111) interface.

STM images show that in this case the rows of macromolecules are well ordered, see Figure 4.9. Although the arrangement is not as perfect as in the case of the molecule **1** on HOPG a uniform average superstructure in a wide range all over the scan area is clearly visible. In order to make sure that the observed periodicity is not an imaging artifact we have rotated the scanning area by different angles. The molecules are organised into rows densely packed which is indicative of vigorous intermolecular interactions. Cross section analysis shows that the striped phase has a corrugation period of approximately 6.8 ± 0.8 nm, see Figure 4.10A,B.

A similar structure was found at the UHV/solid interface. In order to investigate how the packing of **2b** is influenced at the vacuum interface, UHV-STM experiments were carried out.
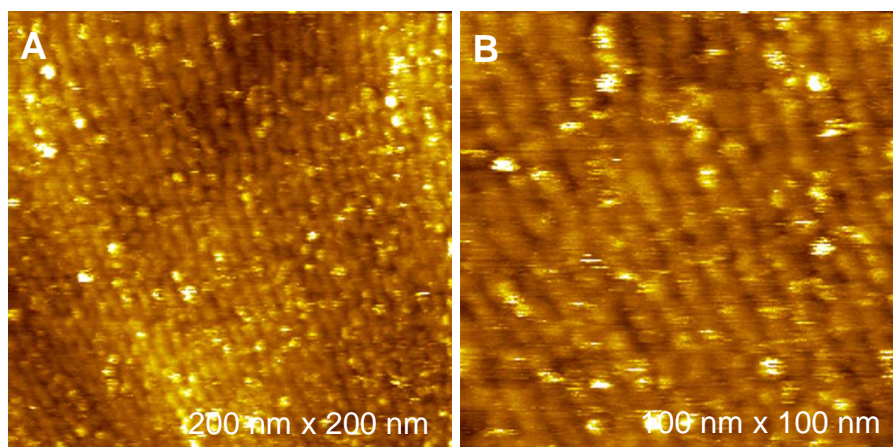
Figure 4.9: STM images of SAMs of **2b** at the air/Au(111) interface after annealing at 70 °C for 15h; V_{bias}=0.5 V, I_t=0.1 nA.
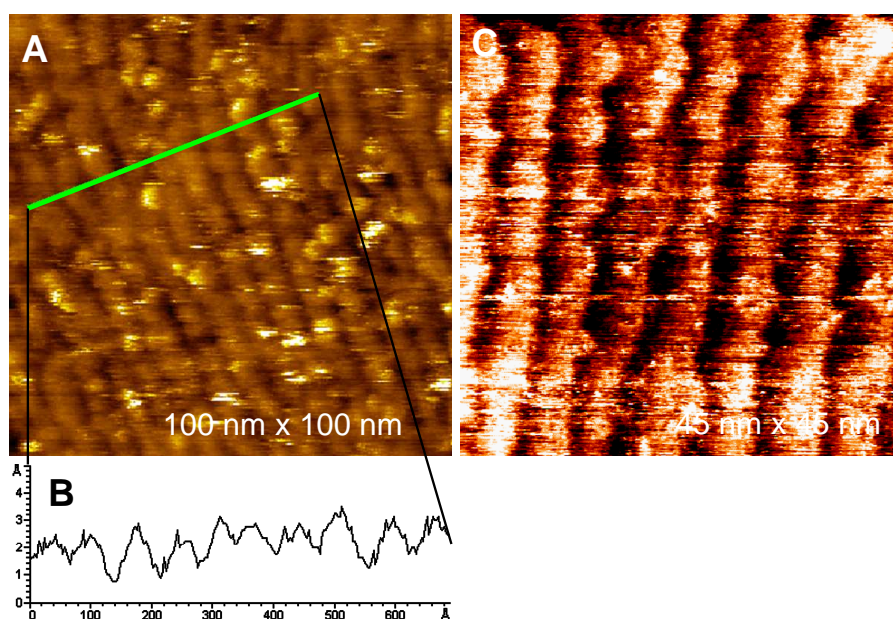
Figure 4.10: (A) STM image of SAMs of **2b** at air/Au(111) interface after annealing at 70 °C (B) Cross section analysis shows that the striped phase of **2b** at the air/solid interface has a corrugation period of approximately 6.8 ± 0.8 nm after annealing at 70 °C (C) STM image of SAMs of **2b** in UHV conditions on Au(111) after annealing at 70 °C; V_{bias}=0.8 V, I_t=0.1 nA.

Figure 4.10C displays an STM image revealing the molecular resolution

topography of SAMs of **2b** on Au(111) under UHV conditions showing that
the molecular arrangement does not change significantly. From the z-profile
measurements we conclude that the molecule **2b** is lying flat which is char-
acteristic for planar molecules with a π system parallel to the surface [93].
In the case of **2b** we could not resolve the empty space in the macrocycle
which presumably is due to the functionalization of the ring with the amides
and thiolether groups.

4.3   Discussion

In this section, specific issues concerning the tunnelling mechanism through
individual macromolecules, the binding and the effect of the functionaliza-
tion are discussed.

4.3.1   Tunneling mechanism through individual macro-molecules

So far we have shown that weakly adsorbed nonconducting macromolecules
of **1** can be imaged on HOPG. The first issue that arises is to check if the
STM images provide an accurate structural picture of the adsorbate. For
that purpose we have to compare the geometry of a model structure of **1**
with the STM image. A geometry optimization of **1** was performed by AM1
method [94] implemented in ArgusLab[1] software excluding alkyl side chains.
Due to the characteristics of the carbon bonds involved, the macromolecule
can be considered being flat and thus a planar geometry is enforced during
the relaxation. The optimized molecular structure of **1** presented in Fig-
ure 4.11 shows a relatively good correspondence between the geometry, bond
lenghts and bond angles of the ring and the structure observed with the STM

---

[1]ArgusLab 4.0.1 Mark A. Thompson
mark@arguslab.com
Planaria Software LLC, Seattle, WA
http://www.arguslab.com

image of **1**. For instance, the height of the ring calculated from the model yields 2.56 nm which is in good agreement with the value of 2.3 ± 0.3 nm obtained from STM image. The width of **1** given by the model is 3.6 nm whereas the measured value is 3.4 ± 0.4 nm. Since the side alkyl chains appear as darker contrast with respect to the ring it was difficult to measure directly their lengths.
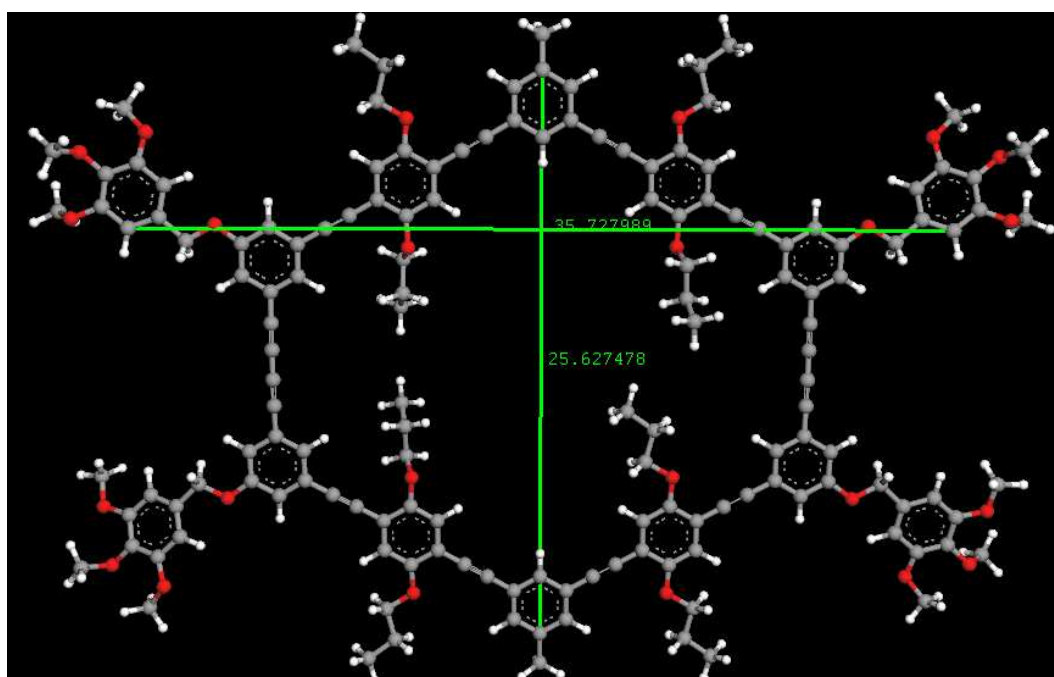
Figure 4.11: Geometry optimized molecular structure of **1** without alkyl side chains. Due to the characteristics of the carbon bonds involved, the macromolecule can be considered being flat and thus a planar geometry is enforced during the relaxation. Indicated distances are given in Å.

Another interesting issue concerns the influence of the macromolecule **1** on the STM tunneling mechanism. As it was pointed out in the results section, the contrast of molecules **1** physisorbed on HOPG is greatly increased at higher bias voltages. When a macrocycle of **1** is not adsorbed on the substrate surface its states consist of a series of occupied electronic molecular orbitals (for instance, the highest occupied energy orbital is known as HOMO state) as well as a series of unoccupied molecular orbitals (the lowest energy
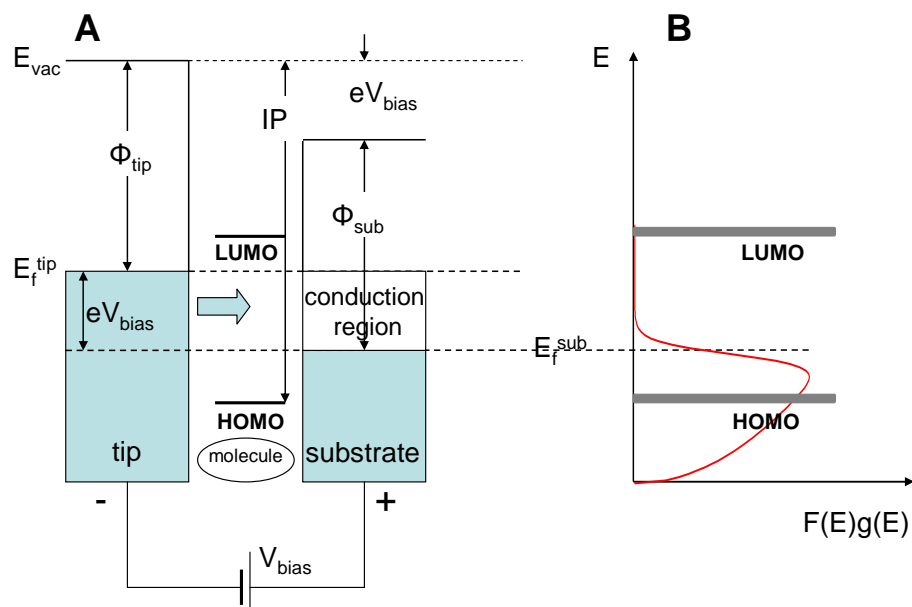
Figure 4.12: (A) Tunneling mechanism of **1** on HOPG. Blue areas correspond to occupied states. The tip is biased negatively with respect to the surface. Tunneling current flows from the occupied tip to the empty substrate states. (B) HOMO states of the macromolecule matches with the density of states of the substrate near the Fermi level.

unoccupied orbital is a LUMO state). On the other hand, for tunneling and STM, the Fermi level, E_f, plays the most important role on the solid metal surface. For details about tunneling, see Sec. 2.1.1. When a macrocycle of **1** is physisorbed on the surface, a shift occurs in the energies of both HOMO and LUMO as well as some shift in the electronic energies of the surface states of HOPG. Therefore, there is no simple way to precisely place the energies of adsorbate states with respect to the energies of the substrate surface states. An approximate approach is to align the vacuum level of the adsorbate and the vacuum level of the surface. The vacuum level of the adsorbate is above its HOMO by the ionization potential(IP), see Figure 4.12A.

Neglecting the change in the relative spacing between the adsorbate LUMO, HOMO and vacuum level upon physisorbtion this approach provides an approximate energy scale that allows the relative positions of the LUMO and HOMO levels of the substrate to be located with respect to the surface Fermi

level. Following this approach we can distinguish between two general cases. In the first case, the LUMO energy level of **1** is well separated from the Fermi level of the surface. In the second one, the LUMO is near E_f^{sub} and by increasing the bias voltage, the LUMO orbital drops into the region between E_f^{sub} and $E_f^{sub} + eV_{bias}$- "conduction region". Here we assume that the tip is biased negatively with respect to the surface in accordance with Figure 4.12A so that electrons tunnel from tip into the surface(adsorbate). In principle, LUMO orbital is more important than HOMO in the tunneling process, simple because these orbitals act as an antenna sticking farther out from the surface than the occupied levels. This is supported by the fact that the ring of **1** exhibits very diffuse structure [95, 96]. Taking into account our experimental observation that the ordered 2D array of **1** appears if V_{bias} is larger than 1.2 V, it is reasonable to assume that the LUMO level falls into the "conduction region". In addition, the density of states on the substrate might be overlapped with the HOMO states of the macromolecule, see Figure 4.12B, and thus influence the tunneling probability. Only under these circumstances the macrocycle can be projected on the HOPG surface.

The tunneling mechanism of macrocycle **2b** on Au(111) looks different. In case of **1** on HOPG, macromolecules lie flat on the surface and Π orbital electrons couple more strongly to the surface of HOPG, where the electronic structure is also dominated by Π orbitals. This is the reason why double and triple bonds of **1** are displayed in the STM images with a markedly increased contrast. On contrary, **2b** is binded on Au(111) due to thiol ether functionalization and can be consider as an "extention" of the surface. So, their internal void appear like bright filled rings in the STM images. As we have mentioned in Sec. 4.1, sulphur containing functional groups also exhibit enhanced tunneling probability.

Concerning the ordering of macromolecules **1** and **2b**, the main difference between SAMs formed on Au and those formed on HOPG is the driving force for self-assembly. For instance, SAM formation on Au arises from the chemical reaction between sulphur functionalities and the Au surface, after which 2D ordering occurs followed by lateral interaction between side alkyl chains. Molecular arrangements on HOPG are mainly encouraged by a com-

bination of weak van der Waals interactions between molecules and between molecules and substrate.

4.3.2   Binding characteristics of macromolecules on HOPG and Au(111)

At room temperature, the adsorbates are chemisorbed and their mobility on the surface is largely fixed by the strong sulfide-gold interaction, and kinetically disordered phase is observed. At elevated temperatures, however, the sulfide-Au interaction can be reversibly broken, and reorganisation of the monolayer to an energetically more favorable structure with all alkyl side chains oriented can occur. Therefore, by annealing the substrate during formation of SAMs one can improve the ordering and structure of **2b** on Au(111) as evidenced by STM. To prove that annealing at 70 °C leads to denser monolayers than those prepared at room temperatures, an inability of SAMs to block the heterogeneous electron transfer between $Fe(CN)_6^{-3}$ and gold electrode was studied. Fe^{3+}/Fe^{2+} is a typical reversible redox reaction controlled by diffusion. For details about the electrochemistry of diffusion controlled reactions, see Sec. 2.3.2. The result unambiguously shows that SAMs of **2b** hinder the electron transfer at the interface of Au(111) electrode/electrolyte 1mM $K_3Fe(CN)_6^{-3}$ in 0.1 M K_2SO_4 better when they are prepared at 70 °C, see Figure 4.13.

Templated electrodeposition of metals, such as Cu and Ag through SAMs of **2b** on Au(111) were performed. Although chemisorption of **2b** via thiolether functionalization on Au(111) is relatively strong, SAMs are completely swept away from the electrodeposited metal adlayer on the surface. It became evident that metal-Au(111) bond is stronger that SAMs-Au(111) bond and SAMs of **2b** are easily removed.

To understand the binding of **2b** on the Au(111) substrate, XPS and UPS measurements were carried out after UHV-STM characterization. As expected, the C 1s, Au 4d and O 1s core level peaks are clearly resolved, see Figure 4.14A. The C 1s peak seems to be shifted to higher binding energies
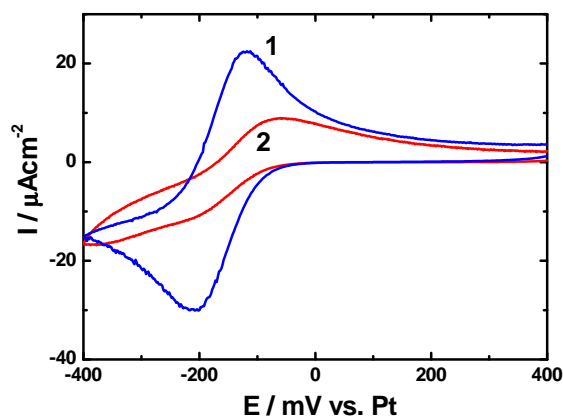
Figure 4.13: Monolayers of **2b** block the reversible electron transfer reaction of Fe^{3+}/Fe^{2+} couple on Au(111) electrode better when annealed at 70 °C in the absorbate solution (2) compared to those prepared at room temperature(1).

(BEs) by 0.3 eV. However, this lies within the error limits of the spectrometer. The pronounced Au $4f_{7/2}$ "bulk" peak (83.84 eV) is found to be in good agreement with literature values (83.95 eV) [97]. In Figure 4.14A are shown the N 1s (399.5eV) and S 2p (163.4eV) emissions. The peaks exhibit a low intensity because of the small photoionization cross-section of these atoms at the respective excitation energy. Nevertheless, the N:S intensity ratio is consistent with the chemical composition of **2b**. The N 1s peak at 399.5 eV corresponds to an oxidation state of N which is the same for similar nitrogen organic compounds [98].

The interaction of sulfur with the Au surface can be elucidated by examining the BEs of S 2p. It is known that elemental sulfur (S8) adsorbed on a metal has an S $2p_{3/2}$ BE of 164.2 eV [99]. Furthermore, sulfur in unbound alkylthiols and disulfides exhibits a positive shift (BE > 163 eV) [97]. Although in our spectra (see Figure 4.14B) we were not able to resolve the S 2p doublet, the peak located at 163.4eV suggests that some amount of sulfur in **2b** is not bound to Au(111). Nevertheless, the shoulder at 162.1 eV clearly seen in the spectra is in good agreement with what has been generally found for alkylthiols bound to Au [97, 100, 101, 102, 103]. The observed difference in BEs with respect to the unbound sulfur is explained as a chemical shift due
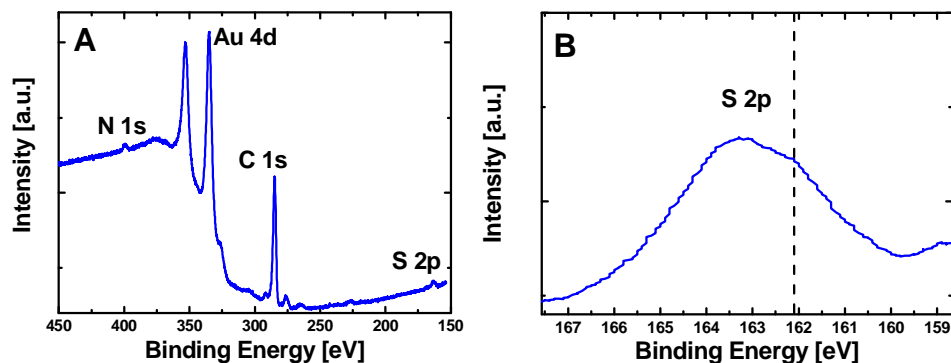
Figure 4.14: (A) XPS spectra of SAMs of **2b** on Au(111); (B) XPS spectra of **2b** and the chemical shift of S 2p level relative to unbound S species.

to the formation of a sulfur-gold bond and by screening of the S 2p core hole by the substrate electrons. This indicates that some "thiolate" like sulfur is formed on the Au surface causing an enhanced adhesion strength of the **2b** monolayer on Au. It is quite unlikely that a S-C bond cleavage takes place upon the adsorption. Moreover, the chemical state of the sulfur is not explicitly known which is not surprising bearing in mind that even in the case of alkylthiols adsorbed on Au the S-H bond dissociation has been questioned recently [104].

The work function of Au(111) modified by the **2b** SAMs has been determined by ultraviolet photoelectron spectroscopy(UPS) simultaneously with the XPS spectra. Figure 4.15A presents the spectra of the **2b** SAM on Au(111) (red line) and the bare gold substrate prepared by sputtering the SAM-Au(111) sample (blue line) for 15 min with an Ar-ion gun. In the case of the sputtered Au substrate, the spectra in the range of 2 - 7 eV show the characteristic Au 5d signal. Indeed, the shoulder at 2.5 eV and the peaks at 4.75 eV and 6.5 eV match with the main peaks of Au 5d. By comparing both spectra, a difference of 0.65 eV in the work function of Au(111) functionalized with **2b** molecules was found. For the evaluation of the work function we took the difference of the total spectra width between the sample with **2b** SAM and the sputtered bare Au(111) substrate [105]. Figure 4.15B represents the calibration of the Fermi levels of both spectra. The change in the work function following the adsorption of molecules onto a clean surface is a
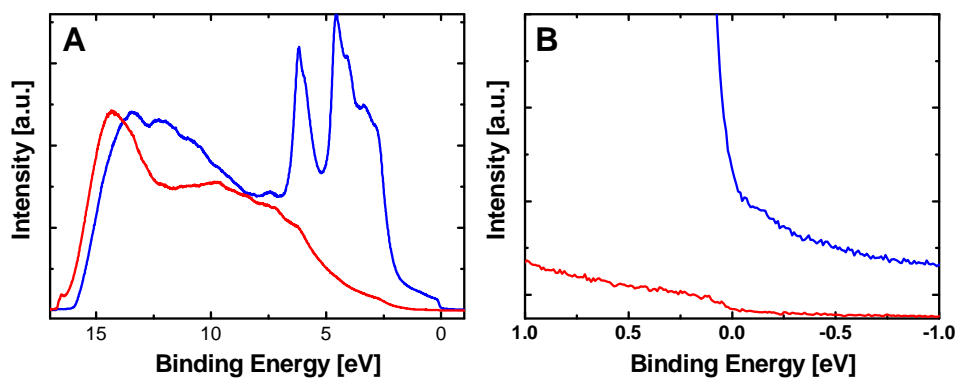
Figure 4.15: (A) Comparison of the UPS spectra of bare Au(111) (blue line) and **2b** modified Au(111) surface (red line) ;(B) enlarged region of respective Fermi energy levels.

well-established fact and the reduced work function can be associated with a partial filling of antibonding orbitals of the adsorbate. This is also supported by theoretical calculations which claim that the S atom in the SAM systems bears a charge of about -0.4e$^-$ [106].

Chapter 5

2D Phase transitions of under potentially deposited Ag on Au(111)

5.1 Introduction

So far we have seen that 2D nanostructuring of surfaces can be achieved by self-assembly of organic molecules. Another strategy to do this includes atomically controlled deposition of metals. Deposition of thin metal films is important not only for fundamental science but also for a variety of applications in fields of catalysis, chemical reaction, fabrication of electronic devices, batteries, corrosion protection and coatings [107,108]. Multilayer metal structures with nanometer-scale thicknesses have been produced by vacuum deposition [109,110,111,112] and chemical vapor deposition processes. However, vacuum deposition techniques require expensive equipment and deposition process is difficult to be controlled. On the other hand patterned metal nanostructures on a foreign metal electrode can be synthesized by chemical reduction and electrodeposition processes [113,114]. Electrochemical deposition and phase formation is more economical and convenient than the growth in vacuum because one can control the morphology of the electrodeposited layers by many factors such as deposition potential, current density, tem-

perature, concentration of metal ion and so on. For instance by limiting
the deposition potential to values positive of the bulk Nernst-potential (the
region is known as underpotential deposition region) the phase formation of
2D structures can be studied, see e.g. [115]. In other words, underpotential
deposition(UPD) provides a window of electrode potentials in which a mono-
layer or less than one can be deposited onto the surface of another metal.
UPD of metals on foreign metal electrodes have been extensively studied
in aqueous solutions. For details about electrochemical phase formation and
crystal growth for these systems the reader is referred to the book of Budevski
and Lorenz [3]. However, UPD mechanism of phase formation in a new class
of solvents called ionic liquids (ILs) is not yet well understood [116, 117]. ILs
are new types of novel electrolytes with extraordinary properties. They con-
sist of anions and cations just like regular table salt but their melting point
lies significantly below 100 °C so they are often liquids at room temperature.
Thanks to their saline character, they have no measurable vapor pressure
bellow their decomposition temperature. From electrochemical point of view
ILs have lots of advantages in comparison to aqueous solutions. First of
all, they have a wide electrochemical window up to 6 V, a good solubility
of corresponding metal salts and high ionicconductivity. These provide an
attractive route to deposit for the first time light, refractory and rare earth
metals as well as elemental semiconductors [118, 119, 120].

Controlled 2D deposition on the nanometer scale of such metals is of great
technological interest and could extend their applications to new generation
batteries, catalysts, coatings, fuel cells and electrochemical sensors including
nanotechnological applications. Ti [121, 122], Ge [123, 124], Si [125], Al, Ni,
Co [126, 127], Zn, Cu, Fe [128] have been successfully electrodeposited from
room temperature ILs. The UPD phenomenon in ILs is also of fundamen-
tal interest to clarify the detailed, microscopic structure of the electrode-
electrolyte interfaces which is not yet fully understood.

Therefore, motivated by the facts mentioned above, our aims were to elu-
cidate and characterize, on one hand, the formation of 2D metal phases on
a metal substrate in an ionic liquid in comparison to aqueous electrolytes
by electrochemical and in-situ probe methods and, on the other hand, to

reveal the mechanism of UPD by Monte Carlo computer simulations in both electrolytes. As an electrochemical system Ag on Au(111) was chosen for two main reasons. First, silver has almost a negligible lattice misfit with gold and its Ag-Au binding energy is higher than the binding energy Ag-Ag which makes the system suitable for studying UPD processes. Second, this system has been extensively studied concerning the UPD phenomenon in aqueous solutions over the past years.

5.2 Results

In this chapter, in-situ STM and electrochemical studies are presented for UPD of Ag on Au(111) in aqueous, Sec. 5.2.1, and ionic electrolytes, Sec. 5.2.2.

### 5.2.1 UPD of Ag on Au(111) in aqueous electrolytes

For electrochemical and in-situ STM experiments, the under potential deposition (UPD) of Ag was examined on Au(111) single crystal electrode. A typical cyclic voltammogram recorded on a Au(111) in 1 mM Ag_2SO_4 + 0.1 M H_2SO_4 at a sweep rate of 30 mVs^{-1} is shown in Figure 5.1. The UPD of Ag on Au(111) is characterized by two major pairs of voltammetric peaks at 520 mV (C1) and 25 mV (C3) indicating that two distinct processes occur at the interface in the UPD region. All cathodic processes (C1,C2,C3) are related to the reduction(deposition) of Ag^+ cations on the electrode surface ($Ag^+ + e^- = Ag^0$) whereas anodic processes are associated with dissolution ($Ag^0 - e^- = Ag^+$) of Ag adatoms.

A weak reversible redox couple is also apparent at 130 mV (C2). The voltammetry and the corresponding peak positions are in good agreement with the literature [129,130]. At 520 mV (C1) the first UPD of Ag on Au(111) occurs with a corresponding anodic peak at 528 mV (A1).
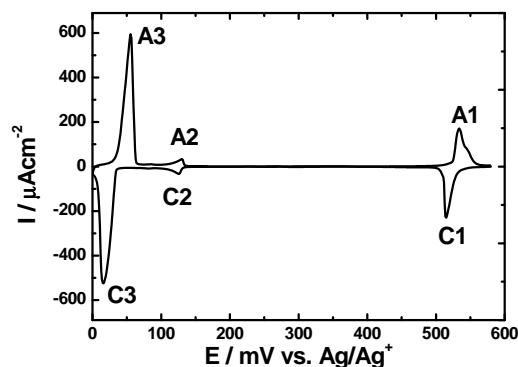
Figure 5.1: Cyclic voltammogram recorded on single crystal Au(111) in 1 mM Ag_2SO_4 + 0.1M H_2SO_4 at a sweep rate of of 30 mVs^{-1}.

Figure 5.2 shows the stripping anodic curves of the first UPD process(A1) taken at different sweep rates. The peak current potential positions with increasing the sweep rate satisfies the criteria for a reversible nernstian behaviour [2]. In addition, the symmetry in the shape of CV curves suggests that the process is under adsorption control. This is also supported by the linear dependence of the peak current against the sweep rate, see Figure 5.2B. For details about electrode reactions driven by adsorption, see Sec. 2.3.3. The same electrochemical behavior was found for process C3.
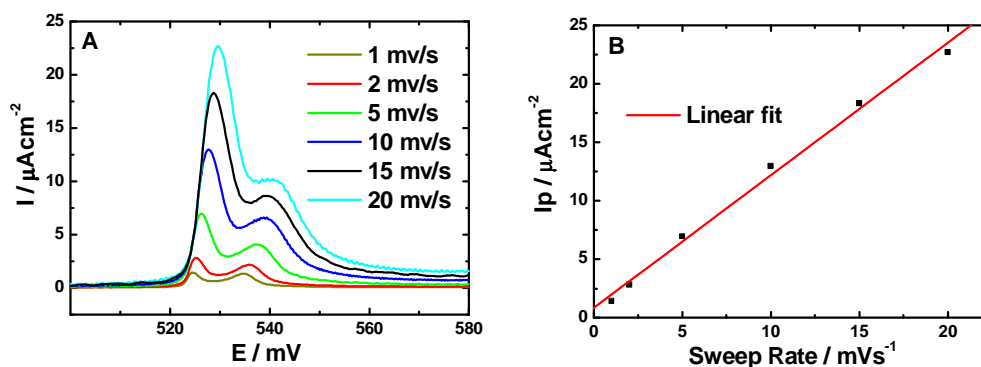

Figure 5.2: (A) Anodic linear sweep voltammetry of the first UPD at different sweep rates ;(B) Peak current is proportional to the sweep rate indicating adsorption phenomenon.

The stripping current curves of Ag taken at a sweep rate of 1 mVs^{-1} after the substrate has been polarized at a certain potential in the range of the cathodic wave (C1) until the cathodic current is almost zero, are presented in Figure 5.3A. In fact, the anodic stripping waves are divided into two peaks which occur at 528 mV and 539 mV. The potential difference between the two maxima (Figure 5.3A) was found to be 11 mV and appears to be independent on the sweep rate. Also, the double peak is already manifested as a shoulder of A1 in the voltammogram, see Figure 5.1.
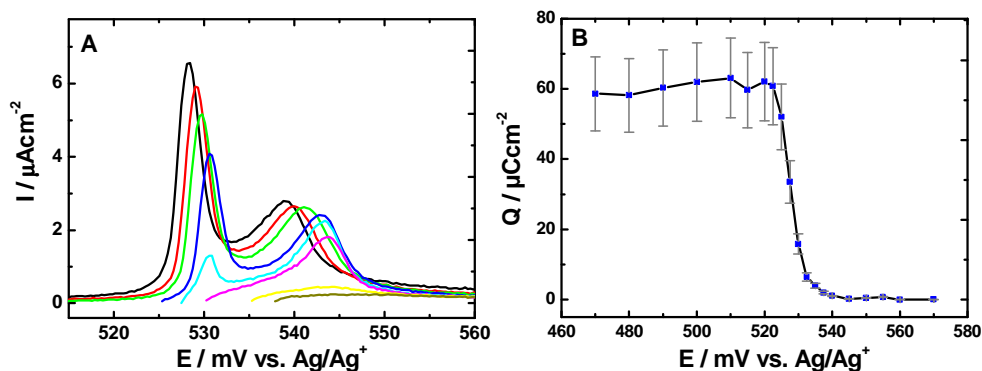
Figure 5.3: (A) Anodic linear sweep voltammograms with a sweep rate of 1 mVs^{-1} ;(B) desorption isotherm for the first UPD of Ag (C1) at 520 mV derived from measurements using the loop technique.

It is interesting to know how much charge is associated with the first peak (C1). Therefore, sets of charge measurements were carried out by means of linear sweep voltammetry (LSV) employing the loop method with an initial potential of 600 mV, various final potentials and polarization times of 300 s [3]. From this a desorption isotherm is derived, as shown in Figure 5.3B. The charge consumed for the first UPD of Ag (C1) including the uncertainty of the double layer charging correction was found to be 55 ± 10 μCcm^{-2}. Taking into account that 1 pseudomorphic monolayer (ML) of Ag is associated with a charge density of 222 μCcm^{-2}, the silver coverage is estimated 0.25 ML suggesting the formation of a more open adlayer of silver.
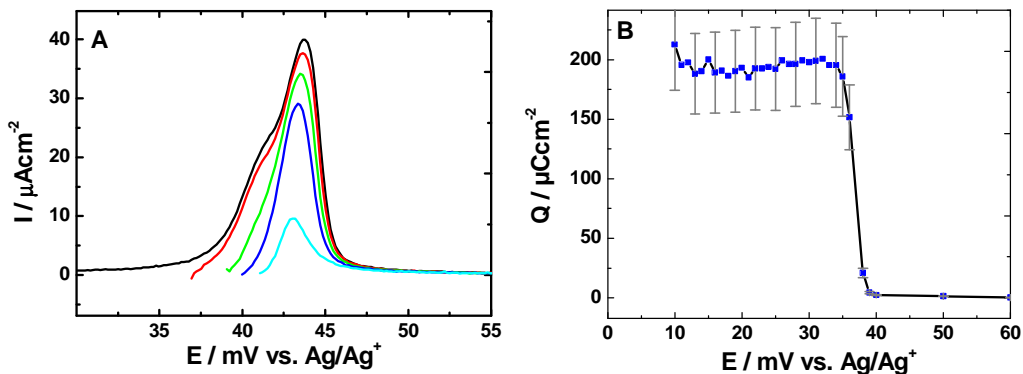
Figure 5.4: (A) Dissolution sweep curves for the second UPD of Ag (C3) taken with a sweep rate of 2 mVs^{-1} ;(B) desorption isotherm for C3 derived from measurements using the loop technique.

With respect to the second major redox peak at 25 mV (C3), the derived desorption isotherm shows that the charge density involved is 190 ± 36 μCcm^{-2} (Figure 5.4B). The charge density includes the contribution of the weak redox couple at 130 mV (C2) which is thought to be caused by a commensurate-incommensurate transition [131]. A brief assessment suggests that for both UPD processes of Ag the total charge density of 245 μCcm^{-2} can be ascribed to the formation of one silver ML.

In concluding the CV results, the UPD of Ag exhibits two distinct surface processes. At 520 mV an expanded adlayer of silver is formed corresponding to surface coverage of 0.25 ML. Sweeping the potential just before the commencement of the bulk Ag deposition, a transition from an expanded to a pseudomorphic monolayer of Ag on Au(111) occurs.

It is interesting to analyze how well the electrochemical examination of UPD of Ag on Au(111) presented so far corresponds to in-situ STM studies. In these experiments attention was focused on the surface processes accompanying the first UPD of Ag (C1/A1). Figure 5.5A shows an in-situ STM image of Ag on a large scan (500 nm x 500 nm) obtained at 500 mV. The STM image reveals a compact adlayer of Ag exhibiting a small number of monoatomically deep holes and islands. The adlayer covers the whole surface following the topography of the substrate and terminates at the monoatomic step edge of Au(111) as shown in Figure 5.5A. The adlayer of Ag is atomically ordered as

one can conclude from the 40 nm x 40 nm in-situ STM image (Figure 5.5B).
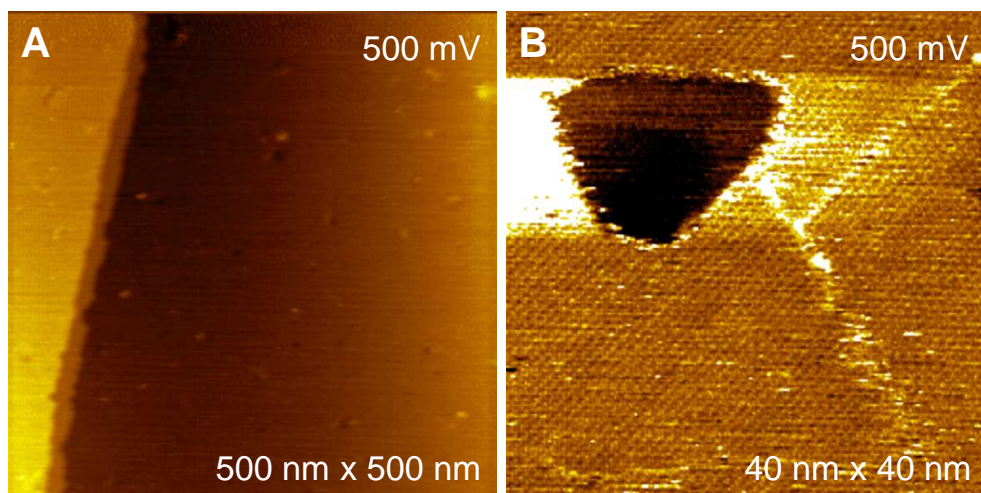
Figure 5.5: In-situ STM images of the first UPD adlayer of Ag at 500 mV on Au(111). (A) Ag adlayer on a large scan of 500 nm x 500 nm ;(B) atomically ordered Ag adlayer resolved at 40 nm x 40 nm, I_t=0.5 nA, U_{bias}=-0.3 V.

Moreover, a high resolution image at the same potential reveals individual silver adatoms packed into an ordered adlayer exhibiting a spacing of a=8.3 $\pm$ 0.5 Å and b=8.2 $\pm$ 0.2 Å between the adjacent adatoms that have the same contrast and an angle of Γ=110 $\pm$ 5° (see Figure 5.6A). The interatomic distances suggest a (3 x 3) superlattice, although the angle in the unit cell deviates from the theoretical 120°. A schematic representation of the adlayer with the (3 x 3) structure on Au(111) is given in Figure 5.6B in which the open circles represent Au(111) surface atoms whereas the filled grey ones are Ag adatoms at atop sites and filled black ones are Ag adatoms at bridging sites. The model clearly shows that silver atoms take both atop and 2-fold bridge sites. Interestingly, the pattern of alternating higher and lower rows is exactly what is seen in the STM image (Figure 5.6A). The modulation of height in the $<1\bar{1}0>$ direction is less pronounced than that one in the $<11\bar{2}>$ direction.
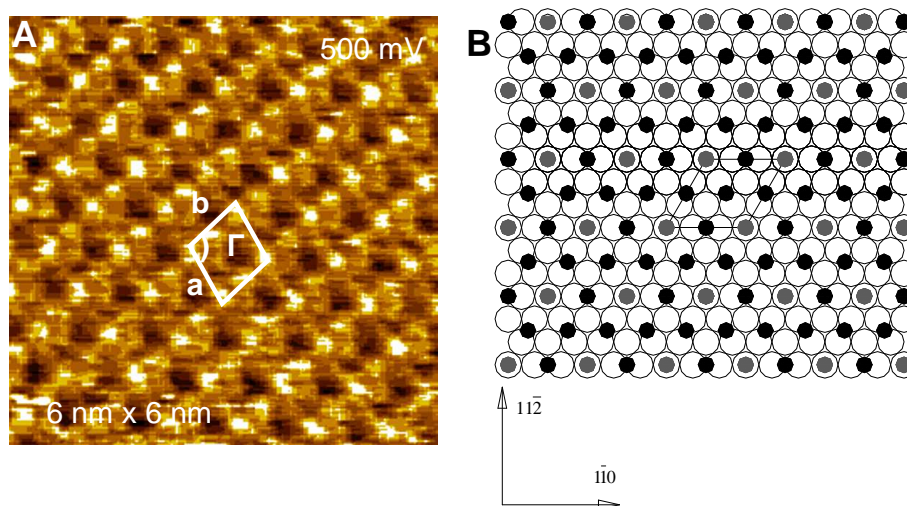
Figure 5.6: (A) Atomically resolved STM image of a 6 nm x 6 nm region of the Ag adlayer exhibiting interatomic spacing of a=8.3 ± 0.5 Å, b=8.2 ± 0.2 Å, and Γ=110 ± 5°.The modulation of height in $<11\bar{2}>$ is a result of alternating adatoms in atop and 2-fold bridging sites. I_t=1 nA, U_{bias}=-0.2 V ;(B) Schematic representation of (3 x 3) structure of Ag on Au(111). Note that filled gray small circles represent Ag adatoms at atop sites, whereas the black ones represent Ag adatoms at bridging sites.

The dissolution process of Ag for the first UPD on Au(111) is manifested by the sequential STM images presented in Figure 5.7. The potential was swept from 500 mV to 600 mV in the middle of the scan to elucidate the stripping of the (3 x 3) adlayer of Ag (Figure 5.7A). Some residuals of the layer are still observed in a short time at 600 mV (Figure 5.7B). After removal of Ag , a number of monoatomically deep pits with diameters between 2 and 10 nm are seen in the basal plane of the Au(111) (Figure 5.7C,D). These pits were found to anneal very slowly with time. Moreover, it is thought that an initial stage of oxidation of the gold preferentially takes place at the step sites as revealed from the corrugation of the step edges. It should be noted that similar pitting of the Au(111) terraces in sulphate [132] and perchlorate [133] solutions has been observed only by a potential excursion to 900 mV (1300 mV vs. SCE)[1] and a subsequent reduction of the gold oxide species. Although special care was taken in our measurement that the substrate was not exposed to such

---

[1]400 mV vs. Ag/Ag$^+$ corresponds to 0 mV vs. SCE

high potentials, the formation of pits indicates that this is a consequence of the stripped layer of silver and its strong interaction with the underlying gold surface which is a strong indication of surface alloying between Ag and Au.
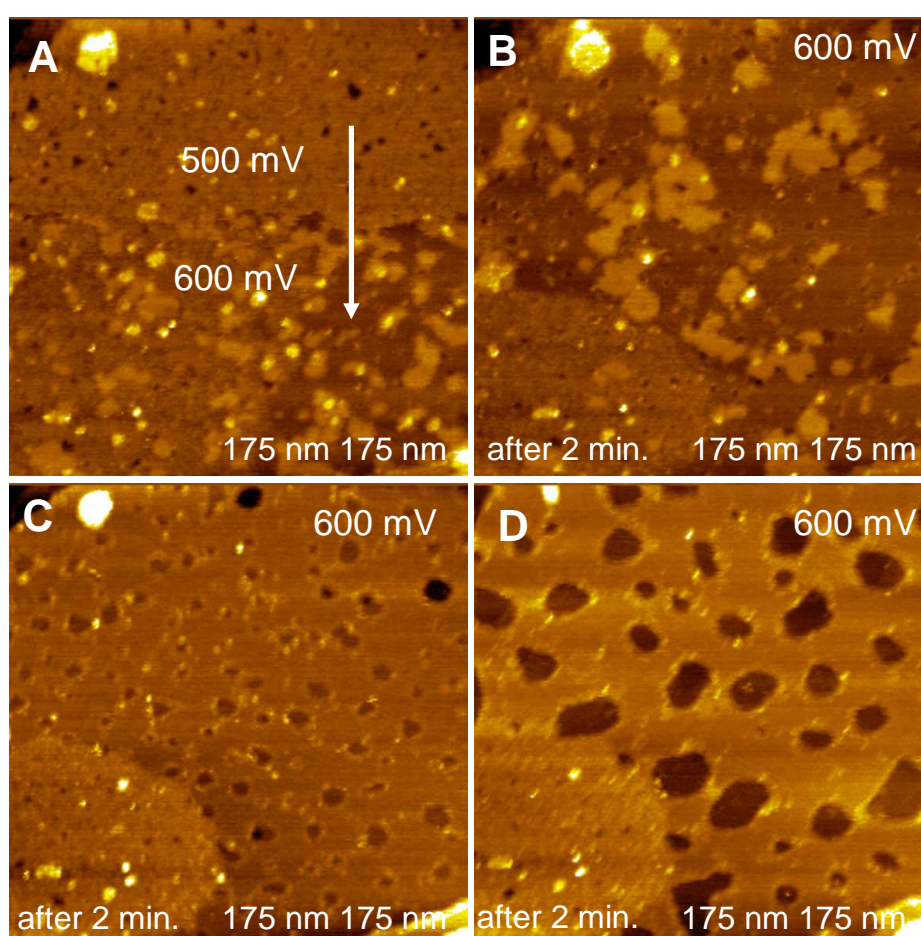
Figure 5.7: In-situ STM images of stripping of the first UPD Ag adlayer on Au(111) in 1 mM Ag_2SO_4 + 0.1M H_2SO_4 on a large scan of 175 nm x 175 nm. I_t=1 nA, U_{bias}=-0.1 V ;(A) in the middle of the scan the potential was switched from 500 mV to 600 mV. The scanning direction is from top to bottom ;(B) the next sequential scan at 600 mV shows that some islands of the adlayer of Ag still remain ;(C) 2 min. later the STM image reveals a number of pits in the surface which are filled with Ag ;(D) the following scans show that Ag is utterly dissolved from the pits resulting in formation of monoatomically deep gold pits.

5.2.2 UPD of Ag on Au(111) in ionic liquid

First of all, it is necessary to compare the voltammogram of the pure ionic electrolyte with the one obtained from a solution in which a 10 mg crystal of AgCl was dissolved in $[BMI]^+[AlCl_4]^-$. The comparison (Figure 5.8A) clearly shows that the silver containing melt exhibits two additional redox couples around 350 mV and 50 mV which we associate to the first and second UPD processes of Ag, respectively. A typical cyclic voltammogram recorded in 2 mM AgCl + $[BMI]^+[AlCl_4]^-$ on Au(111) at a sweep rate of 50 mVs^{-1} is shown in Figure 5.8B. The occurrence of the redox couple at 990 mV (C1) and 1025 mV (A1) was found to be independent of the content of silver in the melt implying that the process is characteristic of the Au(111)-BMICl:AlCl$_3$ interface. A charge density of 73 ± 14 μCcm^{-2} was derived from the CV. This process has been ascribed to a two dimensional (2D) dissolution/deposition of gold occurring preferentially at step edges [134]. Further reducing the potential leads to their reduction and deposition. 3D dissolution of gold should be expected at more positive potentials but the electrochemical window of the ionic liquid is limited to 1200 mV where decomposition of the ionic liquid
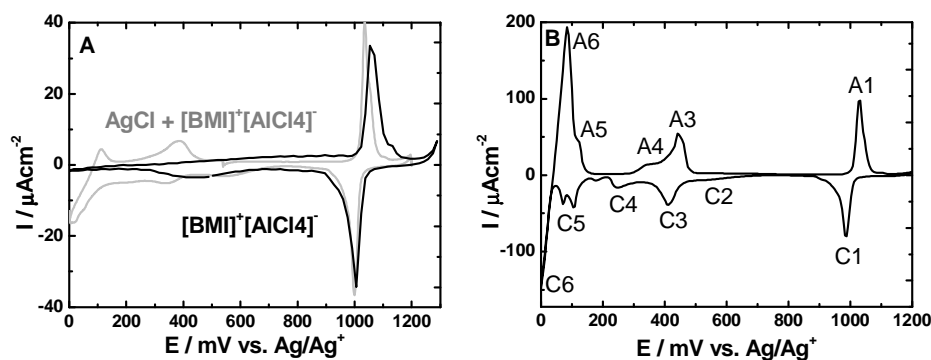
Figure 5.8: (A) Cyclic voltammogram recorded on single crystal Au(111) at a sweep rate of 20 mVs^{-1} in 58:42 mole ratio AlCl$_3$:BMICl before (black line) and after (grey line) small amount of AgCl is added ;(B) CV taken in 2 mM AgCl + AlCl$_3$:BMICl at a sweep rate of 50 mVs^{-1}.

Another interesting feature of the CV concerns the broad feature in the range between 500 to 600 mV (C2) which is also independent of the content of Ag
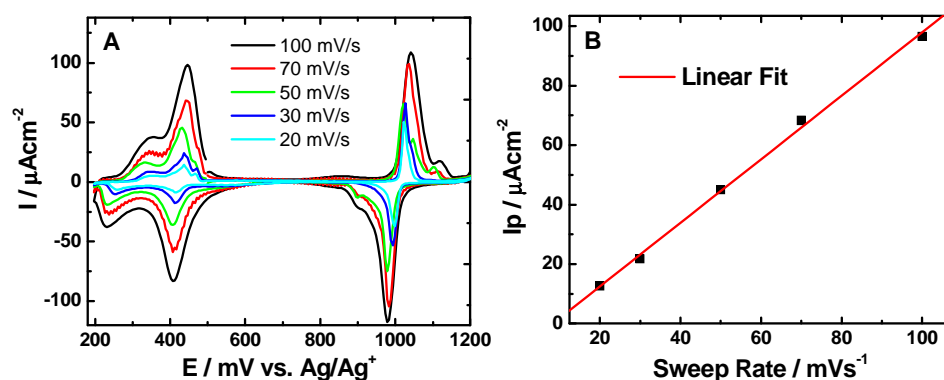
Figure 5.9: (A) Anodic linear sweep voltammograms for C3 and C4 at different sweep rates ;(B) Peak current is proportional of the sweep rate indicating that C3 and C4 are controlled by adsorption of Ag.

(see Figure 5.8A). Prior to the first UPD of Ag, we interpret this process as chemisorption of tetrachloroaluminate anions. Further evidence in this regard will be given while displaying the STM images in this potential range. According to the CV the first UPD of silver arises at two different potentials at 410 mV (C3) and 230 mV(C4) indicating two distinct surface processes. From the linear dependence of the peak current against the sweep rate, we conclude that C3 and C4 processes are driven by the adsorption of Ag on Au(111) surface, see Figure 5.9B. The same electrochemical behavior is observed for the second UPD at 120 mV and 106 mV.

In order to clarify to what extent Ag covers the Au(111) surface in the respective UPD regions, a desorption isotherm was derived on the basis of charge measurements. The isotherm is plotted in Figure 5.10 that shows charge densities of 131 ± 25 μCcm^{-2} (0.59 ML) and 220 ± 42 μCcm^{-2} (0.99 ML) for the first and the second UPD, respectively. This result clearly shows formation of one ML of Ag in the UPD range as in aqueous solutions.

Prior to the first UPD process of Ag the Au(111) surface was examined by STM at 550 mV. High resolution imaging acquired at this potential reveals for the first time a well ordered layer of chemisorbed tetrachloroaluminate anions on Au(111) (Figure 5.11A). The superlattice derived from the 2D fast Fourier transforms (FFT) of the STM data is presented in the inset of
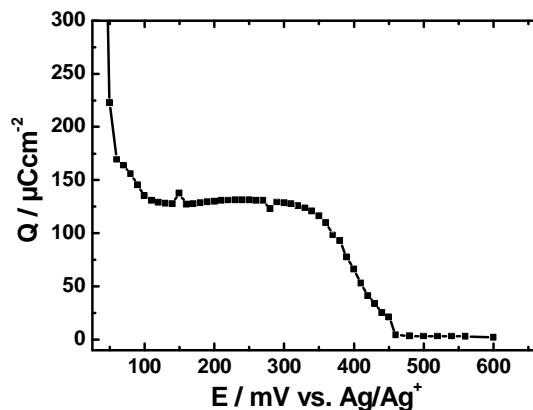
Figure 5.10: Desorption isotherm derived from coulorimetric measurements in the whole UPD range of Ag in $[BMI]^+[AlCl_4]^-$ on Au(111).

Figure 5.10B. The adsorbed tetrahedral ionic complex leads to a structure with lattice constants of a=8.3 $\pm$ 0.5 Å and 9.8 $\pm$ 0.5 Å. The unit cell is equivalent to a (1.65 x $\sqrt{3}$)R30° structure and seems to be incommensurate with the underlying Au(111). It is thought that tetrachloroaluminate species are chemisorbed with the tetrahedral face adjacent to the Au(111).

Reducing the potential towards 400 mV the first UPD of Ag takes place. The initial stage of nucleation and growth process is manifested by the sequence of in-situ STM images as shown in Figure 5.12. At 400 mV a layer of Ag starts growing from the monoatomic step edges as well as on the terraces of Au(111) (Figure 5.12A). The new silver phase seems to be less in height than a monoatomic Au(111) step. Its growth at constant potential is demonstrated on a large scan range of 350 nm x 350 nm (Figure 5.12B,C) within a time span of 8 minutes. At 300 mV, the 2D silver islands grow and merge with one another until a certain level. As a result an inhomogeneous adlayer is formed with partial coverage. The same conclusion can be drawn on the basis of coulometry from which 0.59 ML coverage is expected. This is in contrast to aqueous solutions where a homogeneous open (3 x 3) adlayer of silver develops after the first UPD (see Figure 5.5).

Figure 5.13 illustrates the dissolution of the inhomogeneous adlayer when the potential is gradually stepped back to 500 mV. As in aqueous solutions the dissolution of the Ag adlayer leads to a pitting in the Au(111) sur-
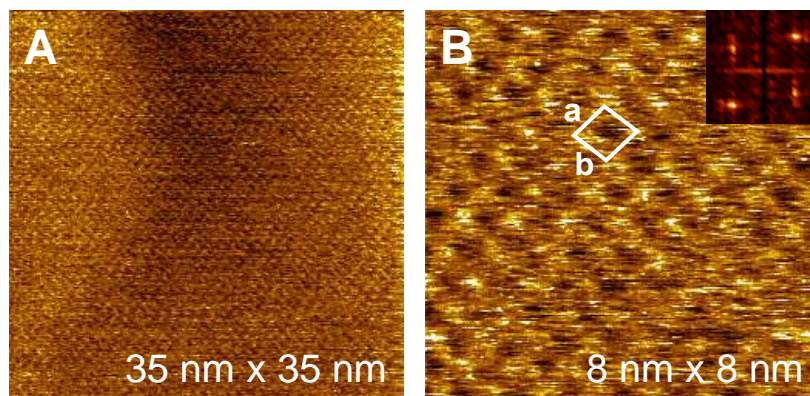
Figure 5.11: In-situ STM images of an ordered adlayer of $AlCl_4^-$ on Au(111) at 500 mV in $AlCl_3$:BMICl. I_t=1 nA, U_{bias}=0.1 V ;(A) a 35 nm x 35 nm region ;(B) a 8 nm x 8 nm region. Inset shows the superlattice of $AlCl_4^-$ derived from 2D FFT of the STM image yielding lattice constants of a=8.3 $\pm$ 0.5 Å and b=9.8 $\pm$ 0.5 Å.
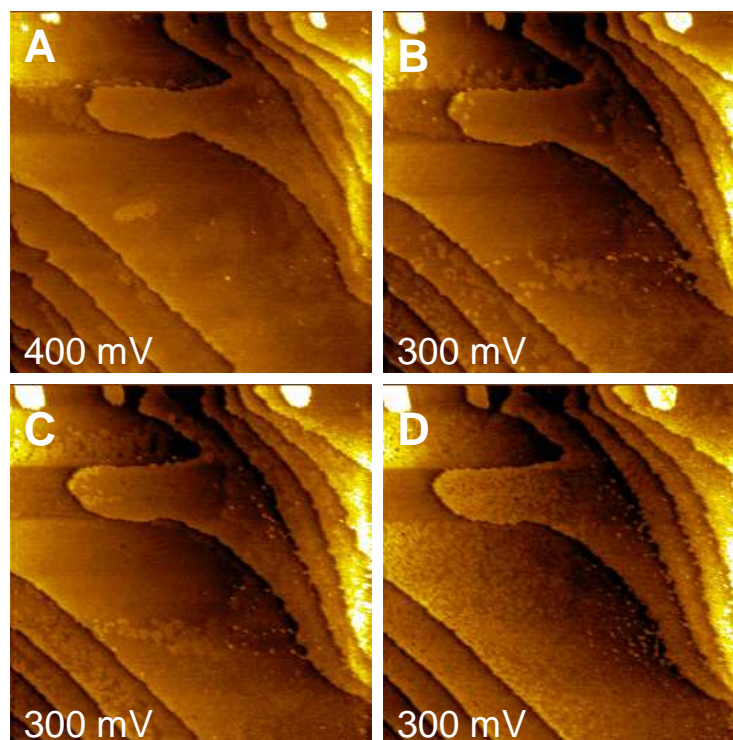
Figure 5.12: A sequence of in-situ STM images (350 nm x 350 nm) showing the initial stages of nucleation and growth for the first UPD of Ag in $AlCl_3$:BMICl, I_t=1 nA, U_{bias}=0.1 V ;(A) at 400 mV ;(B) at 300 mV ;(C) at 300 mV 8 minutes later ;(D) at 300 mV 16 min later.
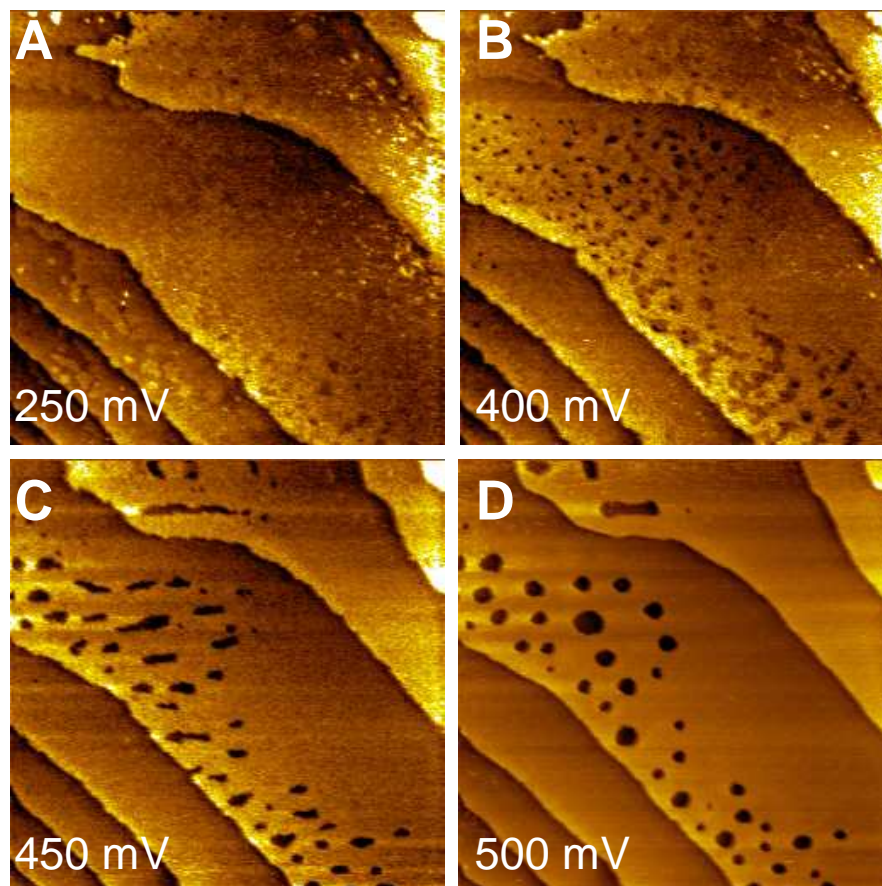
Figure 5.13: In-situ STM images of the dissolution (300 nm x 300 nm) of the first Ag adlayer on Au(111) in AlCl$_3$:BMICl, I$_t$=1 nA, U$_{bias}$=0.05 V. (A) at 250 mV ; (B) at 400 mV ;(C) at 450 mV ;(D) at 500 mV.

face, but now with a very pronounced structure. After dissolution numerous monoatomically deep holes with diameters between 5 and 20 nm are seen all over the Au terraces as shown in Figure 5.13D. This observation is consistent with the previous STM study [134]. Due to the long polarization time which was needed for the acquisition of STM images before the dissolution (about 30 min) we explain the pitting as a result of 2D Ag-Au surface alloying.

Another set of subsequent STM images obtained at 500 mV after dissolution reveals that the monoatomically deep pits disappear relatively fast with time, see Figure 5.14. At first the smaller pits vanish and changes in the shape of the step edges become apparent as depicted in Figure 5.14C,D. The surface

recovers very fast within approximately 20 minutes due to rapid surface diffusion of Au adatoms left on the surface after the dissolution of the Au_xAg_y surface alloy [135]. It is known that the rate of diffusion in the solution containing chloride ions is faster than that in a 0.1 H_2SO_4 medium [133, 136]. Therefore, such difference in kinetics of annealing the pits can be expected comparing sulphuric solutions with ionic liquids.
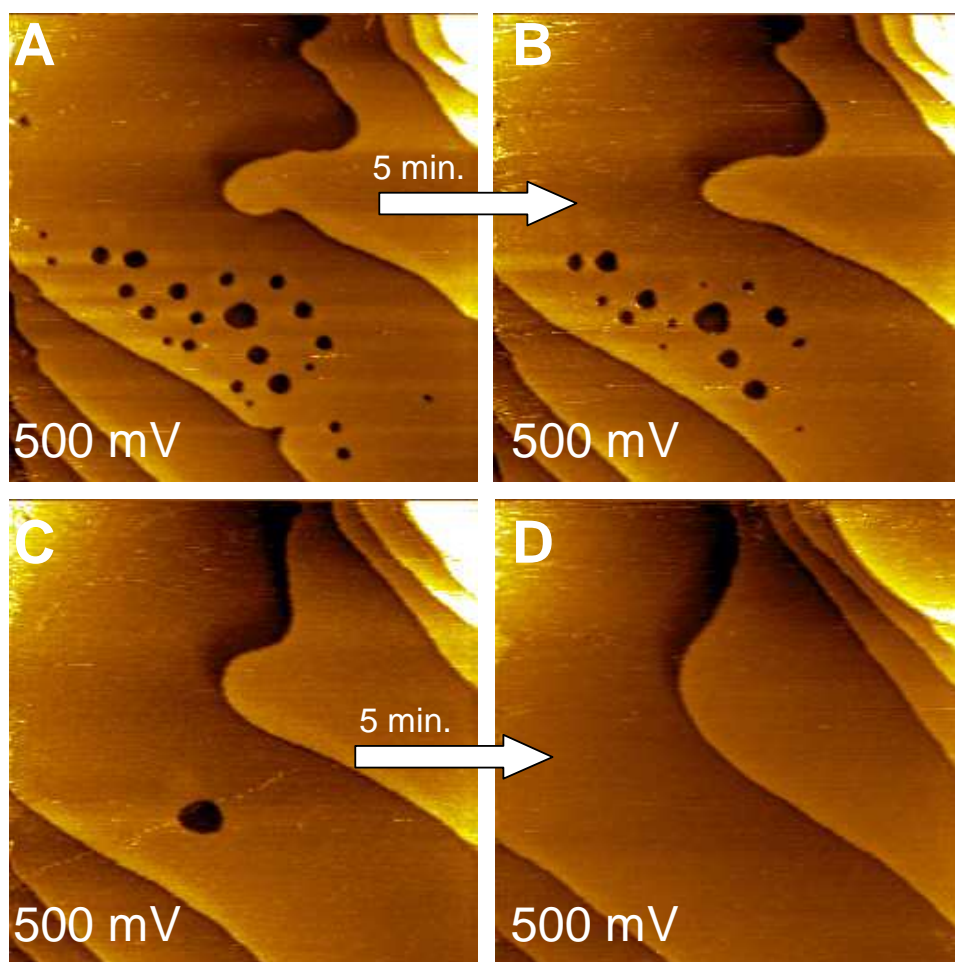
Figure 5.14: Sequence of in-situ STM images (300 nm x 300 nm) at a constant potential of 500 mV after dissolution of the first Ag adlayer on Au(111) in AlCl$_3$:BMICl which show the annealing of the pits in the surface with time, I$_t$=1 nA, U$_{bias}$=0.05 V. (A) 0 min. ;(B) 5 min. ;(C) 10 min. ;(D) 15 min.

Another interesting result concerns the fact that the first UPD of Ag on Au(111) in BMICl:AlCl$_3$ undergoes a completely different mechanism in comparison with that in sulphuric media. As one can see from the CV (see Figure 5.8B) the first UPD of Ag has two distinct peaks separated by nearly 200 mV whereas in aqueous only one peak is observed. So, the question arises: What is the origin of these two peaks? In order to obtain an unambiguous answer we have examined by STM the Ag adlayer on the Au(111) at a potential of 300 mV at which both processes related to the C3 and C4 peaks take place. On a large scan size of 200 nm x 200 nm (Figure 5.15A,B) the silver adlayer exhibits many inhomogeneities as well as monoatomically deep holes. Moreover, we have found for the first time that two distinct domains of condensed and expanded surface structures of Ag coexist at 300 mV. The condensed structure (indicated with a pointer in Figure 5.15A) appears to be smoothed whereas the expanded structure seems to be rough and atomically disordered (Figure 5.15C). An atomically resolved STM image of the condensed phase is depicted in Figure 5.15D. In this instance the image reveals a well ordered structure of the silver monolayer. 2D FFT of the STM data yields a typical unit cell (presented in the inset of Figure 5.15D) with interatomic distances of a=4.4 $\pm$ 0.6 Å, b=5.6 $\pm$ 0.5 Å, and Γ=59 $\pm$ 3°. This result indicates that the silver adlayer in the condensed domains has a packing comparable to that of a compressed ($\sqrt{3}$ x $\sqrt{3}$)R30° monolayer.

Sweeping the potential further in the negative direction to 200 mV (on the left side with respect to the C4 peak) induces new structural changes. The expanded phase is being converted into the compressed one resulting in a smoothing of the surface as shown in Figure 5.16. This observation makes us think that the C4 peak in the CV is a result of a transition from the expanded into the compressed ($\sqrt{3}$ x $\sqrt{3}$)R30° structure of the silver adlayer. Interestingly, stepping back the potential to 400 mV induces the reverse transition from compressed to expanded structures. Such experimental evidence shows for the first time that the process of Ag UPD on Au(111) in [BMI]$^+$[AlCl$_4$]$^-$ undergoes a completely different scenario in comparison with that in aqueous solutions.

As seen in Figure 5.17 with respect to the second UPD of Ag we have found
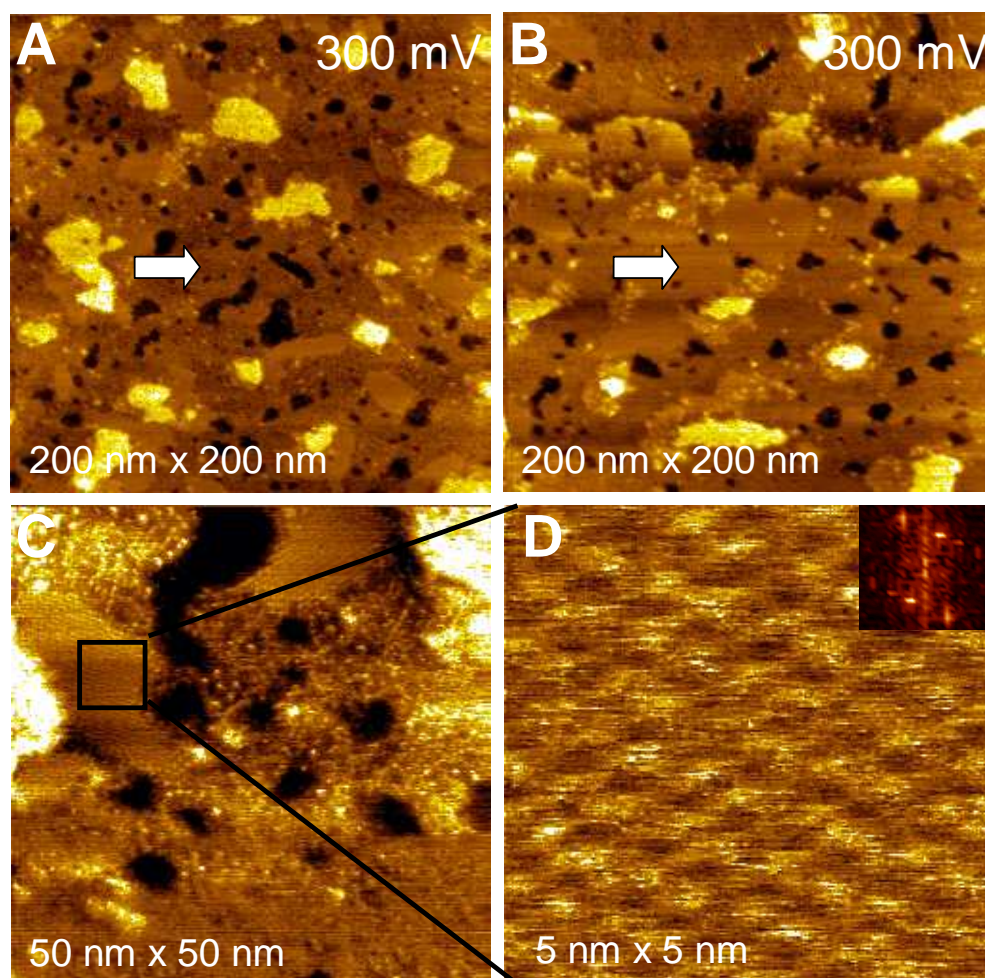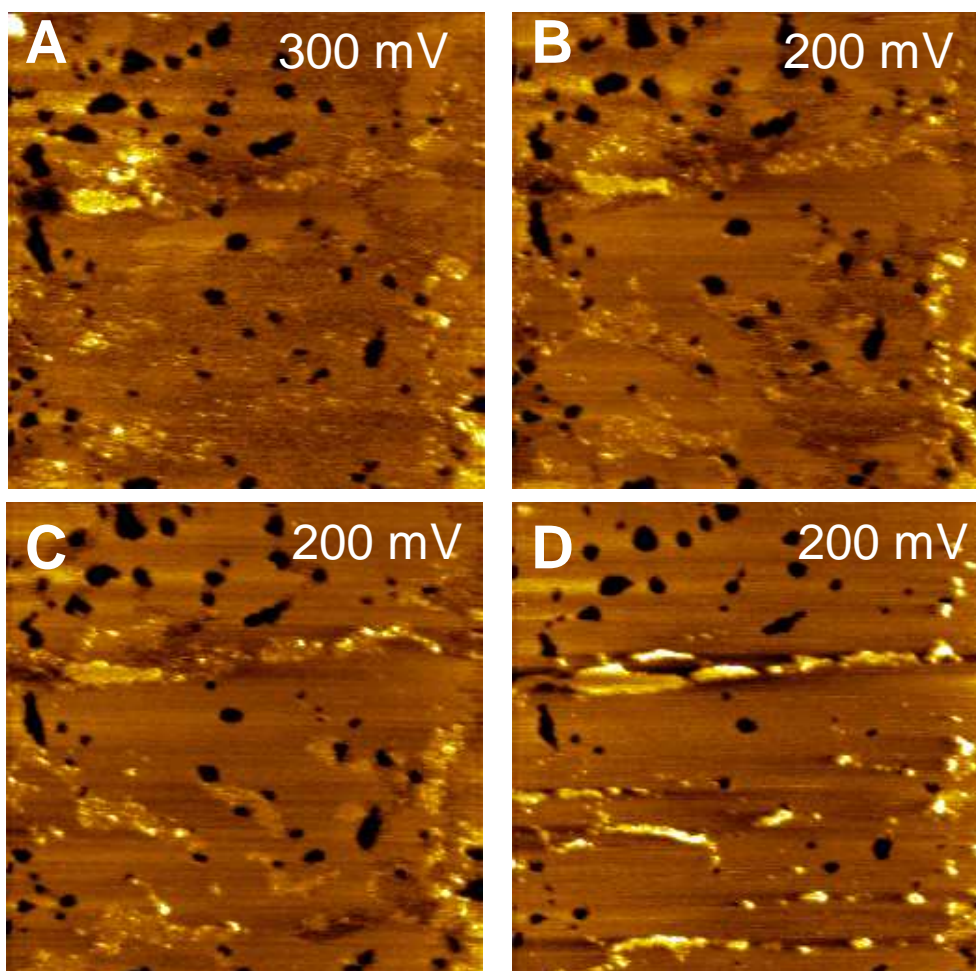
Figure 5.15: In-situ STM images (200 nm x 200 nm) of the first Ag adlayer on Au(111) in AlCl$_3$:BMICl at 300 mV. Arrows show domains of dissordered (A) and dense packed (B) Ag phase. (C) 50 nm x 50 nm ;(D) 5 nm x 5 nm high-resolution STM image of the dense packed Ag phase. Inset shows the superlattice of the packed Ag phase obtained from 2D FFT of the STM image yielding superlattice constants of a=4.4 $\pm$ 0.6 Å , b=5.6 $\pm$ 0.5 Å, and Γ=59 $\pm$ 3°.

Figure 5.16: STM images (200 nm x 200 nm) indicate disorder-order transition when the potential is switched from (A) 300 mV to (B) 200 mV. (C) and (D) show next sequential scans at 200 mV where the Ag adlayer becomes more smoothened. The domains of the dense packed Ag adlayer expand at the expense of the disordered phase, I_t=1 nA, U_{bias}=0.1 V.

that in terms of STM approaching the potentials in the range 120 mV to 100 mV nearly all the monoatomically deep holes in the silver adlayer are filled giving approximately coverage of 1ML as determined from coulometry. Further reducing the potential to 50 mV causes a rapid formation of a second and third layer of Ag approaching the overpotential deposition region(OPD).
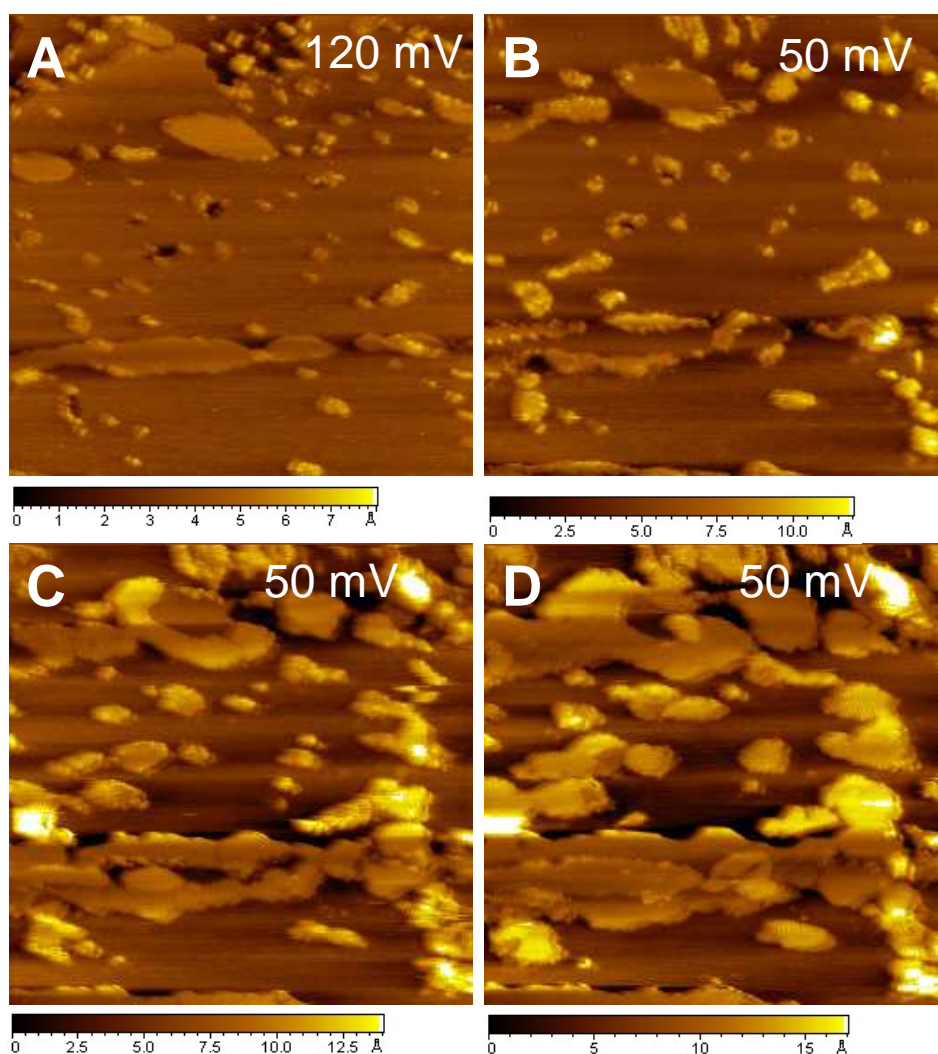
Figure 5.17: In-situ STM images (300 nm x 300 nm) on Au(111) in AlCl$_3$:BMICl. (A) at 120 mV ;(B) at 50 mV ;(C) next scan after 2 min ;(D) 2 min later, I$_t$=1 nA, U$_{bias}$=0.1 V.

5.3   Disscusion

5.3.1   Comparison of UPD of Ag on Au(111) in aqueous and ionic electrolytes

As is well known, under potential deposition(UPD) is considered as the initial stage of elecrocrystallization. Electrocrystallization of metals takes place at electrified electronic conducting substrate/ionic conducting electrolyte interface which includes, in general, three important steps:

(1) Formation of metal adatoms, Me_{ads}, on native metal substrates, Me, or on foreign substrates, S, by adsorption and fast charge transfer

(2) Two-dimentional (2D) and three-dimentional (3D) Me phase formation

(3) Crystal growth of 3D Me bulk phase.

A 2D Me phase is considered as a specific adsorbate located in the inner Helmholtz plane of the electrochemical double layer existing at a substrate/electrolyte interface. In this particular study of UPD of Ag on Au(111) we focus on the first two stages. There are two major factors that have to be considered in the process of UPD: thermodynamics of 2D Ag phases and the properties of the electrolyte phase which strongly affect the structure of the substrate/electrolyte interface. For 3D Ag phase formation and growth on native(or foreign) substrate and dissolution of the 3D Ad phase, the overall reaction is

$$Ag^0 = Ag^+_{solv} + e^-, \tag{5.1}$$

where $Ag^+{}_{solv}$ are solvated silver ions in the electrolyte phase. The actual electrode potential, E, determines the direction of 5.1. Thermodynamically, the equilibrium Nernst potential, E_{3DAg/Ag^+} for 3D Ag phase is given by

$$E_{3DAg/Ag^+} = E^0_{3DAg/Ag^+} + \frac{RT}{nF} \ln \frac{a_{Ag^+}}{a_{3DAg}}. \tag{5.2}$$

The 3D bulk Ag phase is unstable at $E > E_{3DAg/Ag^+}$ and dissolves anodically. At these positive potentials with respect to the equilibrium Nernst potential

2D Ag phase is stable and different 2D phase transitions may take place on the substrate surface. This region is known as UPD region. By definition, UPD of any metal happens at undersaturation, $\Delta\mu < 0$. Supersaturation and undersaturation is determined by

$$\Delta\mu = \mu_{Ag_{ads}} - \mu_{Ag_{0,ads}} = -F\left(E - E_{3DAg/Ag^+}\right), \tag{5.3}$$

where μ is the chemical potential.

Phase formation of metals on a foreign substrate(S) can be classified into three different mechanisms, namely, *Vomer-Weber (VW)*, *Frank-van der Merwe(FM)*, and *Stranski-Krastanov (SK)* modes depending on the Me_{ads}-S binding energy and the crystallografic mismatch between S and 3D Me bulk deposit. Considering the deposition process near equilibrium conditions, three different growth modes can be distinguished as manifested in Figure 5.18. In VW mode, the binding energy of Me_{ads} on S, $\Psi_{Me_{ads-S}}$, is lower than that on the metal itself, $\Psi_{Me_{ads-Me}}$. Consequently, 3D Me bulk phase formation takes place on an unmodified substrate and the VW mode is favored indipendent of crystallografic mismatch. When $\Psi_{Me_{ads-S}} >> \Psi_{Me_{ads-Me}}$, a two-dimensional(2D) metallic monolayer can be formed in the UPD range, and there are two possible growth mechanisms for the subsequent growth of the metallic layers depending on the crystallografic mismatch. In the FM mode the crystallografic mismatch of Me and S is negligibly small, metalic layers are deposited on the substrate by a layer-by-layer growth. In the SK case, the crystallografic mismatch is relatively large, the UPD layer contains considerable internal strain and therefore, the growth of unstrained 3D Me islands on top of the strained UPD Me layers is energetically favored.

The crystallografic mismatch between Ag and Au is almost zero. Atomic diameters of Ag and Au are 2.88 Å and 2.89 Å respectively. In this sence, FM growth mode is expected for this system. Indeed, this kind of electrodeposition is observed. In aqueous and ionic electrolytes, a uniform homogeneous monolayer(ML) of Ag is formed in the whole UPD range confirming the pseudomorfic layer-by-layer growth mode. At more positive potentials, as the results have shown, two distinct surface processes occur on the Au(111)
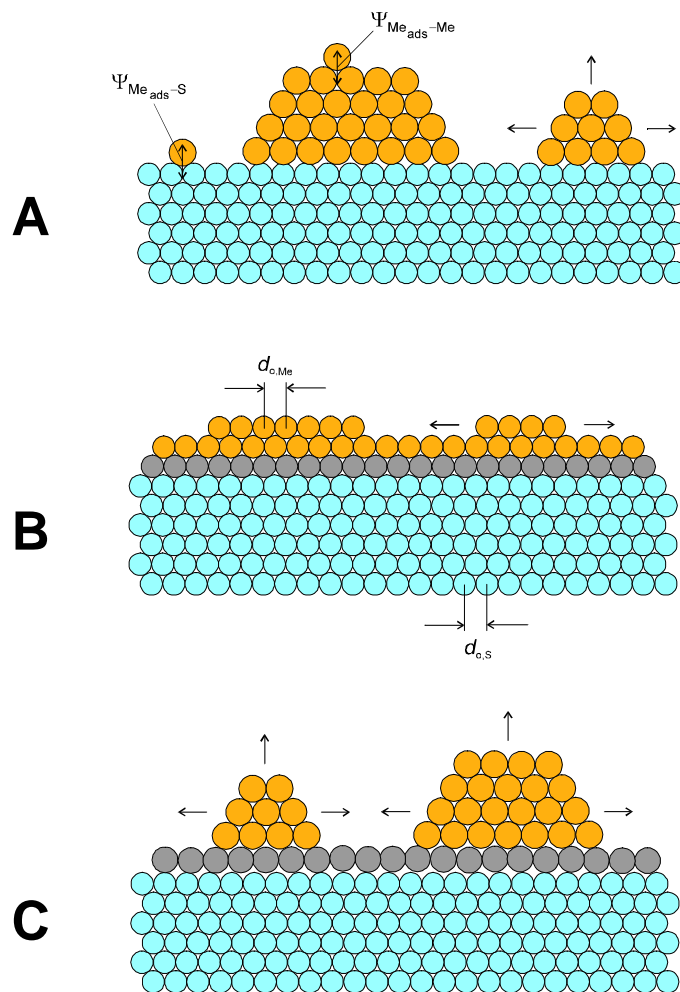
Figure 5.18: Schematic representation of the metal epitaxial growth modes on a foreign substrate: (A) Volmer-Weber ;(B) Frank-van der Merwe and (C) Stranski-Krastanov [3].

surface - C1/A1 associated with 0.25 ML of Ag in aqueous and C3/A3 associated with 0.6 ML in IL suggesting the formation of a more open adlayer of Ag. The value in aqueous is smaller than those published in previous works [129, 130, 137, 138]. There are ,however, some inconsistencies in the reported coverage of Ag in the first UPD in sulfuric acid solutions. For instance, Itaya [129] and Mrozek [137] have derived the coverage from coulometry in the range of 0.31-0.34 ML. In contrast, Kolb [130] and Gewirth [138] have employed charge measurements and have shown that the surface coverage of Ag in the same potential range is about 0.45 ML. These discrepancies can be due to very slow surface alloying kinetics and hence the polarization times used for dissolution may not be long enough to take into account the full amount of the deposited Ag. Surface alloying is supported by two facts: (1) two maxima separated by 11 mV in the stripping LSV measurements indicate that the Ag adatoms occupy two different energetically favored sites on/in the Au(111) surface and (2) a number of monoatomically deep holes are evidenced by in-situ STM imaging in both electrolytes after the dissolution of the Ag adlayer.

Concerning the STM images in aqueous electrolyte, our findings are in good agreement with those of Gewirth et al. [138], who have found by atomic force microscopy(AFM) a (3 x 3) structure at 420 mV. The same structure has been deduced from low-energy electron diffraction (LEED) measurements by Mrozek et al., but in fluoride ion media [137]. In contrast, a $(\sqrt{3} \text{ x } \sqrt{3})$R30° packing has been inferred by Itaya [129] in a broad potential region from 500 to 200 mV. Similarly, Kolb has claimed that the $(\sqrt{3} \text{ x } \sqrt{3})$R30° structure coexists with the (3 x 3) one at 500 mV [130]. However, the (3 x 3) superlattice corresponds to a packing density of 0.44 ML which is substantially higher than the charge-derived coverage of this work. One possible explanation is that the surface alloyed Ag phase can not be completely dissolved during the anodic sweep with 1 mVs^{-1} and therefore the charge derived measurements were underestimated.

As mentioned before, the properties of the electrolyte phase strongly affect the structure of the substrate/electrolyte interface. It is well known that UPD of metals can be accompanied by a specific anion adsorption [139].

In sulfuric solutions, although sulfate/bisulfate is less specifically adsorbed ,for instance, than the halides, it is shown that chemisorption of these species occur in the potential range from 600 mV to 1200 mV, see the review of Magnussen [140]. This means that the first UPD of Ag (C1/A1 peak) is separated by 100 mV and the ectrodeposition of Ag is not influenced by anion adsorption. In contrast, in the BMICl-AlCl$_3$ electrolyte, by high-resolution in-situ STM imaging we have evidenced ordered adlayer of adsorbed AlCl$_4^-$ species. The first indication of such chemisorption was reported by Stafford et al. who have shown by STM an adsorption of tetrachloroaluminate species in acidic aluminium chloride/1-methyl-3-ethylimidazolium chloride on Cu(111) [141]. Similar to this study it is thought that AlCl$_4^-$ species are chemisorbed with the tetrahedral face adjacent to the Au(111). As manifested by CV, the adsorption of AlCl$_4^-$ (C3 process) overlaps with the initial stages of Ag UPD (C4 procees) resulting in a formation of non-uniform adlayer. Besides that, specifically adsorbed AlCl$_4^-$ species affect the UPD potential of Ag by shifting it in the negative direction [142]. In sulfuric electrolyte it occurs at 520 mV (C1) whereas in BMICl-AlCl$_3$ at 430 mV (C3).

The main result of this comparative study are summarized here:

(a) In the aqueous solution, the first UPD process of Ag occurs at 520 mV resulting in an expanded homogeneous (3 x 3) adlayer of Ag whereas the second one at 25 mV shows a transition from a more open (3 x 3) structure to a close packed (1 x 1) monolayer.

(b) In the ionic electrolyte, the first UPD process of Ag exhibits two CV peaks at 410 mV and 230 mV and it is characterized by a charge density of 130 μCcm^{-2} (0.59 ML). Atomically resolved STM images in this potential range show for the first time a structural transition from an inhomogeneous to an ordered phase (disorder/order transition) with a ($\sqrt{3}$ x $\sqrt{3}$)R30° structure and adsorbed AlCl$_4^-$ anions with a superlattice of (1.63 x $\sqrt{3}$) R30° preceding the first UPD of Ag. The second UPD process of Ag arises at 120 mV and 106 mV yielding one ML of Ag.

(c) In both electrolytes, formation of one ML of Ag was found in the UPD

range. The dissolution of Ag adlayer leads to monoatomically deep characteristic holes or pits in the gold substrate which is a signature of 2D surface alloying.

5.3.2 Monte Carlo simulations of adsorption isotherms

The study of UPD of metal atoms belongs to the group of adsorption studies. Adsorption and two-dimensional(2D) phase transitions at surfaces are well suited for lattice-gas modelling. In this section, we focus on equilibrium Monte Carlo (MC) simulations of a lattice-gas model of Ag adsorption on Au(111). For details about this method, see Chapter 2.4. In the previous section, we emphasized how important the interaction energy is between adsorbate and substrate for the growth mechanism. On the other hand, the adsorbate-adsorbate interaction energy play a crucial role for 2D phase transitions. In order to extract this information from experimental measured isotherms, equilibrium Monte Carlo simulations of lattice-gas model of Ag on Au(111) were carried out. Therefore, we employed MC method with one component grand-canonical lattice-gas Hamiltonian including the first, J1, and the second, J2, nearest neighbor pair interactions. For this adsorption study, a computer code (see Appendix 7) was implemented based on a grand-canonical ensemble (or $\overline{\mu}$, V, T ensemble). In this ensemble, the temperature, volume(in this 2D case-surface) and electrochemical potential are kept constant. We have to know only the temperature and electrochemical potential to determine the equilibrium surface coverage of Ag adatoms. The number of Ag adatoms is allowed to fluctuate during simulation. The driving force for the Ag adsorption, the electrochemical potential, $\overline{\mu}$, which is related to the electrode potential, E, was varied. MC simulations used to obtain adsorption isotherms at room temperature (kT=25.7 meV) were performed on hexagonal lattices of size L=20 sites, using Metropolis algorithm based on a random generator, ran2, from Numerical recipes in C, C++ [143]. Each data point was obtained from a run of 5x10^3 Monte Carlo steps per site (MCSS) starting from appropriate ground-state configuration. Sampling was performed at intervals of 2 MCSS, and the first 1000 MCSS were discarded to ensure
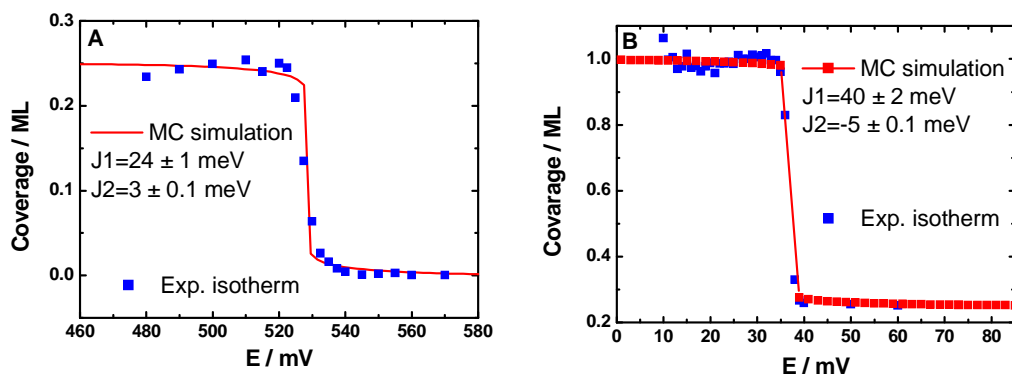
Figure 5.19: (A) Experimental (blue) and simulated (red) isotherms for the first UPD of Ag on Au(111) (C1/A1-process) in aqueous electrolyte ;(B) experimental (blue) and simulated (red) isotherms for the second UPD of Ag (C3/A3-process).

equilibration. The lattice-gas effective interaction energies, J1 and J2, were varied until the simulated isotherms were in acceptable agreement with the experimentally observed ones.

Figure 5.19 shows comparison of a MC simulated isotherm at T=293°C for the first (C1) and the second (C3) UPD of Ag in aqueous solution with the experimental charge derived isotherms. In aqueous solutions, the effective energy of interaction between the 1st nearest neighbor Ag adatoms, J1, obtained from fits of experimantal data for the fisrt and the second UPD processes at T=293°C are J1=24 $\pm$ 1 meV and J1=40 $\pm$ 2 meV, respectively. Three aspects of these interactions energies are particularly interesting. First, the effective nearest neighbor interaction energy is positive denoting effective attraction. Second, J1 for the UPD process which take place at 25 mV (C3), see Figure 5.19B, is relatively strong leading to a discontinuous drop in the isotherm and sharp CV (C3/A3) peaks. This is consistent with the short Ag-Ag bond-length in the dense packed (1 x 1) structure. Third, J1 for the first UPD of Ag at 520 mV, see Figure 5.19A is moderately weak resulting in some kind of "continuous" isotherm. The interaction energy of Ag-Ag in the opened (3 x 3) structure is much more weaker than the interaction energy between Ag adatoms in (1 x 1) structure.

Surprisingly, the situation in ionic electrolyte is different. The effective

interaction between Ag-Ag adatoms obtained from fits with experimental isotherm was found to be moderately repulsive, J1= -10 meV. The simulated isotherm exhibits continuous characteristics and matches very well with the experimental isotherm, see Figure 5.20. A snapshot of the equilibrium Monte Carlo simulation at E=350 mV reveals some ordered patches of Ag adatoms and some domains of disordered Ag phase. By performing MC simulations for different electrode potentials in the range from 400 mV to 200 mV, the snapshots show that the ordered phase of Ag becomes predominant and the disordered phase disappears. This result is in very good agreement with in-situ STM images obtained at these potentials, compare the snapshot presented in Figure 5.20B with in-situ STM image shown in Figure 5.21. In the snapshot of MC simulation at 350 mV, blue circles represent Ag adatoms on the surface whereas white ones unoccupied sites.

The disordered Ag phase might be a result of adsorption of $AlCl_4^-$ ions which precedes and overlaps with the deposition of Ag. Thus, the transition into ordered phase would involve a desorption and replacement of $AlCl_4^-$ ions with Ag densely packed atoms. In order to simulate this scenario, a more realistic model is needed including a usage of a two component lattice-gas Hamiltonian which will take into account the adsorption of $AlCl_4^-$ as well.
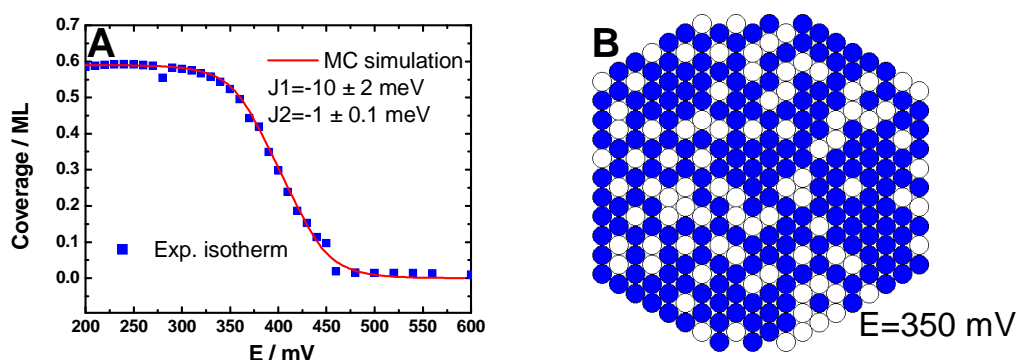
Figure 5.20: (A) Comparison of a MC simulated isotherm in $BMICl-AlCl_3$ with the experimental charge derived isotherm ;(B) Snapshot of MC simulation at E=350 mV which shows ordered patches of Ag adatoms in very good agreement with in-situ STM images; blue circles represent Ag adatoms on the surface, whereas white ones unoccupied sites.
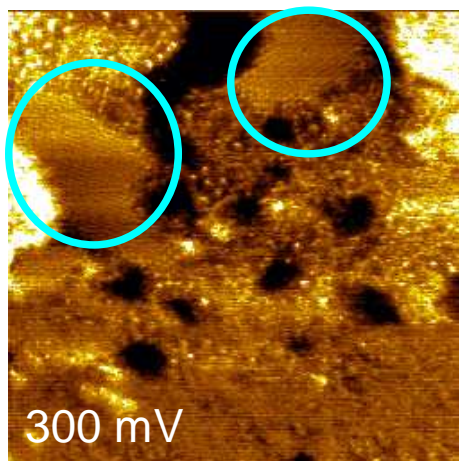
Figure 5.21: In-situ STM image at 300 mV shows characteristic domains of the ordered Ag phase which corresponds very good to the snapshot of the MC simulation.

Chapter 6

Potential pulsed nanostructuring of Ag on Au(111) in the UPD region

6.1 Introduction

In general, electrodeposition of a metal on an electrode surface in the under potential deposition(UPD) region can be performed under conditions of constant electrode potential where a smooth monoatomically thin two-dimensional(2D) electrodeposit is obtained. Another technique involves applying to the electrode a potential on a very short time scale. Pulsed potential overpotential deposition(OPD) is a well established method which causes the formation of three-dimentional(3D) nanoscopic metal particles. Various systems have been investigated with respect to the influence of duration and magnitude of potentiostatic pulsing on size and spacial distribution of metal clusters, see reviews [144, 145, 146]. Most of these studies use squared wave potential pulses in the OPD region and substrates that have large crystallografic mismatch with the deposited metal as well as low interfacial energy such as graphite [147, 148]. This leads to electrodeposition of 3D metal particles under conditions of instantaneous nucleation and diffusion-controlled Volmer-Weber growth mode. However, there is lack of investigations that

99

focus on potential pulsing in the UPD range, in particular on high energy surfaces (e.g., noble metals) where usually homogeneous monolayer formation is expected by gradually changing the electrode potential. Therefore, the aim in this work was to check how the electrochemical stability, behavior, and topography of a metal monolayer will be affected by applying one potential pulse in the UPD range of that metal on high energy surfaces such as Au(111). Silver was selected because the reduction of Ag^+ exhibits fast heterogeneous electron transfer kinetics and because previously we have studied the electrodeposition in UPD range of Ag on Au(111) (see Sec. 5.1).

6.2 Results

Pulsed electrodeposition in the UPD region of Ag on Au(111) from sulfuric aqueous electrolyte was carried out by switching the electrode potential from E1=550 mV to E2=20 mV vs. Ag^+/Ag for very short time, see Figure 6.1A. Duration of potential pulse was varied from 0.2 ms to 500 ms. For these fast measurements, the potentiostat was equipped with a special interface card, ADC750 (AutoLab, Nederlands), which has a maximum conversion speed of 750 kHz and can measure current-time response with a shortest interval of 1.3 μs. After one potential pulse from E1=550 mV to E2=20 mV the electrochemical cell was switched off and STM experiment was performed at open circuit potential(OCP).

6.2.1 Potential pulsed electrodeposition of 2D Ag clusters

After one potential pulse from 550 mV to 20 mV in 1 mM solution of Ag^+ on Au(111) with a duration of 0.2 ms, the gold surface was examined by in-situ STM at OCP. The measured OCP was stabilized at 70 mV. Figure 6.2A presents an STM image of the surface showing a surprisingly large number of two-dimensional(2D) silver nano clusters. Their spacial distribution and size will be discussed in Sec. 6.3.1. Apparently, the clusters have a narrow
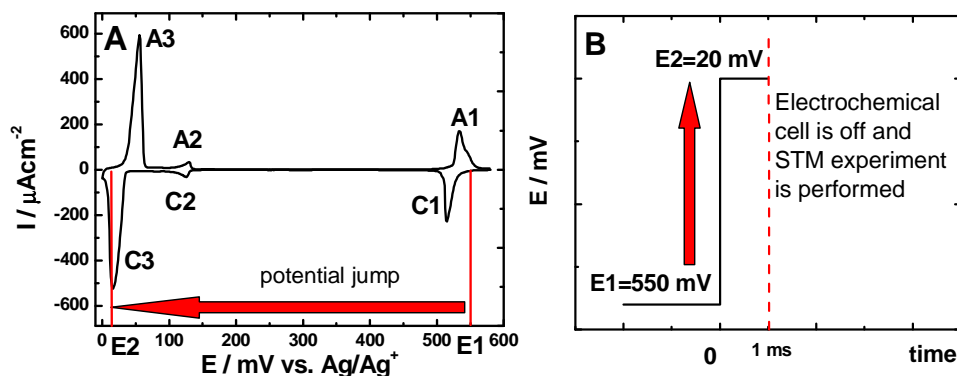
Figure 6.1: (A) Cyclic voltammogram recorded on single crystal Au(111) in 1 mM Ag_2SO_4 + 0.1M H_2SO_4 at a sweep rate of 30 mVs^{-1}; The red arrow shows a potential jump ;(B) After one potential pulse from E1=550 mV to E2=20 mV the electrochemical cell is switched off and STM experiment is performed.

size distribution suggesting instantaneous nucleation.

A detailed analysis of the STM images reveals that the 2D Ag nanoclusters are formed all over the surface without any preferential position on the gold terraces or at the step edges. Also, it was found that they have a very high stability because no significant change in their size and spacial distribution was observed for a long span of time, see Figure 6.2B. A cross section analysis (Figure 6.2B) reveals silver clusters which have a monoatomic height of 2 Å. In order to prove whether 2D Ag clusters can grow under potentiostatic conditions, the electrochemical cell was switched on and the electrode potential was gradually reduced from 70 mV (the actual value of OCP) to 0 mV. From OCP to 30 mV there is no significant change on the surface (Figure 6.3A). In accordance with the CV, at 20 mV, a new silver phase is being formed at the step edges and at 2D silver clusters as well, see Figure 6.3B. The development of the island growth was continuously followed at constant applied electrode potential of 20 mV. In Figure 6.3B-D sequential images are shown with a time interval of about 5 minutes. The new Ag islands enlarge relatively fast their size and indicate a strong tendency to merge with each other as well as with the existing Ag clusters. Apparently, the silver islands that stem from the pulsed clusters, grow with different rates. Approaching the Nernst
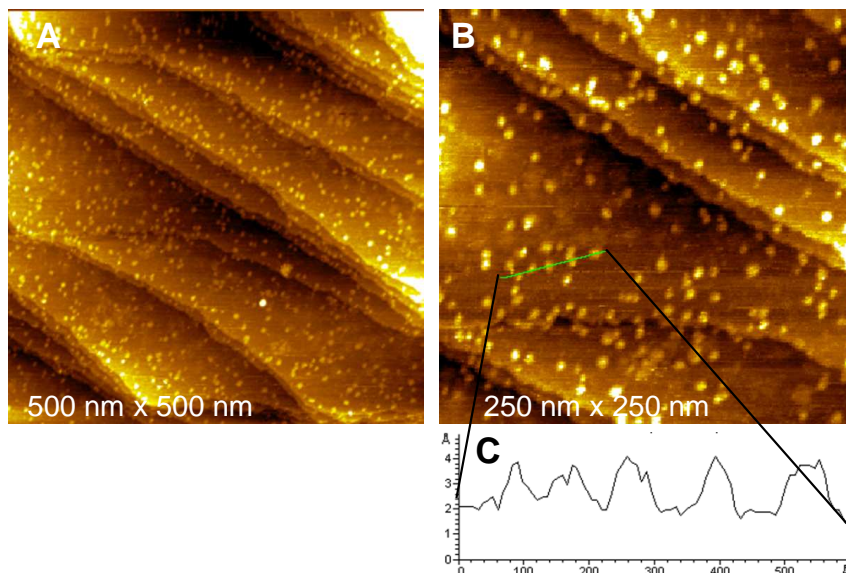
Figure 6.2: (A) 500 nm x 500 nm in-situ STM image of Au(111) after one potential pulse from 550 mV to 20 mV with a duration of 0.2 ms in 1 mM Ag_2SO_4 + 0.1M H_2SO_4 ;(B) 250 mn x 250 nm area of the substrate recorded at OCP after 24h ;(C) Cross section analysis of 2D Ag clusters yielding a height of 2 Å.

equilibrium potential, the surface coverage of Ag on Au(111) increases. It is worth noting that almost one monolayer of Ag coverage is reached at 0 mV and the pulsed clusters become almost an unrecognizable part of it (Figure 6.3F). Thus, conclusion can be drawn that the pulsed Ag clusters belong to the redox couple C3/A3, see Figure 6.1A. Interestingly, it seems that before the monolayer of Ag covers the whole surface, some islands are formed on the top of the silver monolayer, perhaps, due to the fact that the electrodeposition is governed at or near non-equilibrium conditions. A pseudomorphic (1 x 1) adlayer of Ag is formed that covers and follows the topography of the Au(111) surface. This result is in good agreement with our charge measurements.

Dissolution of the deposited monolayer of Ag was studied by in-situ STM as a function of the applied electrode potential. In Figure 6.4A-D STM snapshots are displayed during the dissolution process.
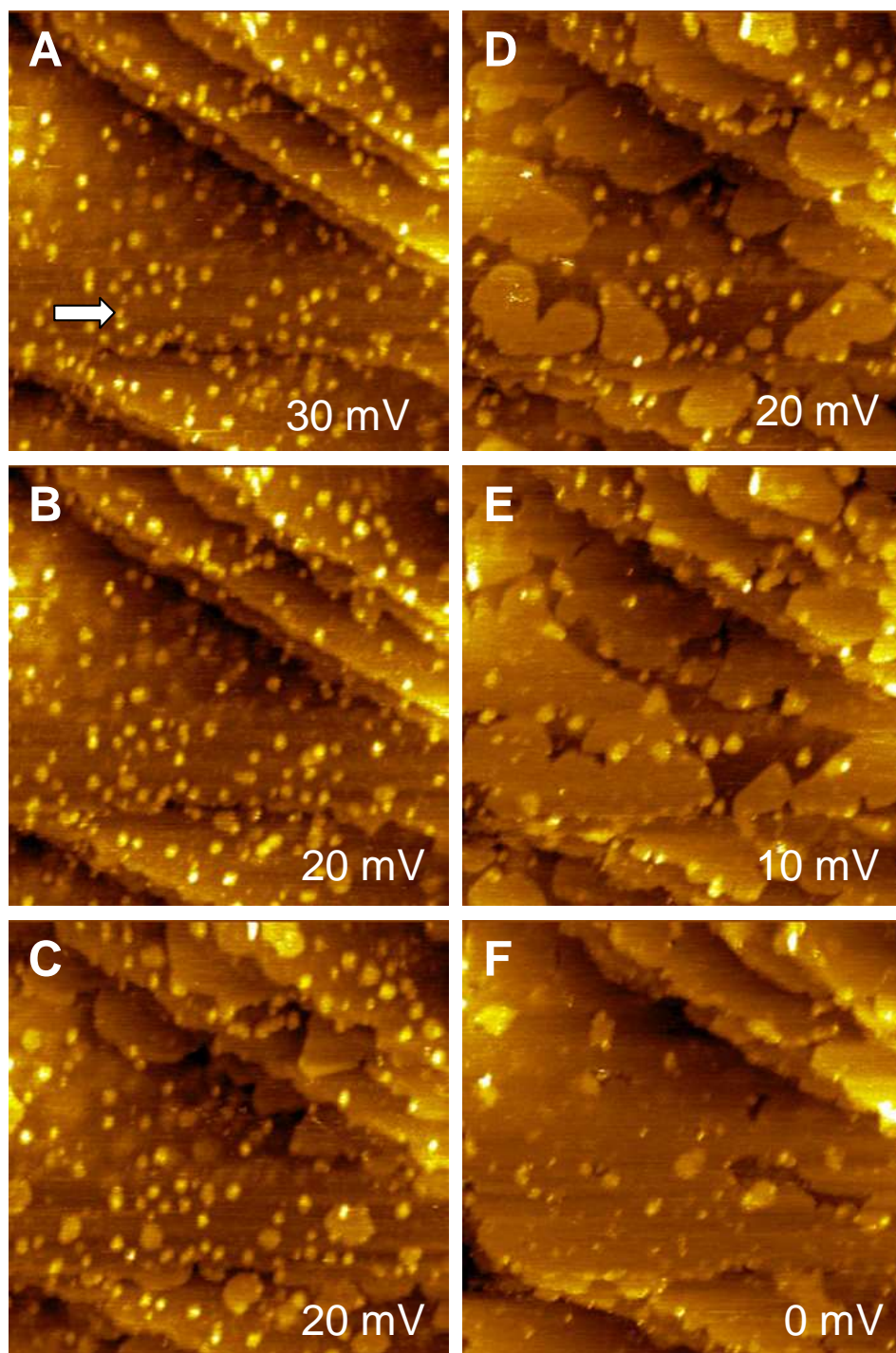
Figure 6.3: A sequence of in-situ STM images after 0.2 ms potential pulse from 550 mV to 20 mV at various electrode potentials showing a formation of one monolayer of (1 x 1)-Ag, size 250 nm x 250 nm ;(A) at 30 mV ;(B)-(D) at 20 mV ;(E) at 10 mV ;(F) at 0 mV.

It should be noted that although the 2D Ag clusters become a part of the (1 x 1) Ag monolayer, they can not be stripped at more positive potentials where usually the (1 x 1)-Ag adlayer is completely dissolved in accordance with the CV (A3 process in the CV). This strongly indicates that the 2D clusters exhibit an anomalously stability.
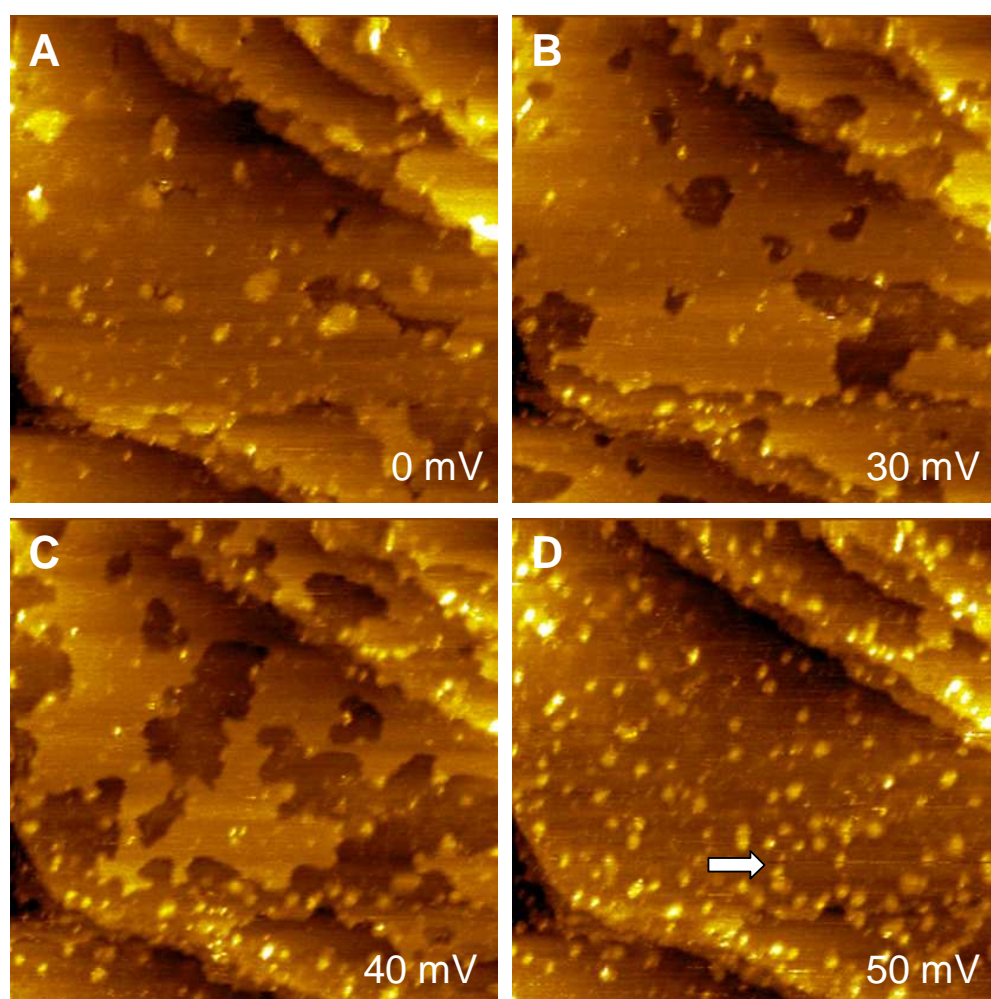
Figure 6.4: A sequence of STM images showing the dissolution of the (1 x 1)-Ag adlayer; size 250 nm x 250 nm (A) at 0 mV ;(B) at 30 mV ;(C) at 40 mV ;(D) at 50 mV. The white arrow shows that after dissolution the same 2D pulsed Ag clusters appear on the surface as before indicating a very high stability.

Moreover, a striking result is, that some kind of "memory effect" is observed because after dissolution the STM pictures reveal the 2D Ag clusters at the same places on the surface as at the beginning of the deposition, see the white arrows in Figure 6.4D and Figure 6.3A. The 2D Ag clusters are evidenced even at 200 mV as displayed in Figure 6.5B. They start to dissolve slowly in the potential range from 200 mV to 400 mV, see Figure 6.4B-D.
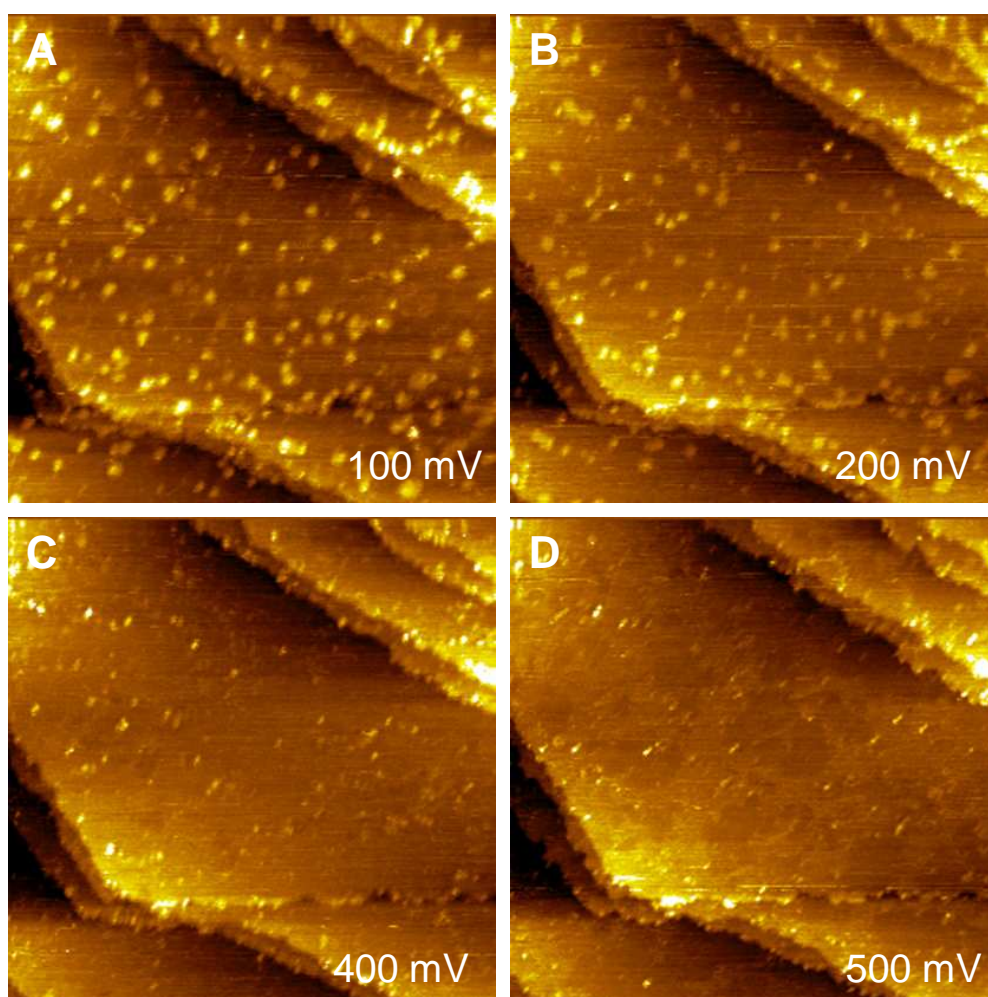
Figure 6.5: STM images (250 nm x 250 nm) of dissolution of 2D pulsed Ag nanoclusters. (A) at 100 mV there is no change ;(B) at 200 mV the clusters slowly start to dissolve ;(C) at 400 mV and ;(D) at 500 mV are almost completely dissolved.

A dependence of duration of the potential pulse on the Ag clusters size is presented in Figure 6.6. Analysis of these images leads to the conclusion that the duration of pulsing strongly affects the surface density of Ag clusters and their size. By comparing Figure 6.6A with Figure 6.6D one can say that increasing the duration of the potential pulse results in larger clustering. The nucleation density after a 0.2 ms pulse is higher than for a 500 ms pulse.
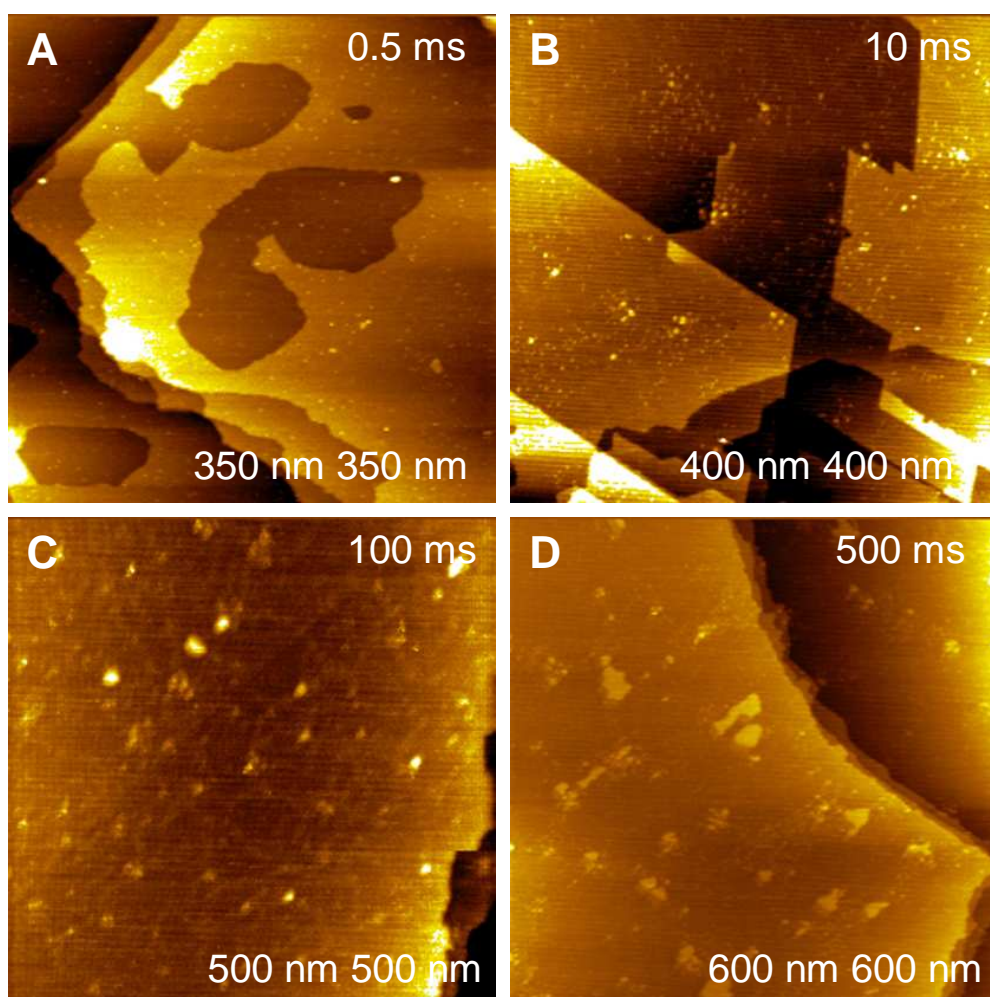
Figure 6.6: STM images after potential pulse from 550 mV to 20 mV with different duration. The dependence of pulse duration on cluster size is clearly visible. (A) with 0.5 ms ;(B) 10 ms ;(C) 100 ms ;(D) 500 ms.

6.3 Discussion

6.3.1 Spacial distribution of clusters

Pulsed silver electrodeposition, monitored by in-situ STM in the UPD range on Au(111) was carried out for the first time. The results have shown that by applying short potential pulses a number of 2D nano clusters can be formed. In order to analyze how the 2D Ag clusters are distributed on the surface the distances between first nearest neighbors were derived from the STM image (Figure 6.2A). In general, the formula for the probability distribution of the distances between first nearest neighbors of randomly distributed clusters on a flat 2D surface is

$$\frac{dP}{dr} = 2\pi r N \exp\left(-\pi N r^2\right),\tag{6.1}$$

where $dP(r)$ and N are the probability distribution function and the average cluster density, respectively. Details of stochastic properties of assemblies of objects randomly distributed in space can be found in [149]. The location of any Ag cluster in the STM image after a potential pulse of 0.2 ms (Figure 6.2A) was digitized with respect to an arbitrary origin and the experimental histogram of distribution of distances between first neighbors was calculated by a special program written for that purpose. The program does not take into account clusters that are at the edges of the STM picture and thus reduces finite-size effects. The average cluster density, in this case, was found to be N=0.00383 nm^{-2} or 3.8 x 10^{11} cm^{-2}. This number density is surprisingly two orders of magnitude higher than the reported values of Penner [150] who used a 10 ms pulse in 1 mM Ag^{+} plating solutions in the OPD range on graphite substrates to produce 3D nanoclusters. Figure 6.7 demonstrates the correlation between the theoretical and experimental distributions of the distances between nearest neighbors in case of 2D Ag pulsed electrodeposited clusters on a flat Au(111) surface. As is seen from Figure 6.7 part of the smallest distances in the range from 0 to 5 nm predicted by the theory are missing from the experimental histogram. This result is due to the finite size

of clusters that have an average size of 5 nm. In addition, the experimental histogram is narrower than the theoretical one. This might be explained in terms of "screening zones" of reduced surface concentration spreading around growing silver nanoclusters and creating unfavorable nucleation conditions. From the experimental data, the mean first nearest neighbor distance is determined to be 9.7 ± 1.75 nm whereas the theoretical value according to Eq. 6.1 is 8.1 nm [149].
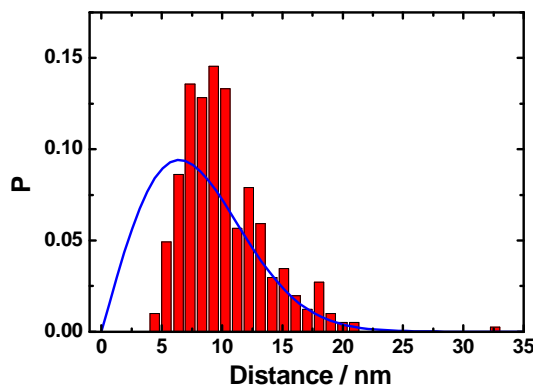
Figure 6.7: Histogram of distances between nearest neighboring Ag clusters after using a 0.2 ms potential pulse, for STM image, see Figure 6.2A. The line is drawn according to Eq. 6.1.

6.3.2 Coupled diffusion-adsorption model

In the previous chapter 6.2.1 STM images demonstrated that by applying short potential pulse 2D Ag nanoclusters with unusual properties can be formed. During the potential pulse, the current-time response of the electrochemical system was recorded, see Figure 6.8. In the following discussion we focus on an adequate kinetic model by which one can not only describe the $i - t$ characteristics but also get some insight into the physics of 2D potential pulsed Ag electrocrystallization.
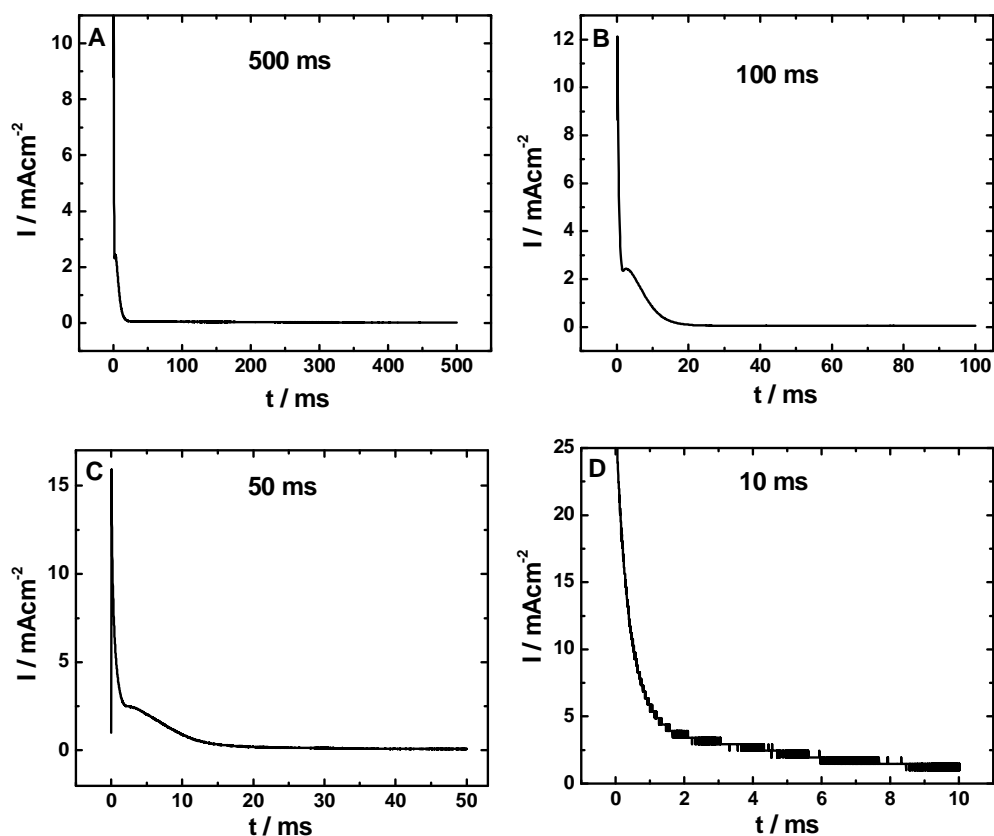
Figure 6.8: Current-time responses recorded during the potential pulse from 550 mv to 20 mV in 1 mM Ag_2SO_4 + 0.1M H_2SO_4 on Au(111).

In general, electrocrystallization is a complex process which involves a number of distinct steps:

(1) diffusion and electromigration of ions in solution to the electrode surface,

(2) electron transfer,

(3) adsorption on the surface with partial or complete loss of the solvation sheath, resulting in the formation of adatoms,

(4) surface diffusion and lattice incorporation of adatoms.

Evaluating the current-time transients according to the existing models [151] for 2D nucleation it became evident that standard nucleation models fail to describe the $i - t$ transients. For instance, Langmuir type of adsorption predicts an exponential decaying function of i vs. t which can not describe the shoulder in $i-t$ transients, see Figure 6.8C. On the other hand, combining the current for double layer charging, i_{DL},

$$i_{DL} = i_0 \exp(-\frac{t}{\tau}), \qquad (6.2)$$

and the well-known expression for current, i_{2DLI}, of 2D instantaneous nucleation [151] if the rate determining step is the lattice incorporation of Ag adatoms at the expanding periphery of the nucleation centers, i_{2DLI},

$$i_{2DLI} = \frac{2\pi FMhN_0k^2}{\rho}t \exp\left(-\frac{\pi N_0 M^2 k^2}{\rho^2}t^2\right), \qquad (6.3)$$

one yields,

$$i(t) = i_{DL}(t) + i_{2DLI}(t). \qquad (6.4)$$

Here F is the Faraday number, N_0 is the number of nuclei present at $t = 0$, k is the rate of lattice incorporation expressed in $molcm^{-2}s^{-1}$, h is the height of the monolayer, and M and ρ are the atomic weight of Ag and density of the adlayer, respectively.

If the experimental $i-t$ data are plotted according to Eq. 6.4 in coordinates[1] $\ln\left(\frac{i-i_0\exp^{-\frac{t}{\tau}}}{t}\right)$ vs. t^2 one should obtain a straight line. However, the $i - t$ transients for 50 ms pulse strongly deviates from the well known model as plotted in Figure 6.9.

Therefore, in order to gain a fundamental understanding of the kinetics during pulsing, it was necessary to develop a theoretical model which describes the early stages of eletrocrystalization, namely processes (1), (2) and (3), see Figure 6.10. The process (2) can be neglected because the charge transfer reaction ($Ag^+ + e^- = Ag^0$) is one of the fastest electrochemical reaction (exchange current density of Ag is I_{ex}=20 A/cm^2).

---

[1]i_0 and τ are obtained from fits of Eq. 6.2 to the initial parts of the $i - t$ curve for 50 ms pulse
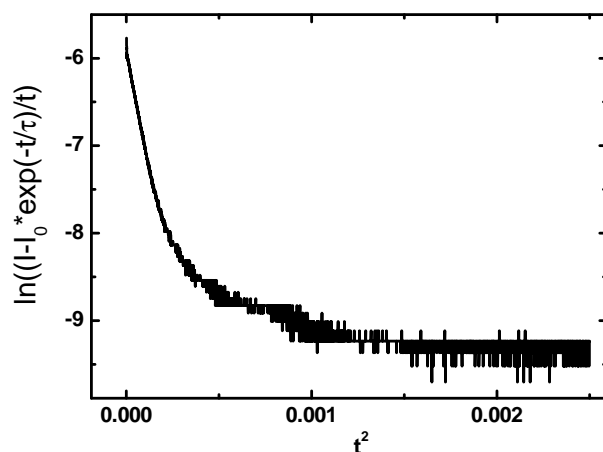
Figure 6.9: Current-time transient plotted in $\ln\left(\frac{i - i_0 \exp^{-\frac{t}{\tau}}}{t}\right)$ vs. t^2 coordinates shows not linearized behavior according to Eq. 6.4.
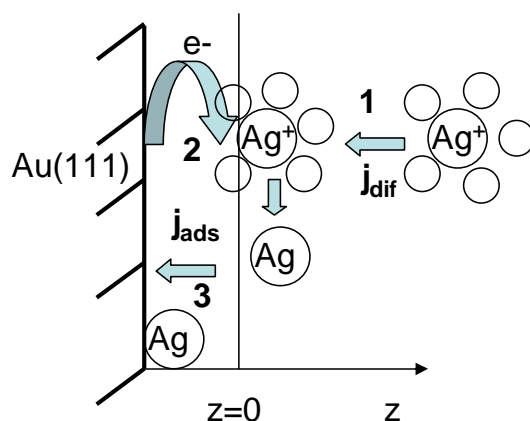
Figure 6.10: Initial stages of electrocrystallization: **1**. diffusion and electromigration **2**. charge transfer (exchange current density of Ag is I_{ex}=20 A/cm^{-2}) **3**. adsorption.

In general, the transport of Ag+ ions in the bulk is driven by both diffusion and electromigration. However, in the present case the latter is negligible due to the high electrolyte concentration of supporting electrolyte (0.5M H$_2$SO$_4$).

Thus, the evolution of the local concentration c(z,t) of Ag^+ ions in the solution obeys the regular diffusion equation,

$$\frac{\partial c(t,z)}{\partial t} = D\frac{\partial^2 c(t,z)}{\partial z^2},\qquad(6.5)$$

where D is the corresponding diffusion coefficient. The boundary conditions of Eq. 6.5 are constant concentration, $c_\infty = c(t, z = \infty)$, far away from the Au electrode and the balance of the diffusion and adsorption fluxes $D(\partial_z c)_{z=0} = \partial_t \Gamma^2$ on the Au surface, where Γ is the adsorption of Ag atoms. The initial conditions are constant concentration everywhere in the bulk $c(t = 0, z) = c_\infty$ and a bare Au surface $\Gamma(t = 0) = 0$ at the beginning of the process. Hence, the solution of Eq. 6.5 is the following Laplace image $\tilde{c}(s, z)$ of the local concentration

$$\tilde{c} = c_\infty/s - \tilde{\Gamma}\sqrt{s/D}\exp(-\sqrt{s/D}z),\qquad(6.6)$$

Further analysis requires modeling of the adsorption kinetics. From the experimental CV it is clear that the Ag atoms can form two different stable surface phases on the Au surface: the (3 x 3) phase occurring at 520 mV and the (1 x 1) at 20 mV, for details, see chapter 5.2. Let us denote the dilute one as phase α and the condensed one as phase β. If the electrode potential changes continuously the α-phase appears at about 520 mV and then it is transformed in the β-phase at around 20 mV. However, if the potential jumps from 550 mV directly to 20 mV there is no α-phase at the beginning and, hence, the formation of the two phases will take place simultaneously. Obviously, the creation of the β-phase requires first the presence of the α-phase. Thus, a linearized kinetic model of the adsorption of Ag on Au electrode after the potential jump reads:

$$\partial_t \Gamma_\alpha = k_a c_s(t)(\Gamma_\alpha^\infty - \Gamma_\alpha) \approx k_a \Gamma_\alpha^\infty c_s - k_a c_\infty \Gamma_\alpha,\qquad(6.7)$$

$$\partial_t \Gamma_\beta = k_t \Gamma_\alpha c_s(t)(\Gamma_\beta^\infty - \Gamma_\beta) \approx k_t c_\infty \Gamma_\beta^\infty \Gamma_\alpha - k_t c_\infty \Gamma_\alpha^\infty \Gamma_\beta,\qquad(6.8)$$

where Γ_α and Γ_β are the surface coverages of the α- and β-phases, respec-

---
$^2\partial_z$ stands for $\partial/\partial z$

tively, $c_s = c(t, z = 0)$ is the surface concentration, k_a is the adsorption constant, and k_t is the rate constant of transformation of α into β phase. Note, that the desorption is completely neglected in Eqs. 6.7 and 6.8. Solving these equations by Laplace transformation yields the following Laplace images of the adsorptions

$$\tilde{\Gamma}_\alpha = k_a \Gamma_\alpha^\infty \tilde{c}_s / (s + k_a c_\infty), \tag{6.9}$$

$$\tilde{\Gamma}_\beta = k_t c_\infty \Gamma_\beta^\infty k_a \Gamma_\alpha^\infty \tilde{c}_s / (s + k_a c_\infty)(s + k_t c_\infty \Gamma_\alpha^\infty) \cdot \tag{6.10}$$

The total adsorption of Ag atoms on the Au surface is a sum of the partial adsorptions above, i.e.

$$\tilde{\Gamma} = \tilde{\Gamma}_\alpha + \tilde{\Gamma}_\beta = k_a \Gamma_\alpha^\infty \tilde{c}_s \frac{s + k_t c_\infty (\Gamma_\alpha^\infty + \Gamma_\beta^\infty)}{(s + k_a c_\infty)(s + k_t c_\infty \Gamma_\alpha^\infty)}. \tag{6.11}$$

Introducing Eq. 6.11 in Eq. 6.6 leads to an expression for the Laplace image of the local concentration. Using it one can derive the Laplace image of the surface concentration in the form

$$\tilde{c}_s = c_\infty \frac{(s + k_a c_\infty)(s + k_t c_\infty \Gamma_\alpha^\infty)}{s[(s + k_a c_\infty)(s + k_t c_\infty \Gamma_\alpha^\infty) + k_a \Gamma_\alpha^\infty (s + k_t c_\infty \Gamma_\alpha^\infty + k_t c_\infty \Gamma_\beta^\infty)\sqrt{s/D}]} \tag{6.12}$$

which depends both on the diffusion in the bulk and the kinetics of adsorption. Finally, the measured electric current is a sum of the electric current due to Ag deposition and the current due to the charging of the electric double layer

$$\tilde{i} = Fs\tilde{\Gamma} + A/(s + k_r). \tag{6.13}$$

Here F is the Faraday number, A is a constant and k_r is the relaxation constant of the double layer formation. Substituting $\tilde{c}_0$ from Eq. 6.12 and 6.11 and introducing the result of $\tilde{\Gamma}$ in Eq. 6.13 leads to the following expression for the Laplace image of the current

$$\tilde{i} = \frac{Fk_a c_\infty \Gamma_\alpha^\infty (s + k_t c_\infty \Gamma_\alpha^\infty + k_t c_\infty \Gamma_\beta^\infty)}{(s + k_a c_\infty)(s + k_t c_\infty \Gamma_\alpha^\infty) + k_a \Gamma_\alpha^\infty (s + k_t c_\infty \Gamma_\alpha^\infty + k_t c_\infty \Gamma_\beta^\infty)\sqrt{s/D}} + \frac{i_0 - Fk_a c_\infty \Gamma_\alpha^\infty}{s + k_r}, \tag{6.14}$$

where the constant A was expressed by the initial current $i_0 = i(t = 0)$. The analytical inversion of the Laplace image from Eq. 6.14 is impossible. For this reason numerical calculations are employed. Some of the parameters in Eq. 6.14 are known: c_∞=1 mM and D=1.65x10^{-5} cm^2/s [152]. From our previous investigation, see chapter 5.2.1, we concluded that the α-phase corresponds to 0.25 ML, while the condensed phase (β-phase) forms a complete monolayer. Thus, one can estimate that the maximal adsorptions equal to $\Gamma_\alpha^\infty = 0.25/(N_A \pi d^2) = 1.6$ μmol/m^2 and $\Gamma_\beta^\infty = 0.75/(N_A \pi d^2) = 4.8$ μmol/m^2, where $d = 2.89$ is the distance between the surface Au atoms. Because of the high electrolyte concentration the relaxation of the double layer is very fast of the order of 1 ms. Hence, the corresponding relaxation can be obtained from the initial slope of the current transient for a 10 ms pulse, presented in Figure 6.10D, i.e. $k_r^{-1} = 0.2$ ms. For the initial current we adopt the value of i$_0$ = 16 mA/cm^2 in accordance with Figure 6.10C. The remaining other two parameters are determined by a fit of the dependence i vs. t for 50 ms pulse, see Figure 6.8C. For this purpose, the inverse Laplace transformation of Eq. 6.14 was performed numerically and then fitted to the experimental i vs. t for 50 ms pulse data varying the constants k_a and k_t. The best fit corresponds to $k_a c_\infty$=0.1x10^{-3} s^{-1} and $k_t c_\infty \Gamma_\beta^\infty$ =1x10^{-3} s^{-1}. The theoretical dependence of $i - t$ response for a 50 ms potential pulse as calculated from Eq. 6.14 is plotted in Figure 6.11. As is seen the theory reproduces very well the characteristic maximum at about 2 ms after the double layer charging. In Figure 6.12 the time dependence of the surface concentration, $c_s(t)$, and the adsorption of $\alpha-$ and β-phases, respectively, are plotted. Obviously, at the beginning, the dilute phase(α phase) forms, which later completely transforms into condensed one(β). The surface concentration is substantially decreased compared to the bulk one and the slow diffusion kinetics determines the current-time response at larger time.
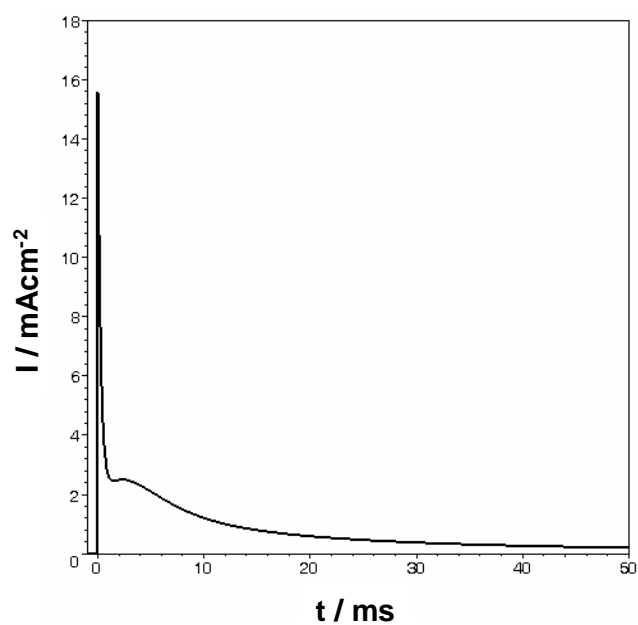
Figure 6.11: The theoretical dependence of current vs. time for a 50 ms potential pulse obtained from the model according to Eq. 6.14
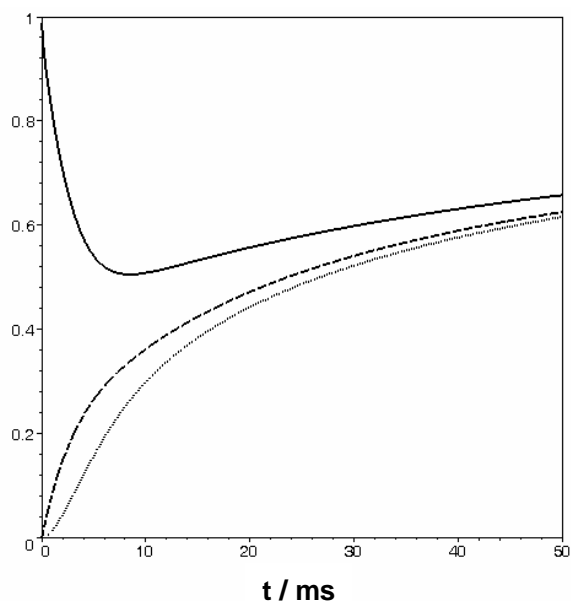
Figure 6.12: Evolution of the relative subsurface concentration, c_s/c_∞ (solid line) and the relative adsorptions $\Gamma_\alpha/\Gamma_\infty^\alpha$ (dashed line) and $\Gamma_\beta/\Gamma_\infty^\beta$ (dotted line).

Chapter 7

Appendix: Monte Carlo code

Monte Carlo simulation code in C\C++.

Monte Carlo code for simulating the underpotential deposition(UPD) of Ag on Au(111) at equilibrium is given as follows:

```c
// Monte Carlo code for simulating adsorption isotherms of
// (3 x 3), (1 x 1) and (Sqrt{3} x Sqrt{3}) structures of Ag
// in the UPD region on Au(111)
#include <iostream.h>
#include <fstream.h>
#include <math.h>
#include <time.h>
#include <stdlib.h>
#include "nr.h"
#include "nrutil.h"

#define NSAMPLES 10 // number of samples taken for each Nmax
#define MSCMAX 5000   // max number of MC steps
#define L 20 // Lattice size
#define pi 3.141592654

char fExportName[]="\\upd.txt";
char fExportLattice[]="\\upd_lat.txt";

float ran2(long *idum);

int lattice[L+1][L+1][3];
```

```cpp
double deltaW2(double J,double mu, int k, int l, int* ipp,
int* imm);
double deltaW3(double J,double mu, int k, int l, int* ipp,
int* imm); //1st neareast neighbor-6 atoms

// 1st nearest neighbours(NN) = 6 atoms; 2nd NN = 6 atoms
double deltaW4NN2(double J1,double J2, double mu, int k,
int l, int* ip, int* im, int* ipp, int* imm);

//this function returns in y, x the coordinates in orthogonal
// coordinate system each paar i,j with a unit lattice with
// angle=60 in (3 x 3) structure and a=b=a;
void Convert_i_jTo_y_x(int i, int j, double *y, double *x,
const double a,const double angle_x,const double angle_y,
const double x0,const double y0);


int main(int argc, char *argv[])
{
 long j,i,iseed, start, end , count, mcs, mcsmax, n0, nb;
 float fRan;
 int *ip, *ipp, *im, *imm;
 double mu,J, J2, k,T, Mi, mi,mi4_av, mi2_av2,mi2_help,samples,
 To, Tstep, Tend ;
 double mu_step, mu_end, mu_export, W; // energy difference;
 double x,y, x_Au, y_Au;

 // the lattice constants of unit cell and the origin of
 // the orthogonal coordinate system

 // for (3 x 3) superlattice
 /*
 const double angle_y=pi/3.0; // 60 grad of y-axis_supperlattice
 // with respect to x_gold lattice(1,-1,0)
 const double angle_x=0.0; // 0 grad x-axis_superlattice
 // matches x_gold lattice(1,-1,0)

 const double x0=3.0/4.0;
 const double y0=sqrt(3.0)/4.0;
 const double a=1.5;
 */




 /*for (1 x 1) superlattice
 const double angle_y=pi/3.0;  // 60 grad of y-axis_supperlattice
 // with respect to x_gold lattice(1,-1,0)
 const double angle_x=0.0; // 0 grad x-axis_superlattice
 // matches x_gold lattice(1,-1,0)

 const double x0=0.0;
 const double y0=0.0;
 const double a=1;
 */

 //for ( sqrt(3) x sqrt(3) ) superlattice
 const double angle_y=pi/6.0; // 30 grad of y-axis_supperlattice
 // with respect to x_gold lattice(1,-1,0)
 const double angle_x=-pi/6.0; // -30 grad x-axis_superlattice
 // with respect to x_gold lattice(1,-1,0)
 const double x0=0.5;
 const double y0=1/(2.0*sqrt(3.0));
 const double a=sqrt(3.0);
```

```cpp
// mu=electrochemical potential
// cumulant mi4_av = <mi^4>; mi2_av2=<mi^2>^2

J=1.0;      // [meV] interaction between 1st NN, known as J1
J2=13.0;    // [meV] interaction between 2nd NN, known as J2
k=1.0;
T=25.7;
To=25.7;    // temperature in unit of kT [meV]
Tstep=1;
Tend=26;


mu=60;      // [meV]
mu_export=70; //export at given mu_export
mu_end=80;
mu_step=1;


n0=1000;// the monte carlo step from which averaging will begin
nb=1;   // after n0 every nb-th configuration will be count
// (nb=2 means every second)
Mi=0.0; //  Magnetization (Adsorption per lattice^2)

mcsmax=MSCMAX;
samples=double(mcsmax-n0+1);
samples=0.0;

ip=ivector(1,L); // gives the index of the next i+1 neighbour
im=ivector(1,L); // gives the index of the next i-1 neighbour
ipp=ivector(1,L); // gives the second i+2
imm=ivector(1,L); // gives the second i-2
mcsmax=MSCMAX;

ofstream fExp, fExpLat;
fExp.open(fExportName);
if(!fExp)
{
cout<<"\n ERROR OPENING FILE ="<<fExportName;
}


 fExp<<"Ising\tL="<<L<<"\tMSCMAX="<<MSCMAX<<"\tT="<<T<<"\tJ="
<<J<<"\tJ2="<<J2<<endl;




 fExp<<"mu\tmi"<<endl;
 time_t now_s;
 struct tm *ptm1;
 time(&now_s);
 ptm1=localtime(&now_s);
 cout<<"\n Start calculating ... at "<<asctime(ptm1)<<endl;
 //iseed=-747;
 iseed=-79;
 start=clock();

for(mu=mu;mu<=mu_end;mu=mu+mu_step)
{

 samples=0.0;
//      W=exp(-2*J*k*(1.0/T)*(double)j);
 // look up table for PERIODIC BOUNDARY CONDITIONS
 for(i=1;i<=L;i++)
 {
     ip[i]=i+1;
     im[i]=i-1;
     ipp[i]=i+2;
     imm[i]=i-2;
 }
```

```cpp
ip[L]=1;
im[1]=L;

imm[1]=L-1;
imm[2]=L;

ipp[L]=2;
ipp[L-1]=1;

// initialize the lattice
for(i=1;i<=L;i++)
{
    for(j=1;j<=L;j++)
    {
        lattice[i][j][0]=0;
        //cout<<"lattice["<<i<<"]["<<j<<"]"<<endl;
    }

}

// Monte Calro part
count=0;
mi=0.0;
mi4_av=0.0;
mi2_av2=0.0;
for(mcs=1;mcs<=mcsmax;mcs++)
{
    // generate one sweep
    for(i=1;i<=L;i++)
    {
        for(j=1;j<=L;j++)
        {

            // compute the energy difference by a function
            // W=deltaW3( J,mu,i, j, ip, im);// take only 1st NN

            W=deltaW4NN2(J,J2,mu,i,j,ip,im,ipp,imm);//take 1st
            and 2nd NN
            W=exp(-1*k*(1.0/T)*W);
            //cout<<"\tH="<<W<<endl;
            fRan=ran2(&iseed);
            //decide to flip ot not
            fRan=ran2(&iseed);

            if(fRan<W)
            {
                //flip the spin
                if(lattice[i][j][0]==0) lattice[i][j][0]=1;
                else lattice[i][j][0]=0;
            }
        }
    }
    if (mcs>=n0)
    {
        count++;
        if (count==nb)
        {
            // accumulate results
            // magnitization(adsorption) for one msc
            // configuration is Mi
            for(i=1;i<=L;i++)
            {
                for(j=1;j<=L;j++)
                {
                    Mi=Mi+lattice[i][j][0];
                }
            }
```

```cpp
            // magnetization(adsorption) per spin mi=
            mi=mi+Mi/((double)L*(double)L);
            mi2_help=mi*mi;
            mi2_av2=mi2_av2+mi2_help;          // sum of mi^2
            mi4_av=mi4_av+mi2_help*mi2_help;  // sum of  mi^4
            samples=samples+1.0;
            //cout<<"mcs=["<<mcs<<"] Mi="<<Mi<<endl;
            //fExp<<mcs<<"\t"<<Mi<<endl;
            Mi=0;
            count=0;
        }
    }
}
//export the lattice configuration after msc steps
//export the snapshot of the superlattice at given mu
if(mu==mu_export)
{
    cout<<"Export Lattice...mcs="<<mcs<<endl;
    fExpLat.open(fExportLattice);
    if(!fExpLat)
    {
        cout<<"\n ERROR OPENING FILE ="<<fExportLattice;
    }
    fExpLat<<"L="<<L<<"\tmu="<<mu_export<<"\tJ="<<J<<"\tJ2="<<
    J2<<"\tmcs="<<mcs<<endl;
    fExpLat<<"AuX\tAuY\ti\tj\toccupy\tx\ty"<<endl;


    // export in x, y the x and y coordinates of the superlattice
    // the begin of the origin is x0,y0 with respect to
    // the lattice of Au(111)
    for(i=1;i<=L;i++)
    {
            for(j=1;j<=L;j++)
            {

                x=0;y=0;
                Convert_i_jTo_y_x(i,j,&x,&y,a,angle_x,angle_y,x0,y0);
                Convert_i_jTo_y_x(i,j,&x_Au,&y_Au,1.0,0.0,pi/3.0,0,0);
                fExpLat<<y_Au<<"\t"<<x_Au<<"\t"<<i<<"\t"<<j<<"\t"<<
                lattice[i][j][0]<<"\t"<<y<<"\t"<<x<<endl;
            }
    }




    fExpLat.close();
}


// calculate the average magnetization(adsorption) per site
mi=mi/samples;
// calculate <mi^2>^2 cumulant
mi2_av2=mi2_av2/samples;
mi2_av2=mi2_av2*mi2_av2;
// calculate <mi^4> cumulant
mi4_av=mi4_av/samples;
//cout<<"T="<<T<<"\t<mi>="<<mi<<endl;
fExp<<mu<<"\t"<<mi<<"\t"<<endl;
} // for each T
```

```cpp
cout<<"\n Done!"<<endl;
time(&now_s);
ptm1=localtime(&now_s);
cout<<"\n End calculating ... at "<<asctime(ptm1)<<endl;
end=clock();
cout<<"\n Elapsed time="<<(end-start)/1000<<"sec."<<endl;
fExp.close();
free_ivector(ip,1,L);
free_ivector(im,1,L);                    long end
free_ivector(ipp,1,L);
free_ivector(imm,1,L);
return 0;
}

double deltaW2(double J,double mu, int k, int l, int* ipp, int* imm)
// if lattice[i][j][0] has values -1;1 // OK for magnitization
// 1st NN - 4 atoms on squared lattice
{
double d, H1, H2;
// deltaW=Hnew-Hold,
// Hamiltonian=H1+H2=2*lattice[k][l][0](mu+lattice[ipp[k]][l][0]+
// lattice[imm[k]][l][0]+lattice[k][ipp[l]][0]+lattice[k][imm[l]][0])

H2=lattice[ipp[k]][l][0]+lattice[imm[k]][l][0]+lattice[k][ipp[l]][0]+
lattice[k][imm[l]][0];

H2=2*J*H2*lattice[k][l][0];
H1=2*mu*lattice[k][l][0];
d=H1+H2;;
cout<<"deltaH="<<d;
if(d<0) return 0.0; else return d ;

}
double deltaW3(double J,double mu, int k, int l, int* ipp, int* imm)
// goes to every site to calculate diff
// if lattice[i][j][0] has values 0;1 // OK for adsorption
// 1st nearest nei - 6 atoms = hexagon
{
double d;
// d=Hnew-Hold
// Hamiltonian=-mu*lattice[k][l][0]-J*lattice[k][l][0]*
// (lattice[ipp[k]][l][0]+lattice[imm[k]][l][0]+lattice[k][ipp[l]][0]+
// lattice[k][imm[l]][0])




if(lattice[k][l][0]==0)
{
    d=-mu-J*(lattice[ipp[k]][l][0]+lattice[imm[k]][l][0]+
    lattice[k][ipp[l]][0]+lattice[k][imm[l]][0]+lattice[ipp[k]][imm[l]][0]+
    lattice[imm[k]][ipp[l]][0]);
}
else
{
    d=mu+J*(lattice[ipp[k]][l][0]+lattice[imm[k]][l][0]+
    lattice[k][ipp[l]][0]+lattice[k][imm[l]][0]+lattice[ipp[k]][imm[l]][0]+
    lattice[imm[k]][ipp[l]][0]);
}

//cout<<"deltaH="<<d;

if(d<0) return 0.0; else return d ;
}
```

```cpp
double deltaW4NN2(double J1,double J2, double mu, int k, int l,
          int* ip, int* im, int* ipp, int* imm)
{
//  (6 atoms 1st NN) and ( 6 atoms 2nd NN ) = hexagonal lattice
double d, h1, h2;
h1=0;
h2=0;
if(lattice[k][l][0]==0)
{
    //1st NN
    h1=h1+lattice[ip[k]][l][0]+lattice[im[k]][l][0];
    h1=h1+lattice[k][ip[l]][0]+lattice[k][im[l]][0];
    h1=h1+lattice[ip[k]][im[l]][0]+lattice[im[k]][ip[l]][0];
    d=-mu-J1*h1;
    // 2nd NN
    h2=h2+lattice[ipp[k]][im[l]][0]+lattice[imm[k]][ip[l]][0];
    h2=h2+lattice[ip[k]][imm[l]][0]+lattice[im[k]][ipp[l]][0];
    h2=h2+lattice[ip[k]][ip[l]][0]+lattice[im[k]][im[l]][0];
    d=d-J2*h2;
}
else
{
    //1st NN
    h1=h1+lattice[ip[k]][l][0]+lattice[im[k]][l][0];
    h1=h1+lattice[k][ip[l]][0]+lattice[k][im[l]][0];
    h1=h1+lattice[ip[k]][im[l]][0]+lattice[im[k]][ip[l]][0];
    d=mu+J1*h1;
    // 2nd NN
    h2=h2+lattice[ipp[k]][im[l]][0]+lattice[imm[k]][ip[l]][0];
    h2=h2+lattice[ip[k]][imm[l]][0]+lattice[im[k]][ipp[l]][0];
    h2=h2+lattice[ip[k]][ip[l]][0]+lattice[im[k]][im[l]][0];
    d=d+J2*h2;
}
//cout<<"deltaH="<<d;
if(d<0) return 0.0; else return d ;
}
void Convert_i_jTo_y_x(int i, int j, double *y, double *x,
const double a, const double angle_x,const double angle_y,
const double x0, const double y0)
{
    *x=x0+double(i-1)*cos(angle_y)*a+double(j-1)*cos(angle_x)*a;
    *y=y0+double(i-1)*sin(angle_y)*a+double(j-1)*a*sin(angle_x);
}
```

Manufacturer list

Advance Ceramics	Advance Ceramics Corporation, USA
Advent	Advent Research Materials Ltd., Oxford, UK
Alfa	Alfa Johnson Matthey Company, Karlsruhe
BASF	BASF, Ludwigshafen
Berliner glass KG	Berliner glass KG, Berlin
Eco Chemie	Eco Chemie B.V., Ultrecht, The Netherlands
Fluka	Fluka Chemie AG, Switzerland
Griesheim	Messer Group GmbH, Krefeld
Oriental Motors	Oriental-Motors(Europe), Düsseldorf
MaTeck	Material-Technologie & Kristalle GmbH, Juelich
Millipore	Millipore Corporation, Massachusetts, USA
MI	Molecular Imaging Corp., USA
Nanotecnology	Merck, Darmstadt
New Focus Inc	New Focus Inc, St. Clara, USA
Omicron	Omicron NanoTechnology GmbH,Taunusstein
Park	Park Scientific Instruments, USA

Bibliography

[1] G. A. Somorjai. *Introduction to surface chemistry and catalysis.* Wiley Interscience, 1994.

[2] Allen J. Bard and Larry R. Faulkner. *Electrochemical methods.* Wiley & Sons, 2001.

[3] E. Budevski, G. Staikov, and W. J. Lotenz. *Electrochemical Phase Formation and Growth.* VCH, 1996.

[4] G. Binning, H. Rohrer, C. Gerber, and E. Weibel. *Physical Review Letters*, 49(1):57–61, 1982.

[5] C. B. Duke and E. W. Plummer. *Frontier in Surface and Interface Science.* Elsevier, 2002.

[6] G. Binnig, H. Rohrer, C. Gerber, and E. Weibel. *Physica B & C*, 110(1-3):2075–2077, 1982.

[7] G. Binnig, H. Rohrer, C. Gerber, and E. Weibel. *Applied Physics Letters*, 40(2):178–180, 1982.

[8] R. Wiesendanger. *Scanning Probe Microscopy and Spectroscopy.* Cambridge University Press, 1994.

[9] G. Baym. *Lectures on Quantum Mechanics.* The Benjamin/Cummings Publishing Company, Reading, Massachusetts, 1969.

[10] J. Bardeen. *Physical Review Letters*, 6(2):57–&, 1961.

[11] J. Tersoff and D. R. Hamann. *Physical Review B*, 31(2):805–813, 1985.

[12] Kirsten von Bergmann. *Iron nanostructures studied by spin-polarised scanning tunneling microscopy.* PhD thesis, Universität Hamburg, 2004.

[13] Stefan Griessl. *Zweidimensionale Architekturen organischer Adsorbate: Untersuchung mittels STM, LEED, TDS und Kraftfeldsimulationen.* PhD thesis, Technischen Universität Chemnitz, 2003.

[14] R. S. Nicholson and I. Shain. *Analytical Chemistry*, 36(4):706–&, 1964.

[15] L. Blum. *Advances in Chemical Physics*, 78:171–222, 1990.

[16] P. A. Rikvold. *Electrochimica Acta*, 36(11-12):1685–1687, 1991.

[17] P. A. Rikvold, M. Gamboaaldeco, J. Zhang, M. Han, Q. Wang, H. L. Richards, and A. Wieckowski. *Surface Science*, 335(1-3):389–400, July 1995.

[18] L. Blum, D. A. Huckaby, and M. Legault. *Electrochimica Acta*, 41(14):2207–2227, 1996.

[19] K. Binder and D. W. Heermann. *Monte Carlo Simulation in Statistical Physics.* Berlin:Springer, 1997.

[20] N. Metropolis and S. Ulam. *Journal of the American Statistical Association*, 44(247):335–341, 1949.

[21] N. Metropolis, A. W. Rosenbluth, M. N. Rosenbluth, A. H. Teller, and E. Teller. *Journal of Chemical Physics*, 21(6):1087–1092, 1953.

[22] R. K. Pathria. *Statistical Mechanics.* Oxford:Butherworth-Heinemann, 1996.

[23] O. Lev, F. R. Fan, and A. J. Bard. *Journal of the Electrochemical Society*, 135(3):783–784, 1988.

[24] O. M. Magnussen, J. Hotlos, R. J. Nichols, D. M. Kolb, and R. J. Behm. *Physical Review Letters*, 64(24):2929–2932, 1990.

[25] A. Shkurankov, F. Endres, and W. Freyland. *Review of Scientific Instruments*, 73(1):102–107, 2002.

[26] O. Nishikawa, M. Tomitori, and A. Minakuchi. *Surface Science*, 181(1-2):210–215, March 1987.

[27] R. Staub, D. Alliata, and C. Nicolini. *Review of Scientific Instruments*, 66(3):2513–2516, March 1995.

[28] P. J. Bryant, H. S. Kim, Y. C. Zheng, and R. Yang. *Review of Scientific Instruments*, 58(6):1115–1115, June 1987.

[29] H. Bourque and R. M. Leblanc. *Review of Scientific Instruments*, 66(3):2695–2697, March 1995.

[30] J. M. Lehn. *Supramolecular Chemsitry*. VCH Weinheim, 1995.

[31] G. M. Whitesides and M. Boncheva. *Proceedings of the National Academy of Sciences of the United States of America*, 99(8):4769–4774, April 2002.

[32] D. M. Cyr, B. Venkataraman, and G. W. Flynn. *Chemistry of Materials*, 8(8):1600–1615, August 1996.

[33] B. Venkataraman, J. J. Breen, and G. W. Flynn. *Journal of Physical Chemistry*, 99(17):6608–6619, April 1995.

[34] A. Wawkuschewski, H.J. Cantow, and S.N. Magonov. *Langmuir*, 9(11):2778–2781, November 1993.

[35] J. P. Rabe and S. Buchholz. *Science*, 253(5018):424–427, July 1991.

[36] G. C. Mcgonigal, R. H. Bernhardt, and D. J. Thomson. *Applied Physics Letters*, 57(1):28–30, July 1990.

[37] A. Wawkuschewski, H. J. Cantow, S. N. Magonov, M. Moller, W. Liang, and M. H. Whangbo. *Advanced Materials*, 5(11):821–826, November 1993.

[38] A. Ikai. *Surface Science Reports*, 26:261–332, 1996.

[39] K. Yoshimura, H. Arakawa, and A. Ikai. *Japanese Journal of Applied Physics Part 1-Regular Papers Short Notes & Review Papers*, 34(6B):3368–3372, June 1995.

[40] W. Liang, M. H. Whangbo, A. Wawkuschewski, H. J. Cantow, and S. N. Magonov. *Advanced Materials*, 5(11):817–821, November 1993.

[41] K. Ishida, S. Taki, H. Okabe, and K. Matsushige. *Japanese Journal of Applied Physics Part 1-Regular Papers Short Notes & Review Papers*, 34(7B):3846–3851, July 1995.

[42] S. Taki, K. Ishida, H. Okabe, and K. Matsushige. *Journal of Crystal Growth*, 131(1-2):13–16, July 1993.

[43] F. Schreiber. *Progress in Surface Science*, 65(5-8):151–256, November 2000.

[44] R. G. Nuzzo and D. L. Allara. *Journal of the American Chemical Society*, 105(13):4481–4483, 1983.

[45] U. Durig, O. Zuger, B. Michel, L. Haussling, and H. Ringsdorf. *Physical Review B*, 48(3):1711–1717, July 1993.

[46] G. E. Poirier and E. D. Pylant. *Science*, 272(5265):1145–1148, May 1996.

[47] Y. T. Kim, R. L. Mccarley, and A. J. Bard. *Journal of Physical Chemistry*, 96(18):7416–7421, September 1992.

[48] C. L. Claypool, F. Faglioni, W. A. Goddard, H. B. Gray, N. S. Lewis, and R. A. Marcus. *Journal of Physical Chemistry B*, 101(31):5978–5995, July 1997.

[49] B. Venkataraman, G. W. Flynn, J. L. Wilbur, J. P. Folkers, and G. M. Whitesides. *Journal of Physical Chemistry*, 99(21):8684–8689, May 1995.

[50] D. M. Cyr, B. Venkataraman, G. W. Flynn, A. Black, and G. M. Whitesides. *Journal of Physical Chemistry*, 100(32):13747–13759, August 1996.

[51] J. P. Rabe, S. Buchholz, and L. Askadskaya. *Synthetic Metals*, 54(1-3):339–349, March 1993.

[52] H. Y. Sheng, D. Fujita, T. Ohgi, Z. C. Dong, Q. D. Jiang, and H. Nejoh. *Applied Surface Science*, 121:129–132, November 1997.

[53] T. Ohgi, H. Y. Sheng, Z. C. Dong, and H. Nejoh. *Surface Science*, 442(2):277–282, November 1999.

[54] K. J. C. Muyskens, D. M. Cyr, G. W. Flynn, A. Black, and G. M. Whitesides. *Abstracts of Papers of the American Chemical Society*, 213:417–HYS, April 1997.

[55] S. R. Snyder and H. S. White. *Journal of Physical Chemistry*, 99(15):5626–5632, April 1995.

[56] N. J. Tao, G. Cardenas, F. Cunha, and Z. Shi. *Langmuir*, 11(11):4445–4448, November 1995.

[57] T. A. Jung, R. R. Schlittler, and J. K. Gimzewski. *Nature*, 386(6626):696–698, April 1997.

[58] S. Chiang. *Chemical Reviews*, 97(4):1083–1096, June 1997.

[59] T. Yokoyama, S. Yokoyama, T. Kamikado, Y. Okuno, and S. Mashiko. *Nature*, 413(6856):619–621, October 2001.

[60] A. Hoshino, S. Isoda, H. Kurata, and T. Kobayashi. *Journal of Crystal Growth*, 146(1-4):636–640, January 1995.

[61] H. Muller, J. Petersen, R. Strohmaier, B. Gompf, W. Eisenmenger, M.S. Vollmer, and F. Effenberger. *Advanced Materials*, 8(9):733–&, September 1996.

[62] J. C. Gabriel, N. B. Larsen, M. Larsen, N. Harrit, J. S. Pedersen, K. Schaumburg, and K. Bechgaard. *Langmuir*, 12(6):1690–1692, March 1996.

[63] K. W. Hipps, X. Lu, X. D. Wang, and U. Mazur. *Journal of Physical Chemistry*, 100(27):11207–11210, July 1996.

[64] X. Lu, K. W. Hipps, X. D. Wang, and U. Mazur. *Journal of the American Chemical Society*, 118(30):7197–7202, July 1996.

[65] S. Berner, M. de Wild, L. Ramoino, S. Ivan, A. Baratoff, H. J. Guntherodt, H. Suzuki, D. Schlettwein, and T. A. Jung. *Physical Review B*, 68(11):–, September 2003.

[66] J. S. Moore. *Accounts of Chemical Research*, 30(10):402–413, October 1997.

[67] S. Hoger. *Journal of Polymer Science Part A-Polymer Chemistry*, 37(15):2685–2698, August 1999.

[68] M. M. Haley, J. J. Pak, and S. C. Brand. *Carbon Rich Compounds Ii*, 201:81–130, 1999.

[69] S. Chandrasekhar, B. K. Sadashiva, and K. A. Suresh. *Pramana*, 9(5):471–480, 1977.

[70] O.Y. Mindyuk, M.R. Stetzer, P.A. Heiney, J.C. Nelson, and J.S. Moore. *Advanced Materials*, 10(16):1363–+, November 1998.

[71] J. S. Zhang and J. S. Moore. *Journal of the American Chemical Society*, 114(24):9701–9702, November 1992.

[72] A. S. Shetty, J. S. Zhang, and J. S. Moore. *Journal of the American Chemical Society*, 118(5):1019–1027, February 1996.

[73] Y. Tobe, N. Utsumi, A. Nagano, and K. Naemura. *Angewandte Chemie-International Edition*, 37(9):1285–1287, May 1998.

[74] Y. Tobe, A. Nagano, K. Kawabata, M. Sonoda, and K. Naemura. *Organic Letters*, 2(21):3265–3268, October 2000.

[75] S. Lahiri, J. L. Thompson, and J. S. Moore. *Journal of the American Chemical Society*, 122(46):11315–11319, November 2000.

[76] S. Hoger and A. D. Meckenstock. *Chemistry-A European Journal*, 5(6):1686–1691, June 1999.

[77] M. Fischer and S. Hoger. *European Journal of Organic Chemistry*, (3):441–446, February 2003.

[78] C. Grave, D. Lentz, A. Schafer, P. Samori, J. P. Rabe, P. Franke, and A. D. Schluter. *Journal of the American Chemical Society*, 125(23):6907–6918, June 2003.

[79] J. Kromer, I. Rios-Carreras, G. Fuhrmann, C. Musch, M. Wunderlin, T. Debaerdemaeker, E. Mena-Osteritz, and P. Bauerle. *Angewandte Chemie-International Edition*, 39(19):3481–+, 2000.

[80] O. Henze, D. Lentz, A. Schafer, P. Franke, and A. D. Schluter. *Chemistry-A European Journal*, 8(2):357–365, January 2002.

[81] D. B. Werz, T. H. Staeb, C. Benisch, B. J. Rausch, F. Rominger, and R. Gleiter. *Organic Letters*, 4(3):339–342, February 2002.

[82] K. Campbell, C. J. Kuehl, M. J. Ferguson, P. J. Stang, and R. R. Tykwinski. *Journal of the American Chemical Society*, 124(25):7266–7267, June 2002.

[83] P. Muller, I. Uson, V. Hensel, A. D. Schluter, and G. M. Sheldrick. *Helvetica Chimica Acta*, 84(4):778–785, 2001.

[84] D. Venkataraman, S. Lee, J.S. Zhang, and J.S. Moore. *Nature*, 371(6498):591–593, October 1994.

[85] S. Hoger, K. Bonrad, A. Mourran, U. Beginn, and M. Moller. *Journal of the American Chemical Society*, 123(24):5651–5659, June 2001.

[86] O. Y. Mindyuk, M. R. Stetzer, D. Gidalevitz, P. A. Heiney, J. C. Nelson, and J. S. Moore. *Langmuir*, 15(20):6897–6900, September 1999.

[87] L. Strong and G. M. Whitesides. *Langmuir*, 4(3):546–558, May 1988.

[88] G. E. Poirier and M. J. Tarlov. *Langmuir*, 10(9):2853–2856, September 1994.

[89] P. Fenter, A. Eberhardt, and P. Eisenberger. *Science*, 266(5188):1216–1218, November 1994.

[90] N. Camillone, C.E.D. Chidsey, G.Y. Liu, and G. Scoles. *Journal of Chemical Physics*, 98(4):3503–3511, February 1993.

[91] M. J. Beulen, J. Bugler, B. Lammerink, F. J. Geurts, E. F. Biemond, K. C. van Leerdam, F. M. van Veggel, J. J. Engbersen, and D. N. Reinhoudt. *Langmuir*, 14(22):6424–6429, October 1998.

[92] D. Borissov, A. Ziegler, S. Hoger, and W. Freyland. *Langmuir*, 20(7):2781–2784, 2004.

[93] M. Bohringer, K. Morgenstern, W. D. Schneider, R. Berndt, F. Mauri, A. De Vita, and R. Car. *Physical Review Letters*, 83(2):324–327, July 1999.

[94] M. J. S. Dewar, E. G. Zoebisch, E. F. Healy, and J. J. P. Stewart. *Journal of the American Chemical Society*, 107(13):3902–3909, 1985.

[95] S. N. Magonov and M. H. Whangbo. *Advanced Materials*, 6(5):355–371, May 1994.

[96] F. Faglioni, C. L. Claypool, N. S. Lewis, and W. A. Goddard. *Journal of Physical Chemistry B*, 101(31):5996–6020, July 1997.

[97] D. G. Castner, K. Hinds, and D. W. Grainger. *Langmuir*, 12(21):5083–5086, October 1996.

[98] C. D. Wagner. *Handbook of X-ray Photoelectron Spectroscopy*. Perkin-Elmer Corporation, USA, 1979.

[99] J. Riga and J.J. Verbist. *Journal of the Chemical Society-Perkin Transactions 2*, (10):1545–1551, 1983.

[100] P. E. Laibinis, G. M. Whitesides, D. L. Allara, Y. T. Tao, A. N. Parikh, and R. G. Nuzzo. *Journal of the American Chemical Society*, 113(19):7152–7167, September 1991.

[101] K. Heister, M. Zharnikov, M. Grunze, and L. S. O. Johansson. *Journal of Physical Chemistry B*, 105(19):4058–4061, May 2001.

[102] H. J. Himmel, C. Woll, R. Gerlach, G. Polanski, and H. G. Rubahn. *Langmuir*, 13(4):602–605, February 1997.

[103] C. J. Zhong, R. C. Brush, J. Anderegg, and M. D. Porter. *Langmuir*, 15(2):518–525, January 1999.

[104] H. Gronbeck, A. Curioni, and W. Andreoni. *Journal of the American Chemical Society*, 122(16):3839–3842, April 2000.

[105] K. Christmann. *Introduction to Surface Physical Chemistry*. Springer, 1991.

[106] H. Sellers, A. Ulman, Y. Shnidman, and J. E. Eilers. *Journal of the American Chemical Society*, 115(21):9389–9401, October 1993.

[107] R.R. Adzic. *Advances in Electrochemistry and Electrochemical Engineering*. Number 13. John Wiley & Sons, 1984.

[108] G. Kokkinidis. *Journal of Electroanalytical Chemistry and Interfacial Electrochemistry*, 201(2):217–236, 1986.

[109] Andrew A. Gewirth and Brian K. Niece. *Chemical Reviews (Washington, D.C.)*, 97(4):1129–1162, 1997.

[110] J. X. Wang, R. R. Adzic, and B. M. Ocko. *Interfacial Electrochemistry, Theory, Experiment and Applications*. Marcel Dekker, 1999.

[111] K. Takayanagi, D. M. Kolb, K. Kambe, and G. Lehmpfuhl. *Surface Science*, 100(2):407–422, 1980.

[112] Joseph T. Hupp, D. Larkin, H. Y. Liu, and Michael J. Weaver. *Journal of Electroanalytical Chemistry and Interfacial Electrochemistry*, 131:299–307, 1982.

[113] J. McBreen and M. Sansone. *Journal of Electroanalytical Chemistry*, 373(1-2):227–233, 1994.

[114] Ezequiel Leiva and Wolfgang Schmickler. *Electrochimica Acta*, 39(8-9):1015–1017, 1994.

[115] W. J. Lorenz, G. Staikov, W. Schindler, and W. Wiesbeck. *Journal of the Electrochemical Society*, 149(12):K47–K59, 2002.

[116] R. D. Rogers and K. R. Seddon. *Science*, 302(5646):792–793, October 2003.

[117] K. R. Seddon. *Journal of Chemical Technology and Biotechnology*, 68(4):351–356, April 1997.

[118] F. Endres. *Chemphyschem*, 3(2):144–+, February 2002.

[119] F. Endres and W. Freyland. *Abstracts of Papers of the American Chemical Society*, 221:U327–U327, April 2001.

[120] W. Freyland, C. A. Zell, S. Z. El Abedin, and F. Endres. *Electrochimica Acta*, 48(20-22):3053–3061, September 2003.

[121] I. Mukhopadhyay, C. L. Aravinda, D. Borissov, and W. Freyland. *Electrochimica Acta*, 50(6):1275–1281, January 2005.

[122] I. Mukhopadhyay and W. Freyland. *Langmuir*, 19(6):1951–1953, March 2003.

[123] F. Endres and S. Z. El Abedin. *Physical Chemistry Chemical Physics*, 4(9):1640–1648, 2002.

[124] F. Endres. *Electrochemical and Solid State Letters*, 5(3):C38–C40, March 2002.

[125] S. Z. El Abedin, N. Borissenko, and F. Endres. *Electrochemistry Communications*, 6(5):510–514, May 2004.

[126] C. A. Zell and W. Freyland. *Chemical Physics Letters*, 337(4-6):293–298, April 2001.

[127] C. A. Zell and W. Freyland. *Langmuir*, 19(18):7445–7450, September 2003.

[128] C. L. Aravinda and W. Freyland. *Chemical Communications*, (23):2754–2755, 2004.

[129] K. Itaya. *Nanotechnology*, 3:185–187, 1992.

[130] M. J. Esplandiu, M. A. Schneeweiss, and D. M. Kolb. *Physical Chemistry Chemical Physics*, 1(20):4847–4854, 1999.

[131] P. Mrozek, Y. E. Sung, M. Han, M. Gamboaaldeco, A. Wieckowski, C. H. Chen, and A. A. Gewirth. *Electrochimica Acta*, 40(1):17–28, 1995.

[132] M. A. Schneeweiss and D. M. Kolb. *Solid State Ionics*, 94(1-4):171–179, 1997.

[133] Dennis J. Trevor, Christopher E. D. Chidsey, and Dominic N. Loiacono. *Physical Review Letters*, 62(8):929–932, 1989.

[134] C. A. Zell, F. Endres, and W. Freyland. *Physical Chemistry Chemical Physics*, 1(4):697–704, 1999.

[135] John D. Porter and Timothy O. Robinson. *Journal of Physical Chemistry*, 97(25):6696–6709, 1993.

[136] Shen Ye, Chikara Ishibashi, and Kohei Uosaki. *Langmuir*, 15(3):807–812, 1999.

[137] P. Mrozek, Y. E. Sung, and A. Wieckowski. *Surface Science*, 335(1-3):44–51, July 1995.

[138] C. H. Chen, S. M. Vesecky, and A. A. Gewirth. *Journal of the American Chemical Society*, 114(2):451–458, January 1992.

[139] D. M. Kolb. *Advances in Electrochemistry an Electrochemical Engineering*. Wiley-Interscience, New York, 1978.

[140] O. M. Magnussen. *Chemical reviews*, 102(3):679–725, March 2002.

[141] G. R. Stafford, V. D. Jovic, T. P. Moffat, Q. Zhu, S. Jones, and C. L. Hussey. *Proceedings - Electrochemical Society*, 99-41(Molten Salts XII):535–548, 2000.

[142] Satoshi Taguchi and Akiko Aramata. *Journal of Electroanalytical Chemistry*, 396(1-2):131–137, 1995.

[143] William H. Press. *Numerical recipes in C, C++*. Cambridge University Press, 2002.

[144] Sasha Gorer, Hongtao Liu, Rebecca M. Stiger, Michael P. Zach, James V. Zoval, and Reginald M. Penner. *Metal Nanoparticles*, pages 237–259, 2002.

[145] H. Natter, M. Schmelzer, S. Janssen, and R. Hempelmann. *Berichte der Bunsen-Gesellschaft*, 101(11):1706–1713, 1997.

[146] Branko N. Popov. *Plating and Surface Finishing*, 91(10):40–49, 2004.

[147] H. Liu and R. M. Penner. *Journal of Physical Chemistry B*, 104(39):9131–9139, 2000.

[148] Kwok H. Ng, H. Liu, and R.M. Penner. *Langmuir*, 16(8):4016–4023, 2000.

[149] A. Milchev. *Journal of Chemical Physics*, 100(7):5160–5164, 1994.

[150] R.M. Penner. *Journal of Physical Chemistry B*, 106(13):3339–3353, 2002.

[151] Ellis Harwood. *Southampton Electrochemistry Group, Instrumental Methods in Electrochemistry.* Chichester, UK, 1990.

[152] David R. Lide. *CRC handbook of chemistry and physics / Chemical Rubber Company.* CRC Press, 86th edition.

Acknowledgments

First and foremost, I would sincerely like to acknowledge Prof. W. Freyland as my thesis adviser. His broad and unique view to research has motivated me not only to carry out very interesting investigations but also enhanced my understanding in the field of surface science and physical chemistry.

I would like to thank Prof. S. Höger for giving me the opportunity to study his exotic macromolecules and Prof. M. Olzmann, my second reader, whose comments were extremely helpful.

I wish to give my very special thanks to Prof. Roumen Tsekov who has been a constant source of support and encouragement for me as well as for his exciting discussions we have had on scientific and less scientific matter.

I owe my gratitude to all present and formal members of the IPC and especialy to Dr. Indrajit Mukhopadhyay for the fun times we shared during the work, Dr. C. L. Aravinda and Dr. Ethel Bucharsky for their support and friendly atmosphere. Also I would like to thank Dr. Vadym Halka for giving me some valuable advice as a man with more experience than me and his availability concerning every day problems. Last but not least, Oliver Mann and Dr. Ge-Bo Pan, the first for introducing to me Beaujolais Nouveau and the last for making me keen on original Chinese green tee. Also, I would like to thank:

K. Jacob for his support concerning STM scanners and electronics; D. Waltz and all members of the mechanical workshop for their solutions to many technical problems; J. Dubielzig for his help whenever there was a problem in the lab; J. Szepessy for his availability concerning hardware and software problems.

At last, I am incredibly grateful to my family who gave me their unconditional support during all these years and Anna without her help, guidance and encouragement I couldn't have made it this far.

Curriculum Vitae

PERSONAL DATA:

Family Name:	Borissov
First Names:	Dimitar Iliev
Date of Birth:	2. 12. 1977
Place of Birth:	Sofia, Bulgaria
Nationality:	Bulgarian
Marital Status:	Single

EDUCATION:

2002 - 2005:	Ph.D. University of Karlsruhe(TH), Germany
	Supervisor: Prof. Dr. Werner Freyland
1995 - 2000:	M.Sc. in Chemistry
	Sofia University(SU), Bulgaria
1991 - 1995:	High-School Education
	National High-School of Mathematics and Science
	Sofia, Bulgaria

Publications

1. Pulsed Electrodeposition of Two-Dimensional Ag Nanostructures on Au(111)
   D. Borissov; R. Tsekov and W. Freyland; *Journal of Physical Chemistry B*, **2006**, accepted

2. Liquid/Vapour and Electrified Solid/Liquid Interfaces of Ionic Liquids
   C. L. Aravinda; D. Borissov; W. Freyland; V. Halka; O. Mann; *Proc. 7ᵗʰ Int. Symposium on Molten Salts*, P. Taxil, C. Besada, Toulouse, **2005**.

3. Comparative Investigation of Underpotential Deposition of Ag from Aqueous and Ionic Electrolytes: An Electrochemical and in situ STM Study
   D. Borissov; C. L. Aravinda; W. Freyland; *Journal of Physical Chemistry B*, **2005**, *109*(23), 11606-11615.

4. Electrodeposition of Ti from $TiCl_4$ in the Ionic Liquid 1-methyl-3-butylimidazolium bis(trifluoromethylsulfone) imide at Room Temperature: Study on Phase Formation by in situ Electrochemical Scanning Tunneling Microscopy
   I. Mukhopadhyay; D. Borissov; C. L. Aravinda; W. Freyland; *Electrochimica Acta*, **2005**, *50*(6), 1275-1281.

5. SAMs of Shape-Persistent Macrocycles: Structure and Binding on HOPG and Au(111)
   D. Borissov; A. Ziegler; S. Hoeger; W. Freyland; *Langmuir*, **2004**, *20*(7), 2781-2784.

6. Electrochemical incorporation of copper in polyaniline layers
   V. Tsakova; D. Borissov; B. Ranguelov; Ch. Stromberg; J. W. Schultze; *Electrochimica Acta*, **2001**, *46*(26-27), 4213-4222.

7. Role of polymer synthesis conditions for the copper electrodeposition in polyaniline

V. Tsakova; D. Borissov; S. Ivanov; *Electrochemistry Communications* **2001**, *3*(6), 312-316.

8. Electrochemical deposition of copper in polyaniline films - number density and spatial distribution of deposited metal clusters.
V. Tsakova; D. Borissov; S. Ivanov; *Electrochemistry Communications* **2000**, *2*(7), 511-515.